Title

Investigating the processing and transformation of visual stimuli for spatial navigation in the mouse cortex

Author

Sit, Kevin Ka-man

Publication Date

2022

University of California
Santa Barbara

Investigating the processing and transformation of visual stimuli for spatial navigation in the mouse cortex

A dissertation submitted in partial satisfaction
of the requirements for the degree

Doctor of Philosophy
in
Psychological & Brain Sciences

by

Kevin Ka-man Sit

Committee in charge:

Professor Michael J. Goard, Chair
Professor Tod E. Kippin
Professor Benjamin E. Reese
Professor Ikuko T. Smith
Professor Spencer L. Smith

September 2022

The Dissertation of Kevin Ka-man Sit is approved.

Professor Tod E. Kippin

Professor Benjamin E. Reese

Professor Ikuko T. Smith

Professor Spencer L. Smith

Professor Michael J. Goard, Committee Chair

September 2022

Investigating the processing and transformation of visual stimuli for spatial navigation in the mouse cortex

by

Kevin Ka-man Sit

Acknowledgements

First and foremost, thank you to my advisor and mentor Dr. Michael Goard, for his endless guidance, feedback, and patience throughout my graduate training.

Next, to the members of the Goard lab, past and present, whom I've been fortunate enough to spend countless hours with, both inside and outside of work.

Lastly, to my family who have provided unwavering support and the opportunity to pursue this dream.

Curriculum Vitæ

Kevin Ka-man Sit

Education

2022	Ph.D. in Psychological and Brain Sciences (Expected), University of California, Santa Barbara.
2016	B.S. in Physiology and Neuroscience, University of California, San Diego.

Publications

2022	**Sit K.K.**, Goard M.J., *Coregistration of visual cues and heading in retrosplenial cortex.* (in revision, *Nature Communications*). doi: 10.1101/2022.03.25.486865
2022	**Sit K.K.**, Bess N., Beserra N., Franco L.M., Roney J.P., Goard M.J., *A modular, cost-effective solution for automated training of mice for head-fixed behaviors* (in preparation).
2022	Telias M.*, **Sit K.K.***, Frozenfar D., Smith B., Goard M.J.† Kramer R.H.†, *Retinoic acid inhibitors mitigate vision loss in a mouse model of retinal degeneration.* Science Advances 8, 11 (2022). doi: 10.1126/sciadv.abm4643 *: co-first author; †: co-last author
2022	Wolcott N.S., **Sit K.K.**, Raimandi G., Hodges T., Shansky R.M., Galea L.A.M., Ostroff L.E., Goard M.J., *Automated classification of estrous stage using deep learning.* (in revision, *Scientific Reports*). doi: 10.1101/2022.03.09.483678
2022	Redman W.T., Wolcott N.S., Montelisciani L., Luna G., Marks T.D., **Sit K.K.**, Yu C., Smith S.L., Goard M.J., *Long-term transverse imaging of the hippocampus with glass microperiscopes.* eLife 11:e75391 (2022). doi: 10.7554/eLife.75391
2020	**Sit K.K.**, Goard M.J., *Distributed and retinotopically asymmetric processing of coherent motion in mouse visual cortex.* Nature Communications 11, 3565 (2020). doi: 10.1038/s41467-020-17283-5

Abstract

Investigating the processing and transformation of visual stimuli for spatial navigation in the mouse cortex

by

Kevin Ka-man Sit

Visual information is a primary contributor to many cognitive processes, including learning, memory, and navigation. The mechanism by which visual stimuli from the external world are processed, transformed, and ultimately utilized is an area of open research. To tackle this question, we use cutting edge microscopy techniques in mice to thoroughly examine how visual stimuli are represented and processed in the brain. First, we examine how the visual cortex represents coherent motion, finding that there is significant heterogeneity in the responses of neurons to coherent motion across different visual cortical regions, as in primate visual cortex. Unexpectedly, we also found significant anisotropy in neural responses within each visual area that was highly correlated to visual elevation, but not azimuth. Second, we sought to understand how processed visual information is used in navigation, via studying the head direction network, which is important for representing the animal's orientation in an environment. Importantly, we also found a specific subclass of neurons which registers the responses from similarly tuned neurons across different cortical systems to anchor our internal heading to the external world. Third, we examined the effects of retinoic acid inhibitors on a mouse model of photoreceptor degenerative disease. We found that we were able to restore light-driven responses in the retina, stimulus coding in the visual cortex, and performance in a behavioral task. Together, these results contribute to a more comprehensive understanding of how visual stimuli are processed and incorporated by the neocortex to inform cognition.

Contents

Chapter 1

General Introduction

1.1 Overview of visual processing

Of all the primary senses, vision is particularly important, guiding many aspects of our lives. As with other sensory systems, the visual system is responsible for receiving, processing, and transforming stimuli into electrical impulses to drive ethological behaviors. For several millennia, scientists have been interested in the mechanisms by which light can enter into the eye and result in an image being imprinted onto the brain. Although the anatomical structure of the eye has been studied as early as the 4th century B.C.E. by ancient philosophers, such as Plato, only in the 11th century C.E. that our modern understanding of the eye began to form, largely due to Ibn al-Haytham's *Book of Optics*. Still, it took several centuries for researchers to begin to link the perception of vision to the brain, with initial tracing and lesion studies by Bartolomeo Panizza in the mid 19th century [1]. The modern era of visual neuroscience began in the mid 20th century, through the first chemical and physiological studies of the retina [2, 3, 4, 5]. Then, through a set of seminal experiments by David Hubel and Torstein Wiesel, our understanding of visual processing was expanded from the retina to the brain via their

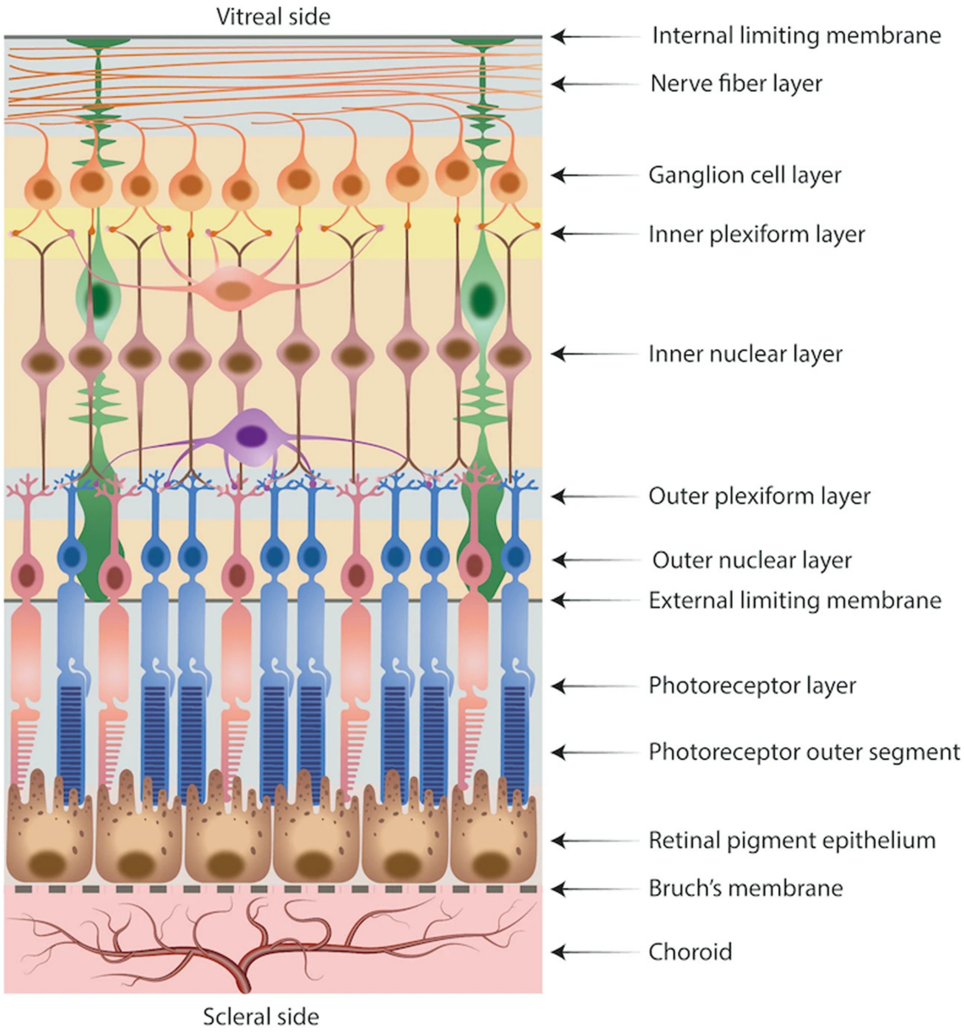

Figure 1.1: Schematic showing the laminar structure of the retina. Adapted from [7].

careful characterization of the visual cortex, including how cells in this area extract important information from visual scenes. [6] In the last couple decades, visual neuroscience has been an important field of study, both for understanding how vision itself works as a preface to treating visual disorders, as well as a generalized model for understanding sensory processing and computations as a whole.

Processing of stimuli in the retina

The retina is a complex laminar structure that contains several cell types that transduce and process visual stimuli (Figure 1.1). Of particular importance are the photoreceptors, which are cells that contain light-sensitive pigments [8]. Exposure to light causes specific ion channels in these cells to open and close, changing the cell's membrane potential and resulting in the first conversion from light to electrical signaling [9]. These signals are passed to bipolar cells, which receive inputs from more than one photoreceptor through horizontal cells. Because these cells receive information from several neighboring photoreceptors, bipolar cells exhibit the first structured receptive fields, which are shaped as concentric circles of opposite polarity [4]. Bipolar cells synapse onto retinal ganglion cells (RGCs) which convert the graded changes in membrane potential to neural spikes, the primary signal used in downstream neural processing. The retina also processes visual stimuli in many other ways, such as via color selectivity [10], spatial filtering [11], and temporal filtering [12]. Rather than relaying visual information in a completely faithful way, like a camera, the information that is sent from the retina has already been processed to some degree.

Flow of visual information to the cortex

In mammalian species, the cerebral cortex has developed as a computationally powerful structure, that has important functions in sensory processing [13], cognition [14], and motor output [15]. As a result, the processing of most sensory information, including visual stimuli, occurs along specialized hierarchies in the cortex. However, there is no direct synapse from the eye to the cortex, visual information passes through a series of subcortical brain regions first, forming two distinct pathways: the geniculate and extrageniculate pathways (Figure 1.2).

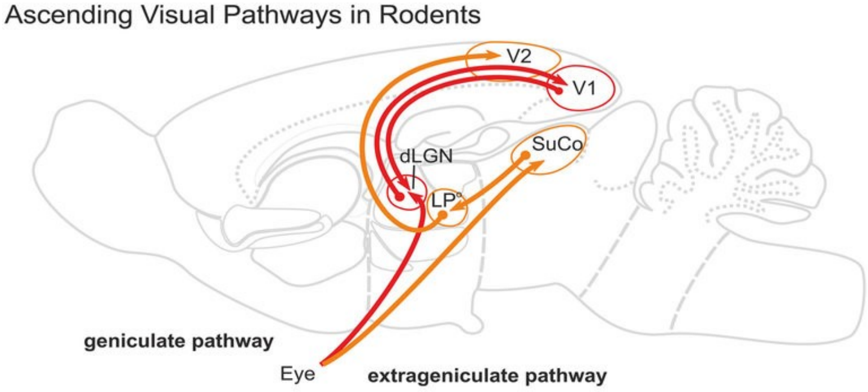

Figure 1.2: Example of ascending pathways, showing the geniculate and extrageniculate pathways. SuCo: Superior colliculus; LP: Lateral pulvinar; dLGN: Dorsal lateral geniculate nucleus; V1: primary visual cortex; V2: secondary visual cortex. Adapted from [16].

The extrageniculate pathway routes information from the retina through the superior colliculus [17], which is a structure than has been strongly implicated in orienting responses, such as turning to face a bright flash of light [18]. Other important ethological functions of the extrageniculate pathway include escape [19, 20] and defense [21] behaviors. The superior colliculus also sends projections to higher visual areas in the cortex, which recent studies suggest are preferentially responsive to stimuli containing high velocity motion [22]. However, the nature and purpose of these projections are still unclear, and is an open area of research.

On the other hand, a larger focus has been devoted to understanding the geniculate pathway, which is primarily responsible for the conscious perception of visual stimuli, and is the primary path of visual information into the cortex [17]. In the geniculate pathway, projections from the retina first synapse onto a thalamic region called the lateral geniculate nucleus (LGN). The LGN serves as an important relay nucleus, gating visual stimuli based on different behavioral states [23], but recent work has also elucidated its role in processing incoming visual information as well [24]. Interestingly, the LGN also receives significant feedback projections from the cortex, forming cortico-thalamo-

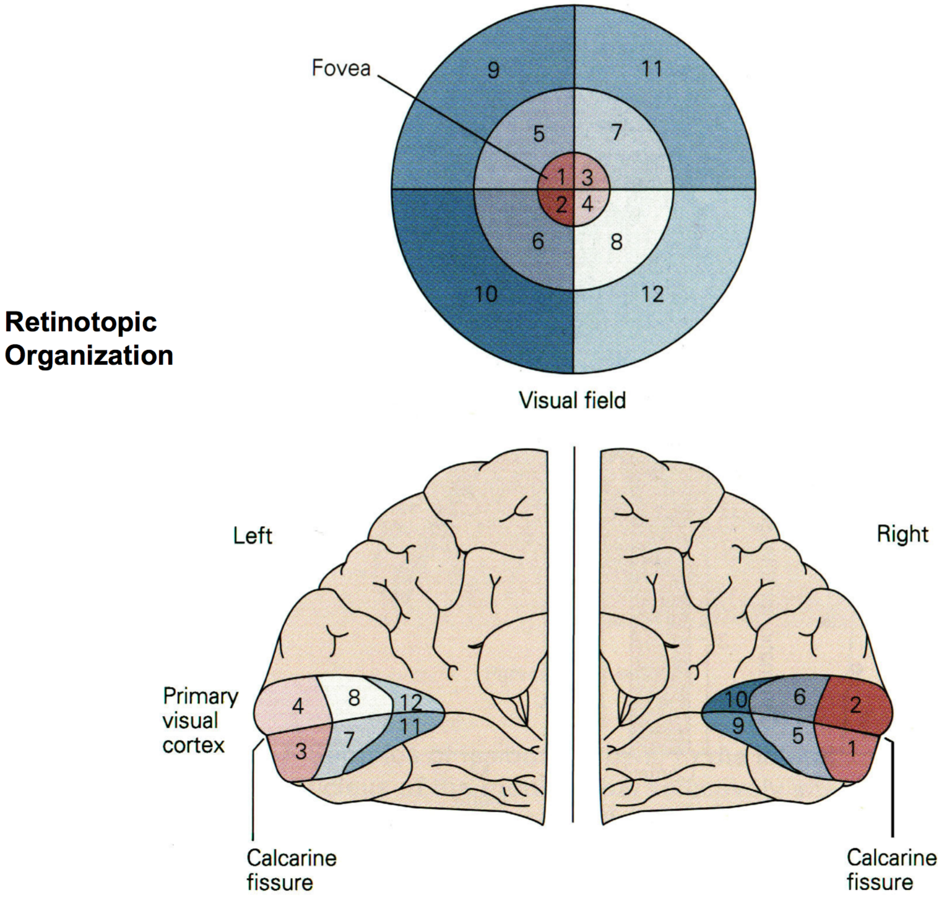

Figure 1.3: Example of retinotopic organization of the primary visual cortex. Top: visual stimulus presented. Bottom: Schematized location of visual stimulus on the visual cortex. Adapted from [26].

cortical loops [25], although the exact nature and purpose of these loops is still being studied. The primary output target of the LGN is the primary visual cortex (V1), the first cortical region in the visual processing hierarchy.

Despite being the *primary* visual cortex, a significant amount of sensory processing occurs in V1, resulting in neurons that exhibit a wide array of response properties. A fundamental property of neurons in visual areas is that they exhibit highly spatially localized receptive fields, so that individual neurons represent only a small portion of the total field of view [3]. As a result, visual areas contain a "retinotopic map", in which neighboring neurons represent neighboring portions of the visual scene [27, 28] (Figure 1.3). However, individual neurons also exhibit specialized tuning to specific features in visual stimuli within their particular receptive field. These preferences can include stimuli of specific sizes [29], speed [30], orientation [6], and color [31]. Therefore, each population of neurons extracts important stimulus features from the visual scene, parsing visual information to inform perception and behavior. However, V1 is still restricted in the amount of information that it can extract from the stimulus, so significant sensory processing and transformations are still required by downstream visual areas.

Transfer of visual information to extrastriate areas

Visual stimuli are a particularly rich medium, containing an abundance of information across multiple temporal and spatial scales. One strategy that the brain uses to process this information is to dedicate specialized visual cortical regions to extract and process specific features of the stimulus, such as motion [32], textures [33], or even faces [34]. Collectively, these areas are called higher visual areas (HVAs), and are hierarchically organized into two processing streams: the dorsal and ventral streams [35]. Each of these streams contain several HVAs that are specialized for processing specific visual features. The ventral stream culminates in the ability to recognize objects, and contains areas that are tuned for textures, shape, size, and combinations of these and other properties [36]. On the other hand, the dorsal stream is important for spatial processing, containing areas that are sensitive to location, movement, and spatial relationships [37]. However, these two streams are not entirely segregated, and information is transferred between areas in each stream [38]. Together, these two processing streams further dissect features from the visual stimuli, ultimately for altering cognitive variables or producing relevant behaviors.

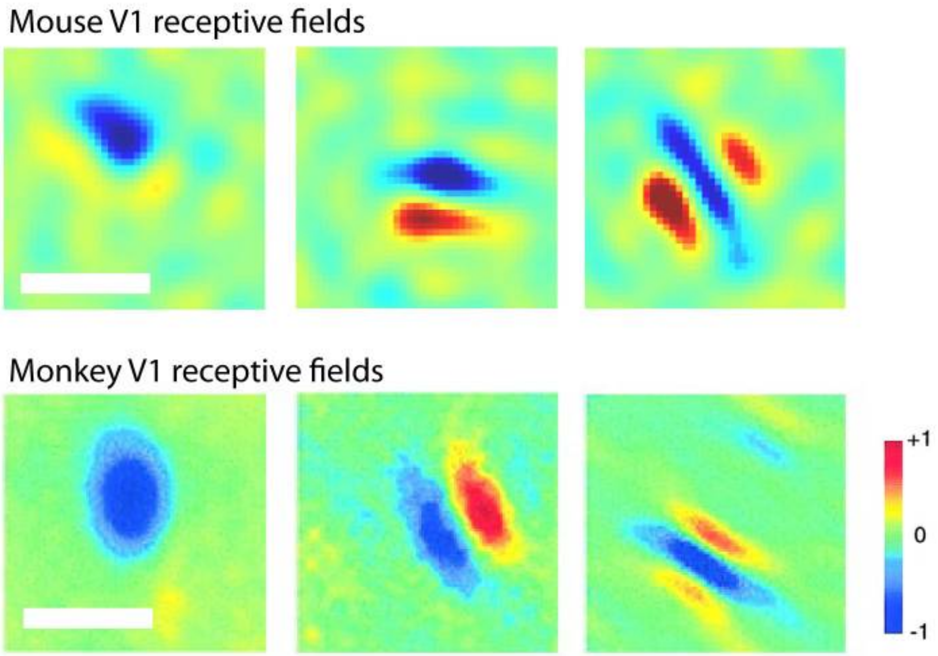

Figure 1.4: Example receptive field of neurons from mouse V1 compared against monkey V1 neurons. Top: receptive fields from mouse. Bottom: receptive fields from monkey. Adapted from [39].

Homology of murine and primate visual cortex

In the last decade, the mouse has become an attractive model organism, particularly because of its high genetic tractability. Coupled with large advancements in microscopy techniques, all-optical interrogation allows measurement and manipulation of large populations of neurons that was never before possible. Leveraging these techniques allows researchers to pursue new avenues of research to understand the brain at more complete and ethologically relevant scales.

Much of the previous work to understand how visual stimuli are transformed in the cortex was performed in cats and nonhuman primates, which have highly developed visual systems with high visual acuity. Despite having lower visual acuity, the mouse visual cortex is also highly developed and is homologous to primate cortex, particularly at lower levels of visual processing [39]. Early work in the mouse visual system [40] demonstrated that the spatial receptive fields of neurons in mouse V1 exhibit the same shape and properties, albeit with much larger size, as the neurons in primate V1 (Figure 1.4). Furthermore, neurons in mouse V1 exhibit the same tuning properties as primates, such as orientation tuning [40]. Lastly, mice also have a large set of HVAs that are similarly organized into putative dorsal and ventral streams [41, 42]. The mouse visual cortex has been an important contributor to our understanding of the complex cortical computations, particularly at the population level, of visual stimuli.

1.2 Overview of spatial navigation systems

One of the major outputs of the visual system, particularly in rodents, is in brain regions fundamental for spatial cognition and navigation. The rodent model has been fundamental in our understanding of how mammalian brains construct internal maps of the physical world to enable successful navigation.

What types of spatial cognitive maps exist in the mammalian brain? Perhaps the most well-known is the existence of a specific type of cell in the hippocampus (HPC) called “place cells”. Place cells preferentially respond when animals are in a specific location in their environment, creating a neural representation of the position of the animal at any given time [44] (Figure 1.5A). The responses of place cells is thought to be derived from another type of cell, “grid cells”, whose responses create a repeating pattern that tiles an animal’s local environment [45] (Figure 1.5B). Together, place and grid cells enable the brain to create an accurate, yet flexible, representation of the external world.

However, successful navigation requires both knowledge of current position as well as orientation in an environment, such as using both a map and a compass. While place and grid cells represent an animal’s position, its orientation is represented by a third class of cells, the “head direction cells” (HD cells) [47, 48] (Figure 1.6A, B). Head direction cells

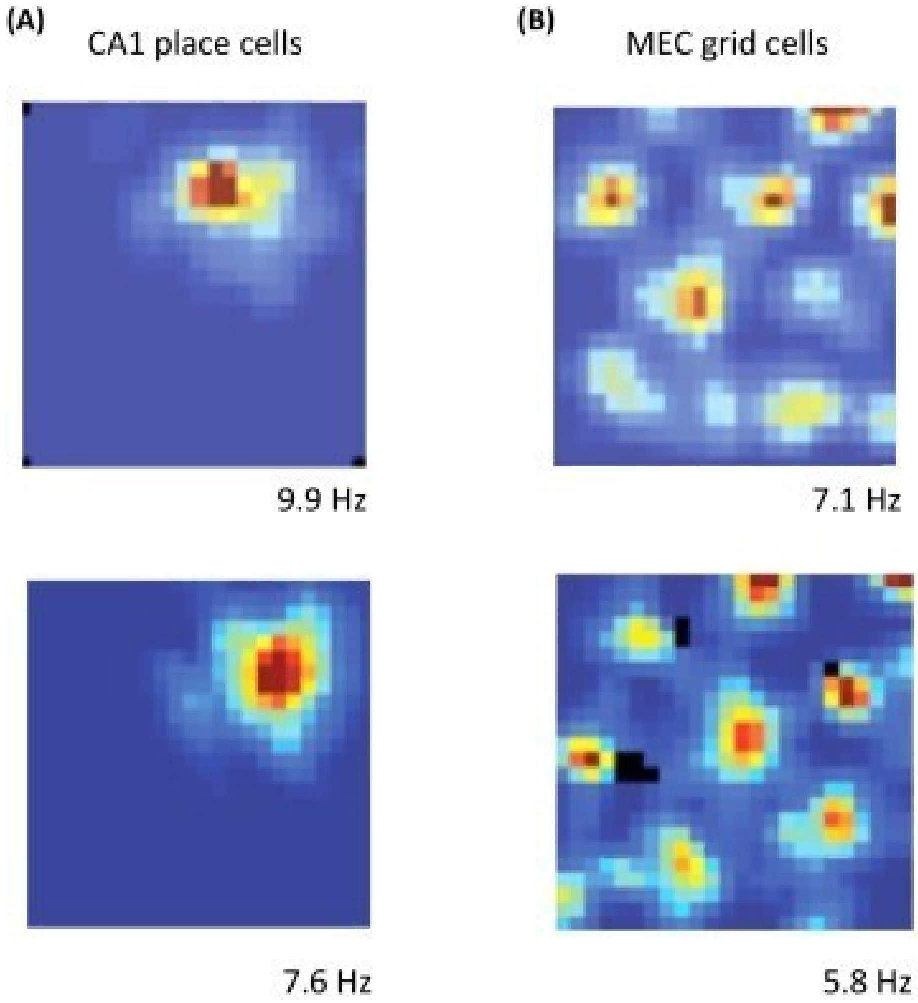

Figure 1.5: Example of cells that represent location. **A)** Example of two place cells in the CA1 portion of the hippocampus. **B)** Example of two grid cells from the medial entorhinal cortex (MEC). Adapted from [43].

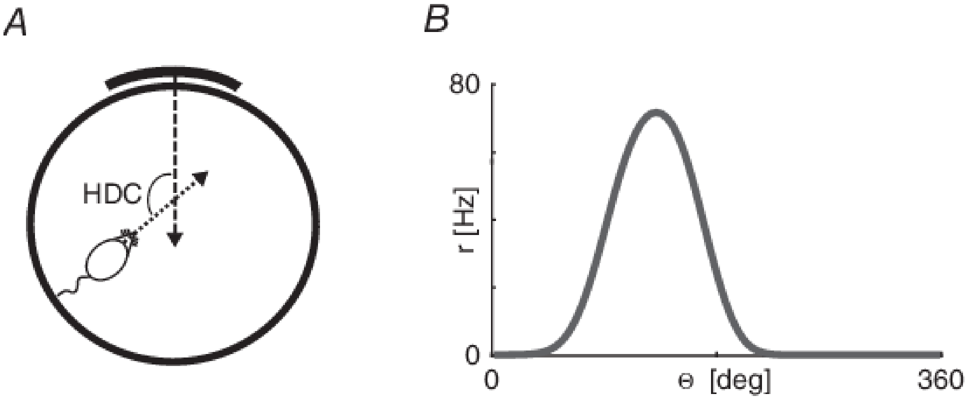

Figure 1.6: Example head direction cell responses. **A)** Position of animal relative to the cue. HDC: Head Direction Cell **B)** Schematic of a tuning curve from a head direction cell. Adapted from [46].

preferentially fire when an animal is facing a specific direction in its environment and serve as the final piece to allow for successful navigation [48]. The combination of these three cell types allows animals to know their location, as well as to formulate a trajectory to get to a target location.

A confluence of sensory information drives the creation and updating of these internal maps to ensure that they faithfully represent changing environments. Vision has been demonstrated to be particularly important for navigation, exerting a dominating influence over other sensory modalities [49]. However, how visual information is specifically integrated into the areas responsible for navigation is not well understood.

1.3 Disorders affecting the visual system

Although complete blindness is relatively rare, severe uncorrectable vision loss, which can profoundly affect daily life, affects approximately 4 million Americans. Blindness can be caused by damage to the visual cortex, but this is generally rare. More commonly, visual impairments are a result of some kind of damage to the eye or retina. Some of these disorders, such as cataracts and diabetic retinopathy, have understood mechanisms and successful treatment options. On the other hand, other diseases, particularly ones that degenerate photoreceptors such as retinitis pigmentosa and age-related macular degeneration, have been more difficult to treat [50, 51]. Although the symptoms of these diseases are well defined, both the molecular and cellular mechanisms, as well as potential treatment and prevention options, are still unclear.

1.4 Summary and motivation

In the past decade, the mouse visual system has emerged as an important model for studying sensory processing and transformation into important ethologically relevant information. Although there has been significant research into how visual information travels from the retina through the LGN to V1, our understanding of how this information is processed in the HVAs and beyond is unclear. Here, we use optical physiology to simultaneously record from hundreds of neurons in awake mice to study how visual stimuli are processed and transformed from V1 onward. First, we sought to understand how the neural representation of coherent motion, a specific type of stimulus motion, is organized and represented in the visual cortex of mice. Next, we studied how the processed information from HVAs is combined with other cognitive variables in the HD network to update an animal's internal sense of direction. Last, we studied the effects of retinoic acid inhibitors on a mouse model of photoreceptor degeneration, examining visual responses at multiple scales, including retinal, cortical, and behavioral. These studies shed light on how the rodent cortex transforms sensory stimuli to a suitable representation for higher cognitive processes, such as navigation.

1.5 Permissions and attributions

1. The contents of chapter 2 have been published in the journal *Nature Communications* [52].

2. The contents of chapter 3 have been uploaded as a preprint to *biorXiv* [53].

3. The contents of chapter 4 have been published in the journal *Science Advances* [54] and were the results of a collaboration with Dr. Richard Kramer's lab at UC Berkeley. The Kramer lab performed the retinal electrophysiology and behavioral testing. The Goard lab performed all calcium imaging and related analyses.

Chapter 2

Distributed and retinotopically asymmetric processing of coherent motion in mouse visual cortex

2.1 Preface

Perception of visual motion is important for a range of ethological behaviors in mammals. In primates, specific visual cortical regions are specialized for processing of coherent visual motion. Coherent visual motion is defined as motion that is characterized by coherent net movement across the visual field, even if individual parts of the visual field are moving in different directions. This type of motion is particularly important for navigation, for example detecting optic flow and inferring movement from purely visual information. Despite powerful genetic tools available for measuring population neural activity, whether mouse visual cortex has a similar organization of coherent motion responsive areas remains unclear. Here, we use widefield and 2-photon calcium imaging of transgenic mice to measure mesoscale and cellular responses to coherent motion. Imaging of primary visual cortex (V1) and higher visual areas (HVAs) during presentation of natural movies and random dot kinematograms (RDKs) reveals varied responsiveness to coherent motion, with stronger responses in dorsal stream areas compared to ventral stream areas. Moreover, there is considerable anisotropy within visual areas, such that neurons representing the lower visual field are more responsive to coherent motion. These results indicate that processing of visual motion in mouse cortex is distributed heterogeneously both across and within visual areas.

2.2 Introduction

Perception of visual motion is critical for animal survival, underlying behaviors such as visually guided navigation, pursuit of prey, and avoidance of threats. Although neurons selective for visual motion arise early in the visual system, extensive research in primates has shown that perception of coherent global motion independent of local motion relies on processing in specialized regions of visual cortex [55, 56]. Although mouse visual cortical neurons are known to be well-tuned for coherent visual motion [57, 58], and vision plays an important role in navigation [59], mesoscale cortical processing of coherent motion is poorly understood in the mouse. Recently developed techniques for measuring neural activity in genetically identified neurons makes the mouse an attractive model system for investigating cortical processing of coherent motion at previously inaccessible spatial scales [39, 60]. Although visually driven neurons along the retinogeniculocortical pathway of mice and primates exhibit differences in response properties and connectivity [61], there are parallels in the overarching meso- and macroscale organization of the visual areas [39]. Researchers are just beginning to understand how coherent motion is encoded in the mouse visual system, and the degree to which circuits underlying motion processing are homologous between mice and primates.

In primates, the middle temporal area (MT) and the downstream medial superior temporal area (MST) have been identified as specialized regions for processing of coherent motion [29], and are key regions in the dorsal stream of visual processing [62, 63]. Area MT contains a high proportion of direction-selective neurons [64, 65, 66] and preferentially receives direction-selective inputs from the primary visual cortex (V1) [67]. Pharmacological lesioning of MT causes deficits in coherent motion perception [68], and microstimulation of MT can influence perception of motion in studies using random dot kinematograms (RDKs) [69]. Individual neurons in MT and MST exhibit strong direction-selective responses to RDKs and many are selective for the overall motion of plaid stimuli (pattern direction-selective) rather than to the individual component gratings (component direction-selective) [29]. In contrast, neurons in the primate V1 are mostly nonselective for the direction of coherent motion in RDKs [70] and exclusively exhibit component direction-selective responses to plaids [29]. These findings have led to models in which MT response properties derive from weighted summation and normalization of direction-selective V1 inputs [71, 72].

The basic organization of mouse visual cortex is similar to the primate visual system, with the majority of cortical input arriving via the retinogeniculocortical pathway (along with indirect input from the superior colliculus via the lateral posterior nucleus of the thalamus [22]), and a network of hierarchically organized visual cortical regions with independent retinotopic maps [73, 74, 75]. However, the mouse visual system has several functional properties that are distinct from that of primates. For example, several types of mouse retinal ganglion cells (RGCs) exhibit direction selectivity [2, 76, 77], while direction-selective RGCs have not been found in primate retina [78]. Direction-selective RGCs have an asymmetric retinotopic distribution [79, 80], give rise to direction-selective inputs to visual cortex [81], and influence direction selectivity in visual cortex [82]. In addition, strong orientation tuning and direction selectivity are already present in the lateral geniculate nucleus [83, 84, 85], in contrast to the weakly tuned LGN neurons found in primates [86]. Finally, in contrast to primate V1 [29, 70], mouse V1 contains a significant fraction of neurons that exhibit tuned responses to global coherent motion found in RDKs [57] and plaid pattern motion [87, 88] (though see [89]).

In recent years, mapping procedures using intrinsic signal imaging [74, 75, 90] and wide-field calcium imaging [91, 92] have allowed researchers to define and functionally characterize higher visual areas (HVAs) in intact mice, but the functional role of the HVAs and any homology to primate visual structures remains an area of active investigation. Anatomical and functional studies have found that HVAs are broadly connected into two subnetworks with projection patterns similar to primate ventral and dorsal streams [90, 41, 93, 42]. Specifically, the lateral medial (LM) and lateral intermediate (LI) areas preferentially project to temporal and lateral entorhinal cortices (putative ventral stream) while the anterolateral (AL), posterior medial (PM), rostrolateral (RL), and anteromedial (AM) areas preferentially project to parietal, motor, and medial entorhinal cortices (putative dorsal stream). Consistent with this classification, measurements of single neuron activity indicated greater direction selectivity in regions AL, RL, and AM [74] (though see [75]), a hallmark of dorsal stream regions in primate [64, 65, 66].

Here, we use wide-field and two-photon calcium imaging to map areal and cellular responses to coherent motion in mouse visual cortices using both natural movies and RDKs. We find that HVAs exhibit heterogeneous responses to coherent motion as in primates, with stronger activation in response to coherent motion in regions AL, PM, and AM compared with V1, LM, and LI. However, responses to coherent motion are much more distributed than in primate, with neurons in all measured regions (including V1) exhibiting some degree of coherent motion responsiveness. Furthermore, coherent motion responses are distributed asymmetrically across visual elevation, both within and across all visual regions, with neurons representing the lower visual field exhibiting much stronger coherent motion responses. Taken together, these results show that the mouse visual cortex is optimized for distributed processing of lower field motion, potentially enhancing processing of optical flow signals during movement.

2.3 Methods

2.3.1 Animals

For cortex-wide calcium indicator expression, Emx1-Cre (Jax Stock #005628) × ROSA-LNL-tTA (Jax Stock #011008) × TITL-GCaMP6s (Jax Stock #024104) triple transgenic mice ($n = 25$) were bred to express GCaMP6s in cortical excitatory neurons. For wide-field and two-photon imaging experiments, 6- to 12-week-old mice of both sexes (10 males and 15 females) were implanted with a head plate and cranial window and imaged starting 2 weeks after recovery from surgical procedures and up to 10 months after window implantation. The animals were housed on a 12 h light/dark cycle in cages of up to 5 animals before the implants, and individually after the implants. All animal procedures were approved by the Institutional Animal Care and Use Committee at UC Santa Barbara.

2.3.2 Surgical procedures

All surgeries were conducted under isoflurane anesthesia (3.5% induction, 1.5–2.5% maintenance). Prior to incision, the scalp was infiltrated with lidocaine (5 mg kg^{-1}, subcutaneous) for analgesia and meloxicam (1 mg kg^{-1}, subcutaneous) was administered pre-operatively to reduce inflammation. Once anesthetized, the scalp overlying the dorsal skull was sanitized and removed. The periosteum was removed with a scalpel and the skull was abraded with a drill burr to improve adhesion of dental acrylic. A 4 mm craniotomy was made over the visual cortex (centered at 4.0 mm posterior, 2.5 mm lateral to Bregma), leaving the dura intact. A cranial window was implanted over the craniotomy and sealed first with silicon elastomer (Kwik-Sil, World Precision Instruments) then with dental acrylic (C&B-Metabond, Parkell) mixed with black ink to reduce light transmission. The cranial windows were made of two rounded pieces of coverglass (Warner Instruments) bonded with a UV-cured optical adhesive (Norland, NOA61). The bottom coverglass (4 mm) fit tightly inside the craniotomy while the top coverglass (5 mm) was bonded to the skull using dental acrylic. A custom-designed stainless-steel head plate (eMachineShop.com) was then affixed using dental acrylic. After surgery, mice were administered carprofen (5 mg kg^{-1}, oral) every 24 h for 3 days to reduce inflammation. The full specifications and designs for head plate and head fixation hardware can be found on our institutional lab website (`https://labs.mcdb.ucsb.edu/goard/michael/content/resources`).

2.3.3 Visual stimuli

All visual stimuli were generated with a Windows PC using MATLAB and the Psychophysics toolbox [94]. Stimuli used for wide-field visual stimulation were presented on an LCD monitor (43 × 24 cm, 1600 × 900 pixels, 60 Hz refresh rate) positioned 10 cm from the eye at a 30° angle to the right of the midline, spanning 130° (azimuth) by 100° (elevation) of visual space. The monitor was placed 3 cm above 0° elevation and tilted 20° downward to ensure that the monitor was as equidistant as possible from the mouse's eye. For two-photon imaging of single-cell responses, visual stimuli were presented on an LCD monitor (17.5 × 13 cm, 800 × 600 pixels, 60 Hz refresh rate) positioned 5 cm from the eye at a 30° angle right of the midline, spanning 120° (azimuth) by 100° (elevation) of visual space. This monitor was also positioned 3 cm above 0° elevation and tilted 20°

downward.

Retinotopic mapping stimuli consisted of a drifting bar that was spherically corrected to account for visual field distortions due to the proximity of the monitor to the mouse's eye [74]. A contrast-reversing checkerboard was presented within the bar to better drive neural activity (0.05 cycles degree^{-1} spatial frequency; 2 Hz temporal frequency). The bar smoothly drifted at 10.8° s^{-1} and had a width of 8° of visual field space for elevation and 9° of visual field space for azimuth. The stimulus was swept in the four cardinal directions: left to right, right to left, bottom to top, and top to bottom, repeated 20–60 times.

Natural movies were a set of 22 home cage movies recorded from mice with head-mounted cameras provided by Froudarakis and Tolias [95]. Each movie had a duration of 10 s and was presented at a frame rate of 30 Hz. For each experiment, three movies were randomly selected from a pool of all movies and presented for 20 repeats in random order.

Random dot kinematograms (RDKs) consisted of black dots presented on a 50% gray screen [96]. Each dot had a diameter of 2° of visual space, and the number of dots was adjusted so that the screen was 20% occupied by dots. Dots moved at a speed of 80° s^{-1} in a randomly assigned direction (0° - 315°, in 45° increments), and had a lifetime of 60 frames. A subset of these dots (3, 6, 12, 24, 48, or 96%) had their directions adjusted to the same direction to create coherent motion within the random dot motion. The coherent motion trace, which dictates the amount of coherence in the stimulus, was randomly generated at the beginning of the stimulus presentation and remained constant across repeats. Other stimulus features such as coherence direction and dot position were randomized across trials in order to eliminate reliable responses to all visual features except coherent motion. For wide-field stimulation, a square wave coherence trace consisting of a pseudorandom presentation of all coherence values was created for each experiment, with motion direction changing across repeats. For two-photon stimulation, a short pseudorandom coherence trace was generated, with coherence changing smoothly between target coherence values, and the RDK stimulus was repeated multiple times in different motion directions to allow measurement of directional tuning. A 2 s blank gray screen preceded each trial, and the stimulus was repeated for 10 - 20 trials. For a subset of experiments, the RDKs were spherically corrected with the same parameters as for the retinotopic mapping stimuli.

To map azimuth and elevation preferences, full screen length bars (width $= 20^\circ$) of a contrast-reversing checkerboard (spatial frequency of 0.04 cycles degree^{-1}; temporal frequency $= 5$ Hz) were displayed on a 50% gray screen. There were 30 overlapping bar locations for horizontal bars (elevation mapping) and 40 overlapping bar locations for vertical bars (azimuth mapping). The bar appeared at each location in random order for 1 s, with a 2 s gray screen between repeats. Wide-field imaging

After > 2 weeks of recovery from surgery, GCaMP6s fluorescence was imaged using a custom wide-field epifluorescence microscope. The full specifications and parts list can be found on our institutional lab website (`https://labs.mcdb.ucsb.edu/goard/michael/content/resources`). In brief, broad spectrum (400 - 700 nm) LED illumination (Thorlabs, MNWHL4) was band-passed at 469 nm (Thorlabs, MF469-35), and reflected through a dichroic (Thorlabs, MD498) to the microscope objective (Olympus, MVPLAPO 2XC). Green fluorescence from the imaging window passed through the dichroic and a bandpass filter (Thorlabs, MF525-39) to a scientific CMOS (PCO-Tech, pco.edge 4.2). Images were acquired at 400×400 pixels with a field of view of 4.0×4.0 mm, leading to a pixel size of 0.01 mm pixel^{-1}. A custom light blocker affixed to the head plate was used to prevent light from the visual stimulus monitor from entering the imaging path.

2.3.4 Wide-field post-processing

Images were acquired with pco.edge camera control software and saved into multi-page TIF files. All subsequent image processing was performed in MATLAB (Mathworks). The ΔF/F for each individual pixel of each image frame was calculated as:

$$\Delta F/F = (F_{\mathrm{x,y,n}} - \tilde{F}_{\mathrm{x,\,y}})/\tilde{F}_{\mathrm{x,\,y}} \tag{2.1}$$

where $F_{\mathrm{x,y,n}}$ is the fluorescence of pixel (x, y) at frame n, and $\tilde{F}_{\mathrm{x,\,y}}$ is defined as the median raw fluorescence value across the entire time series for pixel (x, y). Subsequent analyses were performed on whole-frame $\Delta F/F$ matrices. Identifying HVAs using wide-field retinotopic mapping

For identification of HVAs, responses to drifting bar stimuli were averaged across each stimulus (horizontal left to right, horizontal right to left, vertical bottom to top, vertical top to bottom)[97]. Next, for each pixel, the phase of the first harmonic of the 1D Fourier transform was calculated to create retinotopic maps (phase maps) for each direction, which were then phase-wrapped to ensure smooth phase transitions between pixels. Last, to remove the delay due to the rise time of the GCaMP6s signal, phase maps of opposite directions (forward vs backward, upward vs downward) were subtracted from one another [97].

Visual field sign maps were derived from the sine of the angle between the gradients in the azimuth and elevation phase maps. The resulting sign maps underwent a standard post-processing procedure [89, 92]: sign maps were first smoothed and thresholded, then each sign patch was dilated to fill in gaps between areas. Next, we applied an iterative splitting and merging process to further refine maps. First, each patch was checked for redundant coverage of visual space, and if significant redundancy (>10% shared visual field coverage) was found, the patch was split to create two separate patches. Conversely, adjacent same-sign patches were merged if they had little redundancy (<10% shared visual field coverage). After processing, borders were drawn around each patch, and resulting patches were compared against published sign maps for both size and sign to label each patch as a visual area. Visual areas V1, LM, AL, PM, LI, RL, and AM were present in all mice (Supplementary Fig. 2).

2.3.5 Analysis of natural movie and RDK stimuli

For natural movie reliability maps, we calculated the reliability of each pixel according to the following formula:

$$R_{\mathrm{x,\ y}} = \sum_{t=0}^{T} CC(r_{\mathrm{x,\ y,\ t}}, \bar{r}_{\mathrm{x,\ y,\ [0,\ T]} \neq \mathrm{t}})/T \tag{2.2}$$

where R is reliability for pixel (x, y), t is the trial number from $[0, T]$, CC is the Pearson correlation coefficient, $r_{\mathrm{x,\ y,\ t}}$ is the response of pixel (x, y) on trial t, and $\bar{r}_{\mathrm{x,\ y,\ [0,\ T]} \neq \mathrm{t}}$ is the average response of pixel (x, y) on all trials excluding trial t.

For calculating coherent motion in natural movies, the pixel-wise motion vectors for each frame were calculated using the MATLAB optical flow toolbox (Mathworks). In brief, the motion vectors are calculated per pixel by analyzing the spatiotemporal changes in brightness via the Horn–Schunck method. For each frame, the component vectors for each pixel were summed, and the magnitude of the summed component vectors was defined as the value of coherent motion for that frame.

In order to determine the uniformity of motion energy across the frame (Figure 2.6), we first calculated mean motion magnitude maps by taking the magnitude of each pixel's motion vector for each frame, then meaning all resulting frames across a single movie. The uniformity of this image was gauged with a uniformity index, based on the ANSI standard for image uniformity. Briefly, the image is first divided into nine equal sections, which tile the image. The average brightness of each area is calculated. The uniformity index is then calculated as follows:

$$\text{Uniformity index} = 1 - \frac{B_{\text{max}} - B_{\text{min}}}{B_{\text{max}} + B_{\text{min}}} \tag{2.3}$$

where B is the brightness of each section. Higher uniformity index values denote a more even image. As the "brightness" of each pixel in the mean magnitude map denotes the strength of motion information, a high uniformity index signifies even motion information across the screen.

For natural movies and RDKs, the coherent motion correlation of each pixel was calculated as the correlation of the mean response of the pixel and the coherent motion of the presented stimulus:

$$M_{\text{x, y}} = CC(\bar{r}_{\text{x, y}}, m) \tag{2.4}$$

where $M_{\text{x, y}}$ is the coherent motion response for pixel (x, y), CC is the Pearson's correlation coefficient, $\bar{r}_{\text{x, y}}$ is the average adjusted $\Delta F/F$ response for pixel (x, y), and m is the coherence value of the stimulus.

Regions of interest for seven visual areas (V1, LM, AL, PM, LI, RL, and AM) were individually defined for each mouse using the mouse-specific sign map as described above [90]. Pixels within each defined area were averaged to compare areal responses across all imaged mice.

The retinotopic dependence of coherent motion correlations was calculated as the correlation between the retinotopic preference (elevation or azimuth) and the coherent motion correlation for all pixels within each area. Density plots were created using scatplot (MATLAB Central File Exchange). Briefly, a subsampled scatter plot was first created, then turned into a Voronoi diagram. The density of points within each Voronoi cell centered on the subsampled scatter plot was used to determine the density of the distribution in that portion of the scatter plot.

2.3.6 Two-photon imaging

After > 2 weeks recovery from surgery, GCaMP6s fluorescence was imaged using a Prairie Investigator two-photon microscopy system with a resonant galvo-scanning module (Bruker). Prior to two-photon imaging, epifluorescence imaging was used to identify the visual area being imaged by aligning to areal maps measured with wide-field imaging.

For fluorescence excitation, we used a Ti:Sapphire laser (Mai-Tai eHP, Newport) with dispersion compensation (Deep See, Newport) tuned to $\Lambda = 920$ nm. For collection, we used GaAsP photomultiplier tubes (Hamamatsu). To achieve a wide field of view, we used a 16× / 0.8NA microscope objective (Nikon) at 1× (850 × 850µm or 2 × ($425 \times 425 \mu m$) magnification. Laser power ranged from 40 to 75 mW at the sample depending on GCaMP6s expression levels. Photobleaching was minimal ($< 1\%\text{min}^{-1}$) for all laser powers used. A custom stainless-steel light blocker (eMachineShop.com) was mounted to the head plate and interlocked with a tube around the objective to prevent light from the visual stimulus monitor from reaching the PMTs. During imaging experiments, the polypropylene tube supporting the mouse was suspended from the behavior platform with high tension springs (Small Parts) to reduce movement artifacts.

2.3.7 Two-photon post-processing

Images were acquired using PrairieView acquisition software and converted into TIF files. All subsequent analyses were performed in MATLAB (Mathworks) using custom code (`https://labs.mcdb.ucsb.edu/goard/michael/content/resources`). First, images were corrected for X–Y movement by registration to a reference image (the pixel-wise mean of all frames) using 2-dimensional cross correlation.

To identify responsive neural somata, a pixel-wise activity map was calculated using a modified kurtosis measure. Neuron cell bodies were identified using local adaptive threshold and iterative segmentation. Automatically defined ROIs were then manually checked for proper segmentation in a graphical user interface (allowing comparison to raw fluorescence and activity map images). To ensure that the response of individual neurons was not due to local neuropil contamination of somatic signals, a corrected fluorescence measure was estimated according to:

$$F_{\mathrm{corrected}}(n) = F_{\mathrm{soma}}(n) - \alpha(F_{\mathrm{neuropil}}(n) - \overline{F}_{\mathrm{neuropil}}) \tag{2.5}$$

where F_{neuropil} was defined as the fluorescence in the region $< 30\mu\mathrm{m}$ from the ROI border (excluding other ROIs) for frame n. $\overline{F}_{\mathrm{neuropil}}$ is $F_{neuropil}$ averaged over all frames. α was chosen from [01] to minimize the Pearson's correlation coefficient between $F_{\mathrm{corrected}}$ and F_{neuropil}. The $\Delta F/F$ for each neuron was then calculated as:

$$\Delta F/F = (F_{\mathrm{n}} - F_0)/F_0 \tag{2.6}$$

where F_n is the corrected fluorescence ($F_{corrected}$) for frame n and F_0 defined as the mode of the corrected fluorescence density distribution across the entire time series.

2.3.8 Analysis of two-photon imaging data

To map azimuth and elevation preferences, responses were measured during presentation of horizontal or vertical bars containing an alternating checkerboard stimulus. To identify neurons as visually responsive, a one-way ANOVA was first performed to screen for significantly preferential responses for specific stimulus locations. For neurons passing this criterion, we fit the responses with a 1D Gaussian model to determine the preferred azimuth and elevation. Finally, the receptive field preference of all significantly responding neurons in the imaging field were correlated to their pixel distance from the edge of the screen to ensure that the imaged neurons had receptive fields on the screen, and that the retinotopic preference correlated with the anatomical axis of azimuth/elevation (to ensure that the imaging field did not cross areal boundaries). Sessions that failed to exhibit a correlation between receptive field preference and pixel distance along the retinotopic axis were not used for further analysis. The cutoff for correlation was calculated for each recorded field by shuffling the cell locations 5000 times and calculating the correlation between receptive field preference and shuffled pixel distance to probe the underlying distribution. The 99th percentile of the shuffled distribution was then chosen as the threshold correlation, and sessions whose calculated correlations were below this value were discarded

For analysis of single neurons to RDKs, we analyzed responses to different motion directions separately. We first only used the motion direction that produced the highest Pearson correlation coefficient between the neural response and the coherent motion signal, as responses to null directions were generally weak. However, to calculate the net preferred direction of the neuron, we treated the coherent motion responses to each direction as a vector and calculated the vector sum of all vectors. The orientation of the resultant vector was defined as the preferred direction of that neuron.

For measuring coherent motion correlations by area, we imaged fields of neurons at 2× magnification (425 µm × 425 µm) in identified visual areas, as identified in wide-field visual field sign maps. We then compared distributions of single-cell coherent motion correlation across areas. For measuring the relationship of coherent motion correlations to retinotopy in single neurons, we calculated the correlation coefficient between the coherent motion correlation and the preferred elevation.

2.3.9 Eye tracking and center of gaze analyses

To confirm the center of the gaze of the mouse relative to the stimulus monitor, we performed eye tracking experiments on three mice. These mice were head-fixed identically to imaging experiments, but an IR camera (Thorlabs DCC1645C with IR filter removed; Computar T10Z0513CS 5–50 mm f/1.3 lens) was placed such that the image sensor was located exactly at the center of the stimulus monitor. Video was acquired at 10 fps and images were analyzed offline in MATLAB (Mathworks).

First, the pupil was identified for each frame using an automated procedure. In brief, raw images were binarized based on pixel brightness, and the resulting images were morphologically cleaned by removing isolated pixels. For the initial frame, the pupil was manually chosen. For subsequent frames, the pupil was chosen from potential low intensity regions based on a linear combination of size, location, and eccentricity of the pupil in the previous frame. We next calculated the vector that passed through the center of the mouse's eyeball and the center of the pupil for each frame [98]. Extrapolating this vector to the stimulus monitor distance provided a measurement of the center of gaze of the mouse on the stimulus monitor at each frame.

2.3.10 Statistical information

To test statistical significance of single groups, single-sample Student's t tests were performed. Because most of the groups were uneven in sample size, unpaired two-sample t tests were used exclusively. To calculate effect size where applicable, Hedges' g was calculated due to uneven group sizes. All t tests were performed as two-tailed t tests. Where applicable, a Bonferroni correction was applied to adjust the p-value significance threshold.

2.4 Results

2.4.1 Mouse visual cortex has heterogeneous responses to motion

In order to measure neural responses to coherent motion in an unbiased manner across the visual cortex, we used a custom wide-field microscope (Figure 2.3A) to measure calcium responses through a 4-mm diameter window located over the left visual cortex of awake, head-restrained mice expressing the calcium indicator GCaMP6s in excitatory neurons (Emx1-Cre::Rosa-tTA::TITL-GCaMP6s [99, 100]). We displayed visual stimuli on a screen that was placed on the optical axis of the right eye, such that the center of gaze was centered on the display monitor (Figure 2.1, see Methods).

Using established mapping procedures for defining HVAs [74, 90] that were adapted for calcium imaging [91, 92], we determined the areal boundaries of primary visual cortex (V1) and six consistently identified HVAs: LM, AL, PM, LI, RL, and AM (Figure 2.3B), ordered by their approximate position in the visual hierarchy [93]. As in some previous studies, we were unable to consistently locate area A independent of AM [90], so this area was excluded from our analyses. This procedure was performed separately for each mouse to obtain a precise map of each mouse's visual cortical areas (Figure 2.2).

To determine which areas responded to complex visual input, we displayed repeated presentations of sets of natural movies recorded from a head-mounted camera [95] (Figure 2.3C) on a large monitor subtending 130° azimuth (0 - 130° nasal to temporal) and 100° elevation (-50° to +50° lower to upper) of the contralateral visual field. Calcium responses from individual pixels in visual cortex exhibited reliable responses to repeated presentations of the natural movies (Figure 2.3D). To reduce inter-mouse variability and hemodynamic artifacts from blood vessels, we aligned HVA area boundaries and averaged

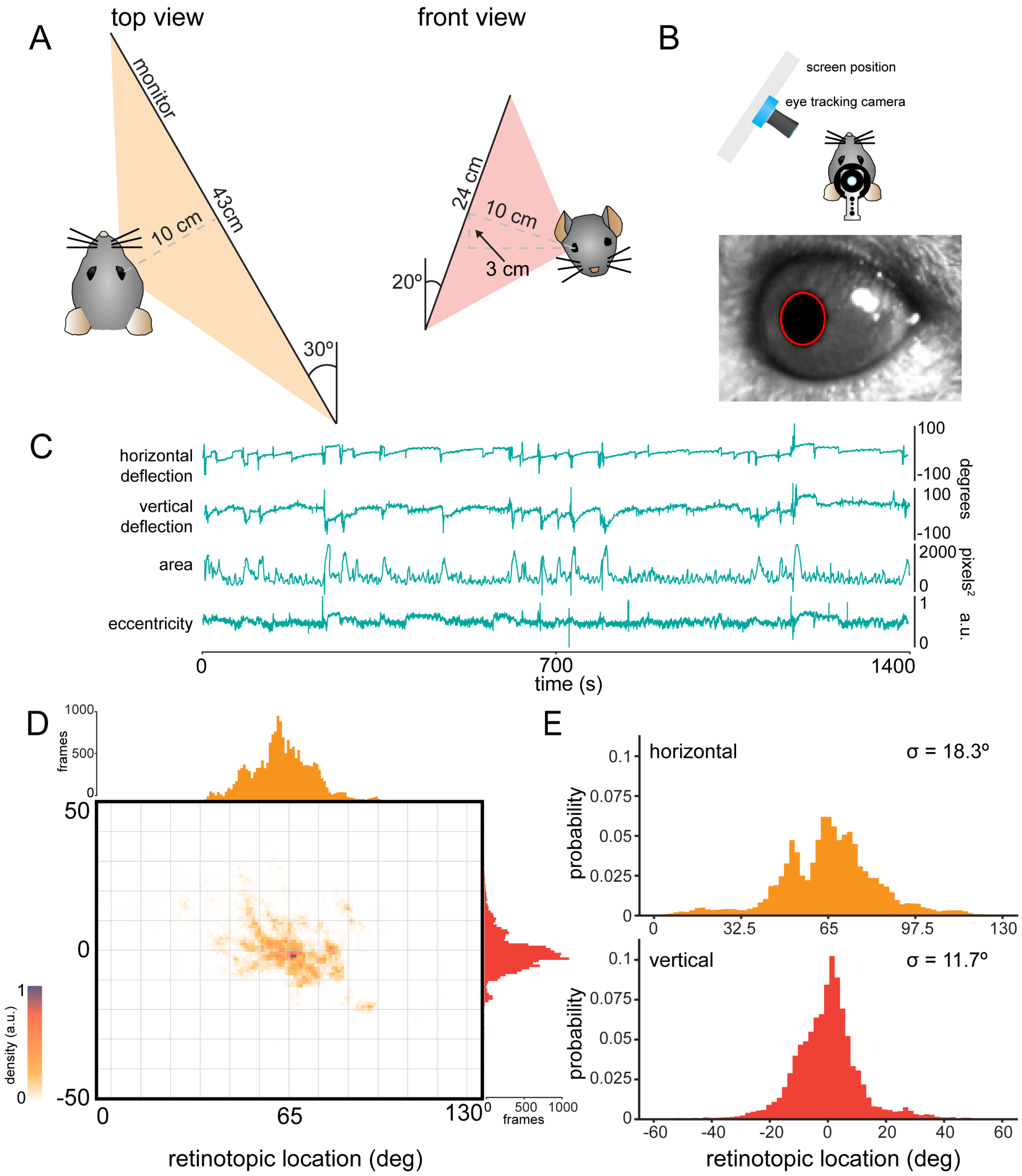

Figure 2.1: Positioning of stimulus monitor and center of gaze tracking. **A)** Schematic of monitor placement in front of the mouse from the top and front views (see Methods). **B)** Schematic of the eye-tracking camera position (top) and an example image (bottom) with the identified pupil circled in red. **C)** Example traces over a 1400 s eye-tracking recording, showing the horizontal deflection, vertical deflection, area, and eccentricity of the detected pupil. **D)** Density map of center of gaze across the recording for a single mouse. The histograms on the top and right edges of the density map represent the distribution of deflection for azimuth and elevation, respectively. **E)** Combined probability density histograms across all recorded mice (n = 3).

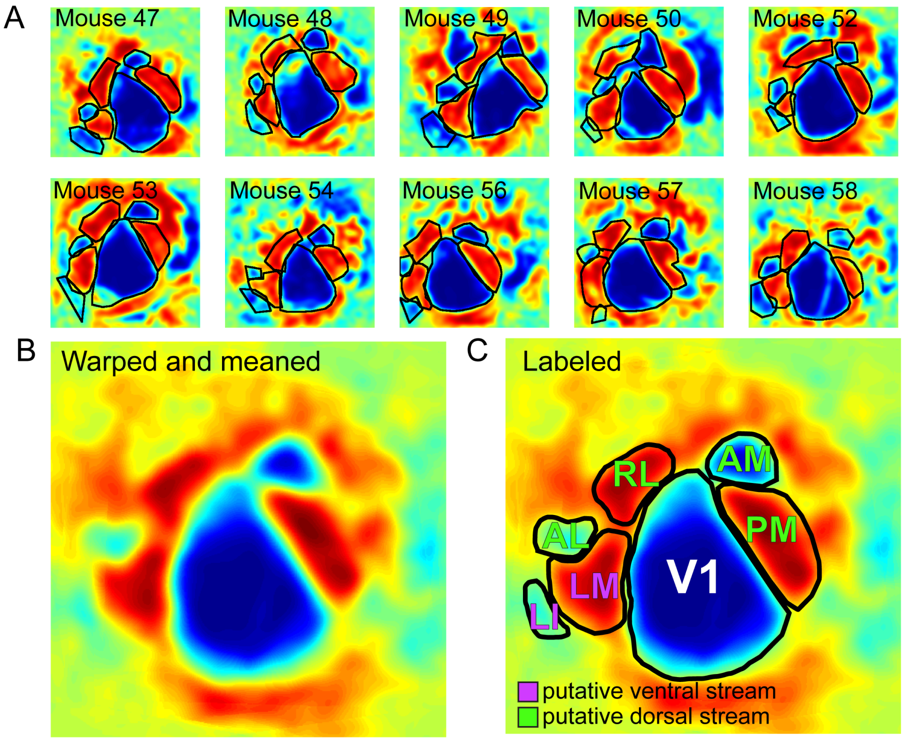

Figure 2.2: Visual field sign maps from all imaged mice. **A)** Sign maps for each of ten mice used in both widefield RDK and natural movie experiments. All sign maps contain boundaries which define the eight areas analyzed (V1, LM, PM, AL, LI, RL, AM, and S1). **B)** Warped and averaged sign maps of all mice. **C)** Same as in (B), but with areal boundaries and labels included. The putative mouse ventral and dorsal streams are designated in green and magenta, respectively.

reliability across multiple mice (Figure 2.3e; n = 19 sessions across 7 mice), revealing that primary visual cortex exhibited uniformly reliable responses across the region. Response reliability was slightly weaker in secondary visual regions LM and PM, and weaker still in higher areas of the visual hierarchy such as AL, RL, and AM (Figure 2.4).

We next investigated whether the responses to the motion energy embedded within the natural movies were similarly uniform across areas, or if the mouse exhibits heterogeneity across HVAs as has been observed in primate MT/MST. To this end, we first calculated the total motion energy for each frame of the natural movie by first calculating pixel-by-pixel motion vectors, then taking the vector sum across each frame (Figure 2.3F; see Methods). We next measured the Pearson correlation between the deconvolved neural response for each pixel and the motion energy of the scene (Figure 2.3G, bottom; see Methods). In both individual sessions (Figure 2.3G, top) and aligned session averages (Figure 2.3H; n = 19 sessions across 7 mice), we found that particular cortical locations were strongly driven by motion embedded in the scene. The motion correlation map (Figure 2.3H) was not well correlated to the map of reliability to all visual features (Figure 2.3E), as evident by the low pixel-wise correlation between motion response and reliability (Figure 2.5; r = 0.088 ± 0.12, $t_{17} = 0.08$, $p = 0.47$, mean ± s.e.m., single-sample t test).

One possibility for the anisotropic distribution of motion responses in visual cortex is that motion energy is not uniformly distributed in the natural movies. Indeed, individual natural movies exhibit non-uniform distributions of motion energy (Figure 2.6), though the average motion energy across all natural movies is roughly uniform (Figure 2.6). To further ensure that the distribution of motion energy is unbiased across the visual field, and to remove the influence of other features driving neural responses, we used full screen random dot kinematograms (RDKs) to measure responses to coherent motion across the visual field (Figure 2.7a; see Methods).

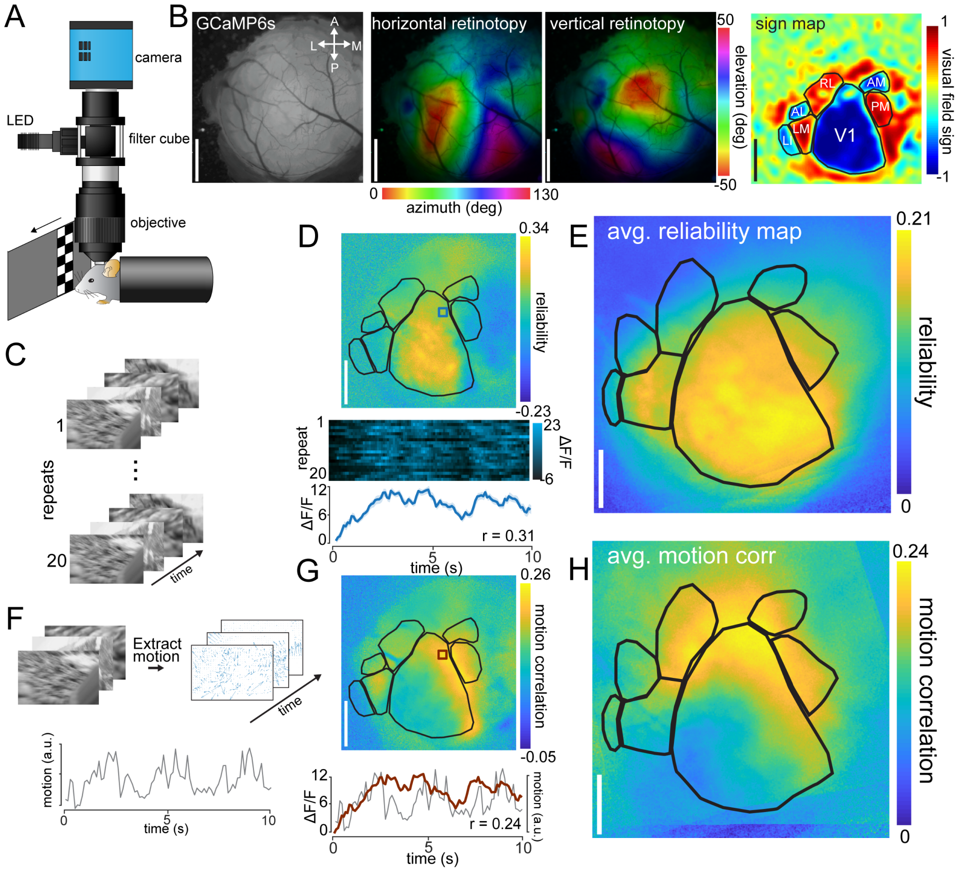

Figure 2.3: Mesoscale calcium responses to motion energy in natural visual stimuli. **A)** Schematic of the custom epifluorescent wide-field microscope for in vivo GCaMP6s imaging. **B)** Areal maps from one session of a single example mouse. Left: surface raw fluorescence image of a 4 mm cortical window of example Emx1-GCaMP6s mouse. Middle: horizontal and vertical retinotopic maps. Right: sign map, and resulting segmentation of visual cortex into V1 and HVAs. Scale bars = 1 mm. **C)** Schematic of the natural movie stimulus. Scenes were repeated 20 times to measure reliable neural responses. **D)** Top: map from a single experiment showing reliability across posterior cortex; visual area segmentation as in (B). Bottom: multi-trial response (20 repeats) and mean trace (± s.e.m. shaded) of a single pixel (blue square) to repeated presentation of the natural movie. **E)** Mean reliability map across all imaged mice (n = 19 sessions over 7 mice). Individual maps are transformed onto a common coordinate system for comparison across mice. **F)** Extraction of the motion energy in the stimulus. **G)** Top: map from a single experiment showing motion response across posterior cortex; visual area segmentation as in (B). Bottom: Neural response of a single pixel (red) overlaid on the motion trace (gray). **H)** Mean motion energy correlation map across all imaged mice (n = 19 sessions over 7 mice); alignment procedure same as (E). Area abbreviations: primary visual (V1), lateral medial (LM), anterolateral (AL), posterior medial (PM), laterointermediate (LI), rostrolateral (RL), and anteromedial (AM).

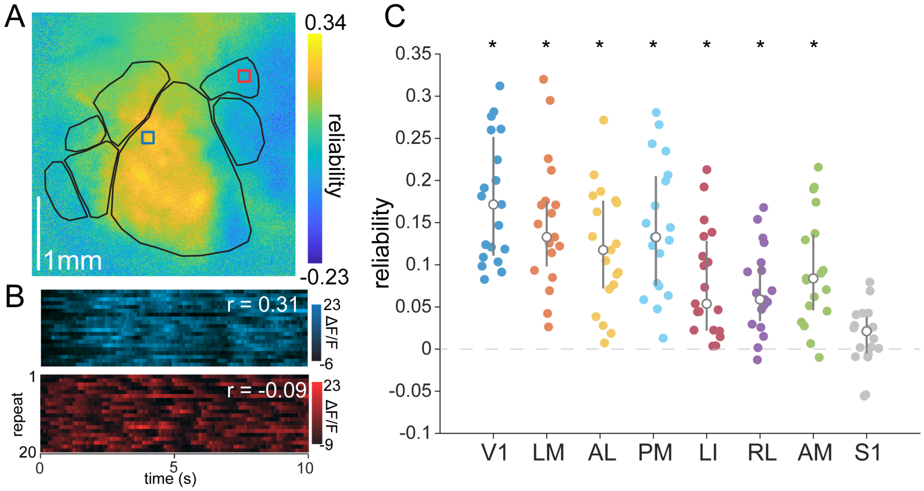

Figure 2.4: Natural movie reliability across mouse visual cortex **A)** Map of reliability to natural movie stimuli. **B)** Two example pixels from the labeled boxes in (A). The blue pixel shows from area V1 shows high reliability; whereas, the red pixel from area AM shows low reliability. **C)** V1 and HVAs ordered in approximate ascending hierarchical order, showing a clear decrease in reliability. All areas but area S1 (have significantly reliable visual responses to the natural movies (*:Bonferroni corrected $p < 0.006$, V1: $p = 4.9 \times 10^{-9}$, LM: $p = 1.1 \times 10^{-7}$, PM: $p = 2.5 \times 10^{-7}$, AL: $p = 9.1 \times 10^{-7}$, LI: $p = 4.4 \times 10^{-5}$, RL: $p = 9.3 \times 10^{-6}$, AM: $p = 7.5 \times 10^{-6}$, S1: $p = 0.079$; two-tailed single-sample t-test; n = 19 sessions over 7 mice). Error bars are median ± quartiles.

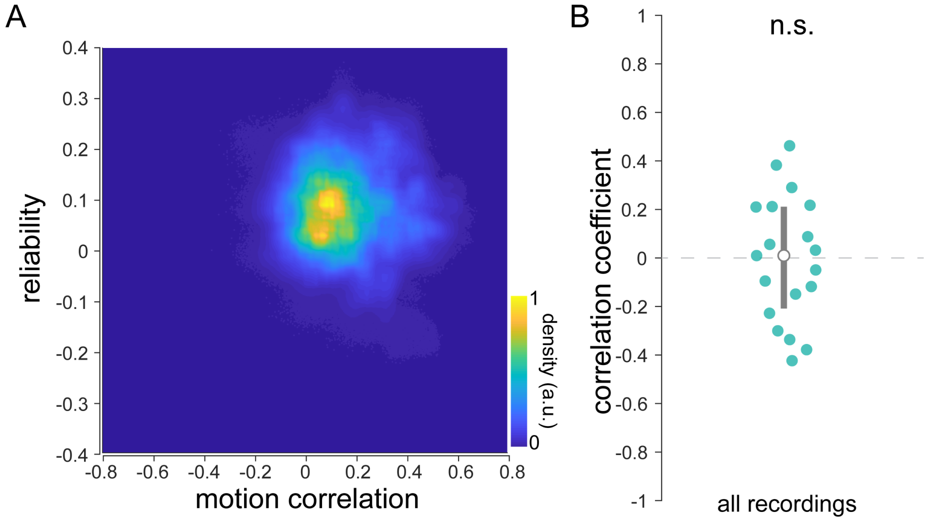

Figure 2.5: Correlation of reliability and motion response of natural movies **A)** Density plot of reliability versus motion correlation for all sessions. **B)** Correlation between reliability and motion correlation for each session (n = 19 sessions over 7 mice). There is no significant correlation between reliability and motion correlation across sessions $p = 0.91$; two-tailed single-sample t-test). Error bars are median ± quartiles.

The calcium response within a single pixel represents the summed activity across many neurons, so we could not measure tuning to preferred motion direction as is typically done in single neuron recordings. Instead, we took advantage of the fact that RDKs with higher coherence values will strongly drive neurons responsive to coherent motion and result in higher magnitude calcium responses regardless of motion direction. We used a small dot size (2° of visual space) and randomized dot position and drift direction on each trial, so that the only consistent visual feature across trials was the RDK motion coherence. We then defined the coherent motion correlation for each pixel as the Pearson correlation coefficient between the pixel response ($\Delta F/F$) and the RDK motion coherence (see Methods). We found that individual pixels in V1 and other HVAs exhibited a high degree of correlation with RDK coherence (Figure 2.7B). Aligning and averaging motion correlation maps revealed a anisotropic distribution of coherent motion correlated pixels within and across regions (Figure 2.7C). Despite the difference in stimulus, the motion

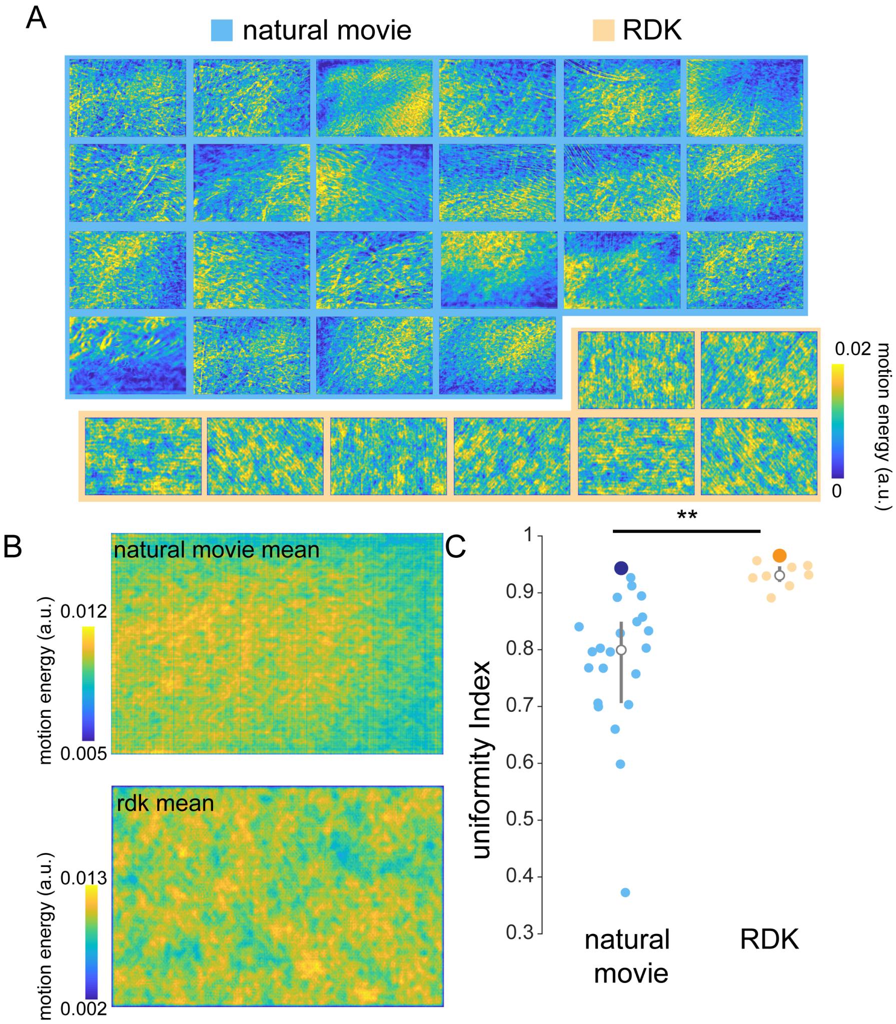

Figure 2.6: Natural movies have uneven motion energy across the frame. **A)** Mean motion energy across all frames for each of 22 different natural movies (blue background) and 8 RDKs of all shown directions (orange background). Whereas each natural movie has hotspots of motion energy, RDKs have motion energy present across the entire scene. When displayed across many directions, RDKs have an essentially flat distribution of motion energy across the frame. **B)** Mean motion energy across all stimuli for natural movies (top) and RDKs (bottom). In both cases, the combination of all stimuli results in a uniform distribution of motion energy across the frame. **C)** Comparison of uniformity index (see experimental procedures) across the frame for the motion energy of natural movies (n = 22 movies) and RDKs (n = 8 movies). RDKs have much higher motion energy uniformity across the frame $p = 0.004$, two-tailed unpaired two sample t-test). For each stimulus, the large dot (dark blue for natural movies, orange for RDKs) is the uniformity index of the single averaged motion energy from (B) (**: $p < 0.01$). Error bars are median ± quartiles.

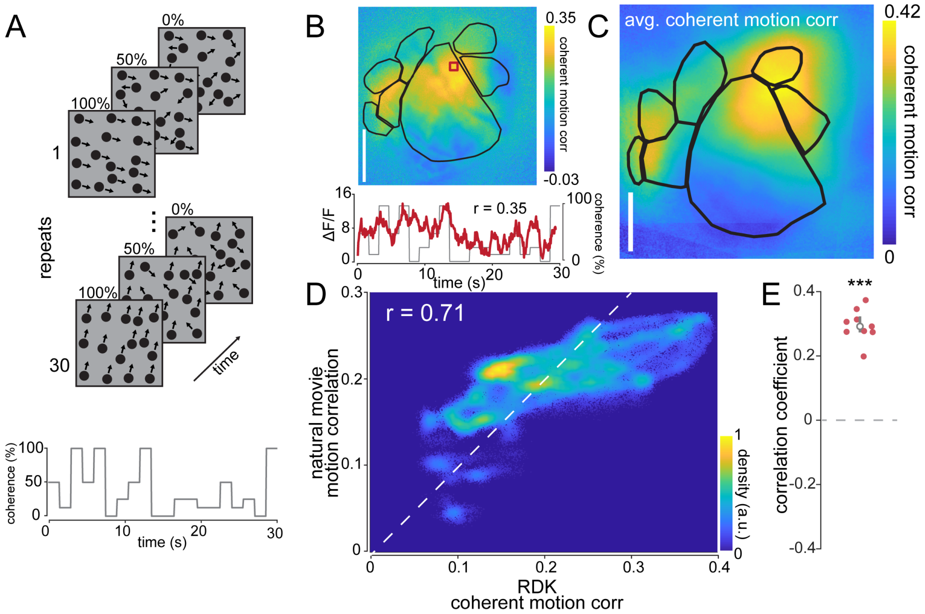

Figure 2.7: Mesoscale calcium responses to coherent motion in RDKs. **A)** Schematic of the RDK stimulus. A single repeat of the stimulus contains dots drifting at varying coherence values across the trial duration (bottom). Over multiple repeats, the coherence values remain constant while the dot positions and directions are randomized every trial. **B)** Top: map from a single experiment showing coherent motion correlation to RDKs across posterior cortex. Bottom: single pixel response (red) over the course of a single presentation of the stimulus overlaid on the coherence value trace; pixel-wise coherent motion correlation is calculated as the Pearson correlation between these two signals (r = 0.35). **C)** Mean coherent motion correlation map across all imaged mice (n = 10 sessions over 10 mice). Individual maps are transformed onto a common coordinate system for comparison across mice. **D)** Pixel-wise density plot of RDK vs. natural movie motion correlation across all mice to show similarity of motion correlation across visual stimuli (r = 0.71). Density plots are similar to scatter plots but provide additional information about the density (but not strength) at each coordinate, with warmer colors indicating a higher density of observation pairs (see Methods). **E)** Natural movie versus RDK motion correlation for each mouse (r = 0.30 ± 0.02, n = 10, $p = 1.0 \times 10^{-7}$; two-tailed single-sample t test).

correlation map measured with RDKs (Figure 2.7C) was well correlated to the motion correlation map measured with natural movies (Figure 2.3G), as indicated by the Pearson correlation of aligned pixels (Figure 2.7D, E; $r = 0.71$; $t_9 = 14.0$, $p = 1.0 \times 10^{-7}$, single-sample t test), although certain regions (e.g., RL) showed differences between stimuli (see Discussion).

2.4.2 HVAs exhibit differential responses to coherent visual motion

In primates, particular higher visual areas (MT/V5 and MST) are specialized for processing of coherent motion. To determine if particular mouse HVAs exhibit similarly dedicated motion processing, we examined coherent motion correlations in V1, each consistently defined HVA (LM, PM, AL, LI, RL, and AM), and somatosensory region S1 (as a negative control).

For each session, we defined visual areas using retinotopic mapping, and then measured coherent motion correlations for each pixel as the Pearson correlation between the deconvolved ΔF/F signal and the RDK motion coherence (Figure 2.8A, B). We then averaged all the pixels within each defined region of interest to generate a measure of coherent motion correlation by area. Using a Bonferroni-corrected p-value of 0.006 (p = 0.05, 8 tests), our statistical comparisons revealed that all visual regions except LM and LI exhibited coherent motion correlation values significantly above zero (Figure 2.8C, V1: 0.08 ± 0.02, $t_9 = 3.6$, $p = 3.0 \times 10^{-3}$; LM: 0.09 ± 0.03, $t_9 = 2.8$, $p = 9.7 \times 10^{-3}$; AL: 0.17 ± 0.03, $t_9 = 5.9$, $p = 1.1 \times 10^{-4}$; PM: 0.15 ± 0.03, $t_9 = 5.1$, $p = 3.0 \times 10^{-4}$; LI: 0.03 ± 0.02, $t_9 = 1.3$, p = 0.11; RL: 0.11 ± 0.02, $t_9 = 4.2$, $p = 1.1 \times 10^{-3}$; AM: 0.21 ± 0.03, $t_9 = 6.0$, $p = 1.0 \times 10^{-4}$; Bonferroni-corrected threshold $p < 0.006$, mean ± s.e.m., single-sample t test). As expected, area S1 was not motion responsive (0.003

± 0.01, $t_9 = 0.2$, p = 0.59; mean ± s.e.m., single-sample t test). Moreover, some HVAs had significantly higher coherent motion correlation than other visual regions (Figure 2.8D). Specifically, area AM had significantly higher motion response values than all other regions ($t_{68} = 3.3$, $p = 6.9 \times 10^{-4}$, Hedges' $g = 1.2$, unpaired two-sample t test), followed by AL, PM, RL, V1, and LM, while area LI had the lowest coherent motion correlation ($t_{68} = -3.2$, $p = 9.9 \times 10^{-4}$, Hedges' $g = 1.2$, unpaired two-sample t test, schematized in Figure 2.8E). These results indicate that particular HVAs in mice indeed exhibit enhanced responses to coherent motion relative to primary visual cortex. Given the differences in coherent motion correlations in HVAs, these results are broadly consistent with past anatomical and functional work suggesting that areas LM and LI constitute a homolog of the ventral stream, while areas AL, PM, RL, and AM constitute a homolog of the dorsal stream [41, 93, 42]. Indeed, each imaged dorsal stream area is significantly responsive to coherent motion, whereas ventral stream areas are more varied. In addition, dorsal areas show an elevated coherent motion correlation as compared with ventral stream areas as a whole (dorsal: 0.16 ± 0.04, ventral: 0.06 ± 0.06, $t_{68} = 3.9$, $p = 1.1 \times 10^{-4}$, Hedges' $g = 1.1$, mean ± s.e.m., unpaired two-sample t test).

2.4.3 Coherent motion correlations exhibit retinotopic asymmetry

In addition to differences in coherent motion correlations between visual areas, there was also anisotropy within individual visual areas. To quantify this, we first considered area V1, where pixels located in anterior V1 were more strongly driven by coherent motion than pixels in posterior V1 (Figure 2.9A, B). The anisotropy of coherent motion correlations in V1 could be explained in two ways: an anatomy-based organization (along anatomical axes) or a functional-based organization (along retinotopic axes). To test

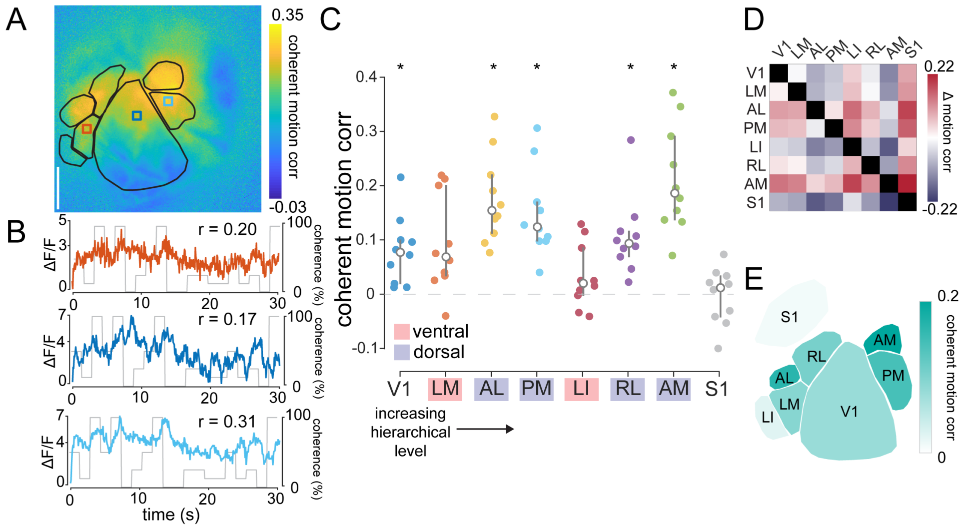

Figure 2.8: HVAs exhibit anisotropic coherent motion correlations to RDKs. **A)** Map from a single experiment highlighting anisotropic coherent motion correlations across HVAs. **B)** Single pixel responses taken from area LM (orange; top), V1 (dark blue; middle), and PM (light blue; bottom) overlaid on the coherence trace. Correlation between pixel response and coherent motion trace indicated for each pixel. **C)** Across all mice (n = 10 sessions over 10 mice), each tested dorsal stream visual area is significantly motion responsive, but neither ventral stream areas nor a control area outside of visual cortex (region S1) are motion responsive (*Bonferroni adjusted $p < 0.006$ ($p = 0.05$, 8 tests); two-tailed single-sample t test). Overlay indicates median ± quartiles. **D)** Relative difference matrix, with each element equal to the coherent motion correlation in the column region subtracted from the coherent motion correlation in the row region across mice (red, higher; blue, lower). **E)** Simplified schematic of mean coherent motion correlations in each cortical area across mice.

these possibilities, we isolated the entire visual cortex and calculated the z-scored coherent motion correlation for each pixel as a function of azimuth and elevation, as mapped with drifting bar stimuli (Figure 2.9C). Although there was little correlation across mice (n = 10 sessions over 10 mice) between the z-scored motion correlation and the azimuth, there was a strong negative correlation between the coherent motion correlation and the elevation, indicating stronger coherent motion processing in the lower visual field (Figure 2.9D-F; azimuth r = 0.09 ± 0.09, $t_9 = 0.4$, p = 0.34; elevation r = -0.54 ± 0.06, $t_9 = -7.5$, $p = 1.91 \times 10^{-5}$; single-sample t test).

To confirm that the anisotropy of coherent motion correlations in visual cortex is robust across measures, we also calculated coherent motion response curves for each pixel, fit a slope to each response curve, and plotted a map of the slopes (Figure 2.10A, B). This analysis resulted in qualitatively similar distribution of areal coherent motion responses (Figure 2.10C, D) and a negative correlation between coherent motion response and elevation (Figure 2.10E, F).

Because the stimulus monitor is flat, the edges of the display are farther from the mouse's eye than the center of the screen. Given that the dots in the RDK are of uniform size, the perceived size of the dots at the edges of the screen could be below the visual acuity of the mouse visual system. To confirm that our results are not due to this effect, we performed two additional control experiments.

First, we examined the retinotopy of RDK-driven activity independent of coherent motion (Figure 2.11). If the size of the dots near the edge of the screen were below the threshold of visual acuity, we would expect a radially decreasing magnitude from the center of V1 to the periphery. However, we do not observe this pattern (Figure 2.11A-C). All visual areas but RL show increased activity due to visual stimulus onset and area S1 shows a mild depression (Figure 2.11D, V1: 10.43 ± 0.75, $t_9 = 14.4$, $p = 8.1 \times 10^{-8}$; LM: 2.78 ± 0.30, $t_9 = 9.5$, $p = 2.7 \times 10^{-6}$; AL: 2.03 ± 0.43, $t_9 = 4.7$, $p = 5.4 \times 10^{-4}$;

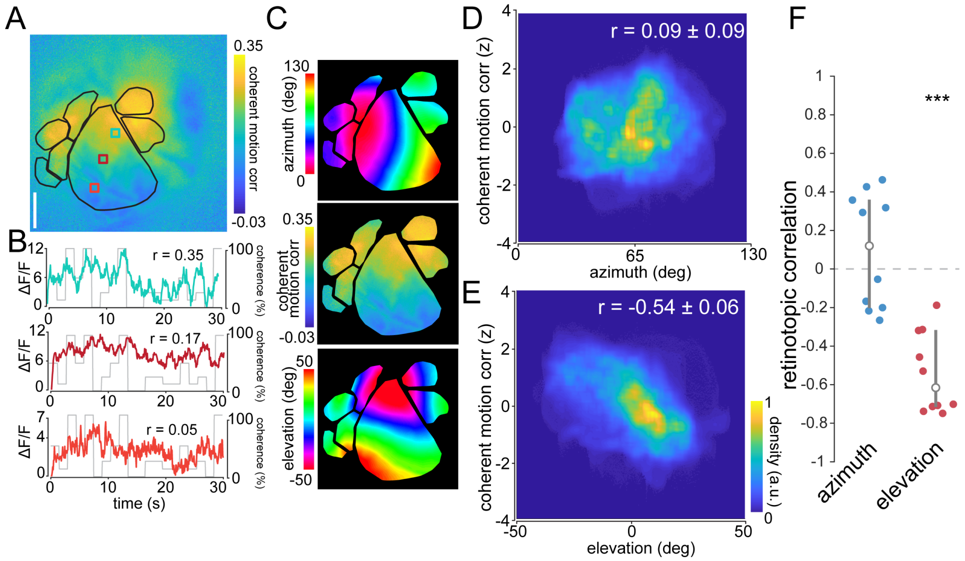

Figure 2.9: Retinotopic asymmetry of coherent motion correlations across the visual cortex. **A)** Map from single experiment showing gradient of coherent motion correlation along the vertical retinotopic axis of V1. **B)** Single pixel responses from anterior (blue, r = 0.35), middle (red, r = 0.17), and posterior (orange, r = 0.05) pixels in V1, showing different amounts of coherent motion correlation. **C)** Visual cortex isolated maps from mouse in (A) of azimuth (top) and elevation (bottom), as well as the coherent motion correlation (middle) for comparison. **D)** Density scatter plot across all mice (n = 10 sessions over 10 mice), showing no significant correlation to azimuth (r = 0.09 ± 0.09). Coherent motion correlation is z-scored to account for differences between experiments. **E)** Same as (D), but for elevation, showing a significant negative correlation between elevation preference and coherent motion correlation across visual cortex (r = -0.54 ± 0.06, $p = 1.9 \times 10^{-5}$, two-tailed single-sample t test). **F)** Comparison of retinotopic correlation between azimuth and elevation. There is a significant anticorrelation of coherent motion correlation and elevation across mice, but none with azimuth ($p = 1.9 \times 10^{-5}$, two-tailed single-sample t test. Error bars are median ± quartiles (***$p < 0.001$).

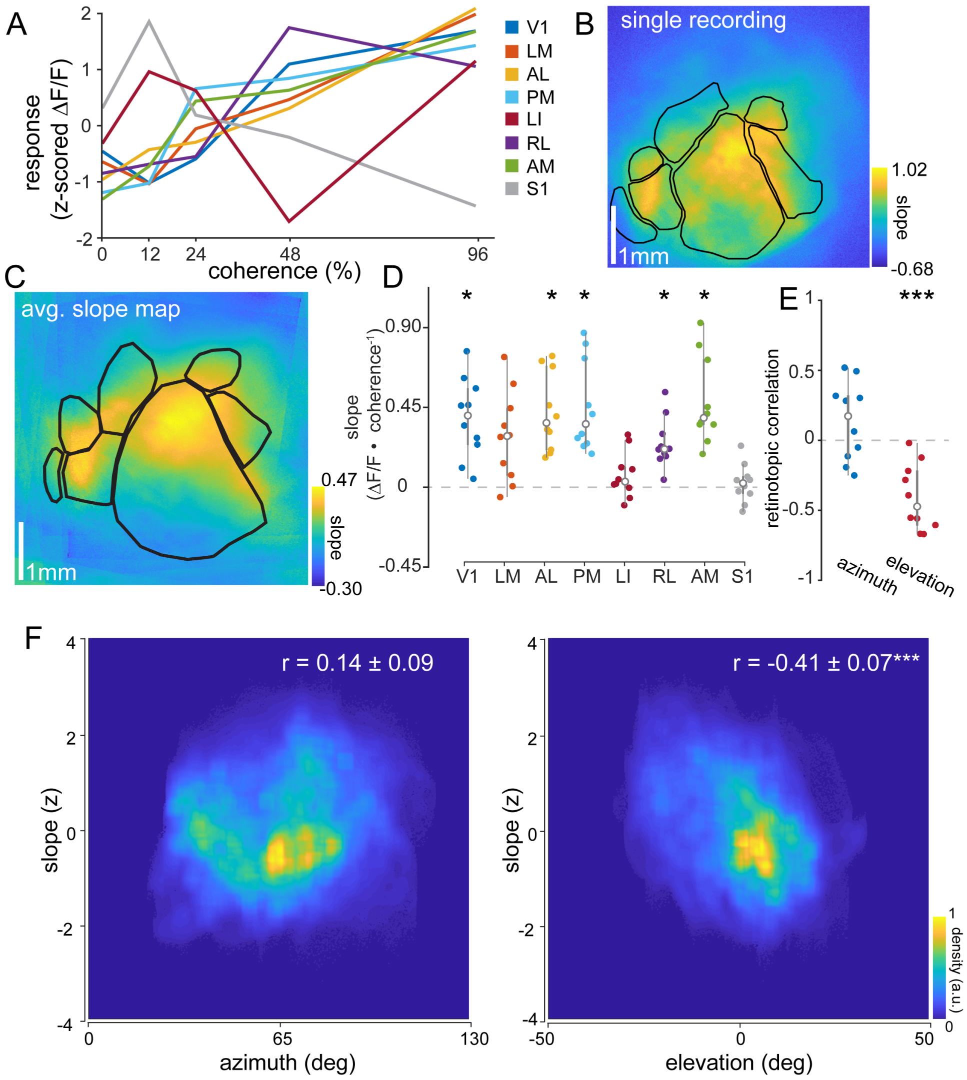

Figure 2.10: Coherent motion response curves measured with mesoscale calcium imaging. **A)** Example of neural responses to coherent motion present in the RDK. **B)** Map of coherent motion response slopes for a single recording. **C)** Average slope map across all imaged mice (n = 10 sessions over 10 mice). **D)** Across mice (n = 10 sessions over 10 mice), dorsal stream areas are significantly responsive to coherent motion, but ventral stream areas and nonvisual areas are not (V1: $p = 4.2 \times 10^{-4}$, LM: $p = 6.4 \times 10^{-3}$, AL: $p = 1.9 \times 10^{-4}$, PM: $p = 3.4 \times 10^{-4}$, LI: $p = 1.2 \times 10^{-1}$, RL: $p = 3.3 \times 10^{-4}$, AM: $p = 1.5 \times 10^{-4}$, S1: $p = 9.6 \times 10^{-1}$, two-tailed single sample t-test) *: Bonferroni corrected $p < 0.006$. Error bars are median ± quartiles. **E)** Comparison of retinotopic correlation between azimuth $p = 0.16$, two-tailed single sample t-test) and elevation ($p = 3.9 \times 10^{-4}$, two-tailed single sample t-test) for slope (n = 10 sessions over 10 mice). Error bars are median ± quartiles (***: $p < 0.001$). **F)** Density scatter plot across all mice showing no correlation for azimuth $p = 0.16$; two-tailed single-sample t-test), but a significant negative correlation for elevation ($p = 3.9 \times 10^{-4}$; two-tailed single-sample t-test).

PM: 4.59 ± 0.49, $t_9 = 5.3$, $p = 2.4 \times 10^{-4}$; LI: 1.48 ± 0.28, $t_9 = 5.5$, $p = 2.0 \times 10^{-4}$; RL: 0.30 ± 0.23, $t_9 = 1.0$, $p = 0.18$; AM: 1.29 ± 0.21, $t_9 = 6.1$, $p = 8.6 \times 10^{-5}$; S1: -0.57 ± 0.16, $t_9 = -3.5$, $p = 3.3 \times 10^{-3}$; mean ± s.e.m., single-sample t test). We also observed a weak positive correlation between visually driven activity and both azimuth and elevation (Figure 2.11E, F). However, this pattern is incongruent with the pattern described for coherent motion correlation (Figure 2.9A).

To further confirm that the retinotopic anisotropy was not due to variable screen distance, in a subset of mice we applied spherical correction to the RDKs (Figure 2.12A), resulting in uniform perceived dot size across the stimulus display. The resulting coherent motion correlation maps are nearly identical to those using the uncorrected RDKs (Figure 2.12B, C). Furthermore, the correlation between coherent motion correlation and elevation remains strongly negative, while remaining uncorrelated for azimuth (Figure 2.12D, E).

We next investigated whether the retinotopic asymmetry was also present in other HVAs. For each area, we calculated the correlation between the z-scored coherent motion correlation and azimuth (Figure 2.14a–h, left plots) and elevation (Figure 2.14a–h, right plots). No visual areas exhibited significant correlation between the preferred azimuth and the coherent motion correlation, although areas LM and LI trended toward a significant positive correlation (Figure 2.14i; V1: 0.09 ± 0.12, $t_9 = 0.2$, $p = 0.44$; LM: 0.46 ± 0.13, $t_9 = 3.0$, $p = 7.0 \times 10^{-3}$; AL: -0.10 ± 0.14, $t_9 = -0.1$, $p = 0.46$; PM: -0.12 ± 0.13, $t_9 = -0.3$, $p = 0.38$; LI: 0.35 ± 0.10, $t_9 = 3.0$, $p = 8.0 \times 10^{-3}$; RL: -0.06 ± 0.20, $t_9 = -0.7$, $p = 0.76$; AM: -0.09 ± 0.12, $t_9 = -0.1$, $p = 0.46$; S1: 0.13 ± 0.13, $t_9 = 0.5$, $p = 0.33$; Bonferroni-corrected threshold $p < 0.006$, mean ± s.e.m., single-sample t test). Conversely, several regions (areas V1, PM, and LM) exhibited a significant negative correlation between the preferred elevation and the coherent motion correlation. In addition, areas AM and RL were trending toward significance, but ar-

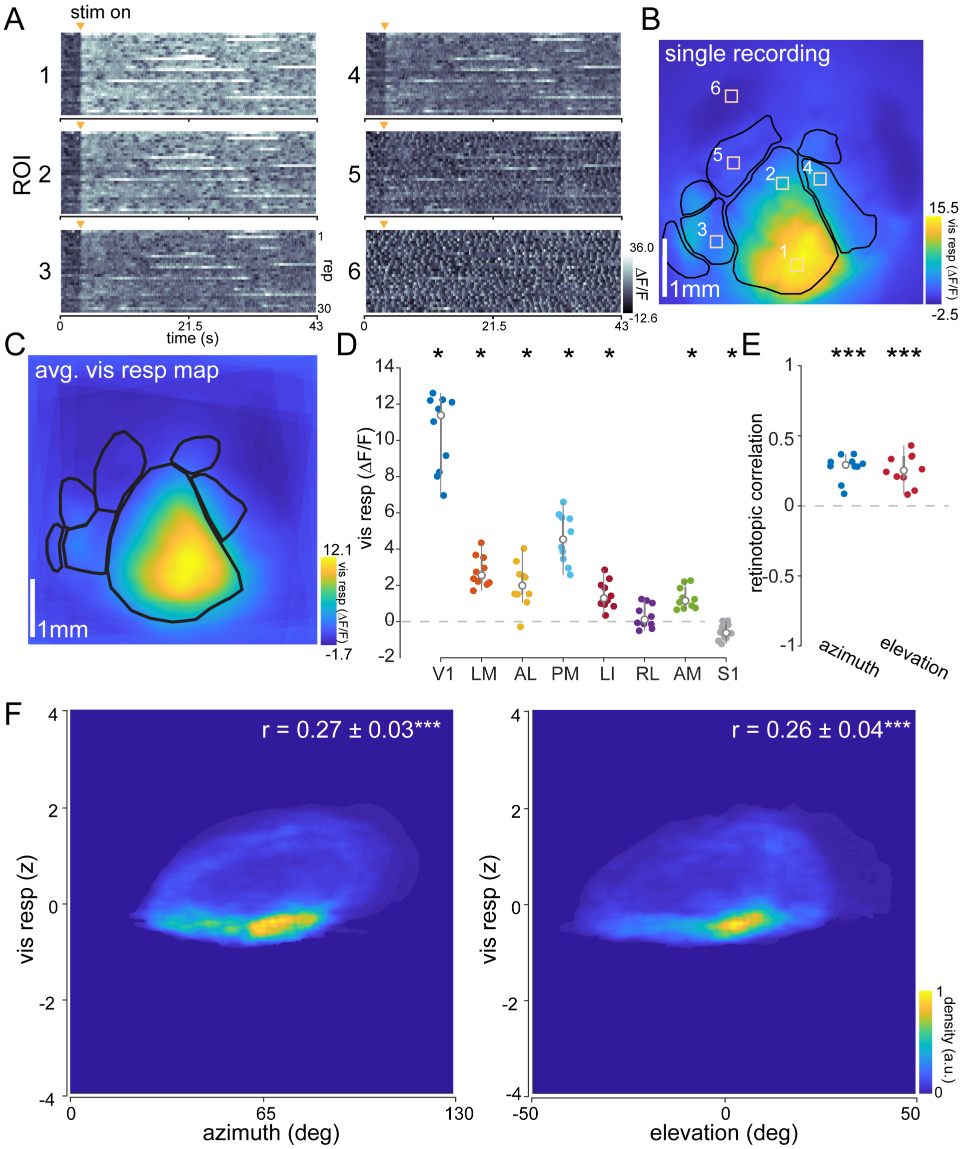

Figure 2.11: Magnitude of visual response to RDK stimulus across posterior cortex **A)** Six example pixels (identified in B) showing responses across posterior cortex. **B)** Map of visual responsiveness from a single mouse. **C)** Average visual responsiveness map across all imaged mice. **D)** Across all mice, most visual areas are strongly driven by visual stimuli, whereas S1 shows a mild suppression to visual stimuli (V1: $p = 8.1 \times 10^{-8}$, LM: $p = 2.7 \times 10^{-6}$, AL: $p = 5.4 \times 10^{-4}$, PM: $p = 2.4 \times 10^{-6}$, LI: $p = 2.0 \times 10^{-4}$, RL: $p = 1.8 \times 10^{-1}$, AM: $p = 8.6 \times 10^{-5}$, S1: $p = 3.3 \times 10^{-3}$, two-tailed single sample t-test). (*: Bonferroni corrected $p < 0.006$). **E)** Comparison of retinotopic correlation between azimuth ($p = 5.2 \times 10^{-6}$, two-tailed single sample t-test) and elevation ($p = 4.7 \times 10^{-5}$, two-tailed single sample t-test) for visual responsiveness. (***: $p < 0.001$). **F)** Density scatter plot across all mice showing positive correlations for both azimuth ($p = 5.2 \times 10^{-6}$; two-tailed single-sample t-test) and elevation ($p = 4.7 \times 10^{-5}$; two-tailed single sample t-test).

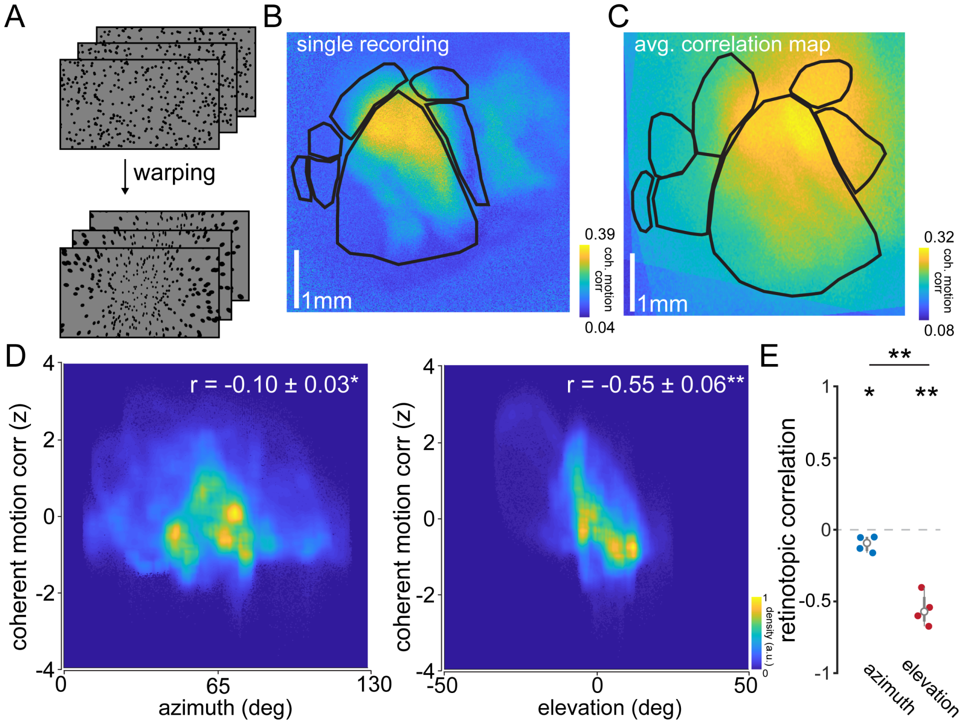

Figure 2.12: Mesoscale calcium responses to coherent motion using spherically corrected RDKs **A)** Schematic of the spherical correction procedure. The same procedure applied to retinotopic mapping stimuli was applied to the RDKs to create warped RDK stimuli. **B)** Map of coherent motion correlation from a single mouse. **C)** Average motion correlation map across all imaged mice (n = 4 sessions over 4 mice). Individual maps are transformed onto a common coordinate system for comparison across mice. **D)** Density scatter plot across all mice showing significant correlations for both azimuth (left r = -0.10 ± 0.03, $p = 0.03$; two-tailed single-sample t-test) and elevation (right r = -0.55 ± 0.06, $p = 0.002$; two-tailed single-sample t-test). However, the retinotopic correlation to elevation is significantly more negative than that for azimuth $p = 0.008$, two-tailed paired t-test). **E)** Comparison of retinotopic correlation (n = 4 sessions over 4 mice) between azimuth $p = 0.03$, two-tailed single sample t-test) and elevation $p = 0.002$, two-tailed single sample t-test). Elevation correlation is significantly more negative than azimuth correlation $p = 0.008$, two-tailed unpaired two sample t-test). Error bars are median ± quartiles (*: $p < 0.05$, **: $p < 0.01$).

eas AL, LI, and S1 did not show significant retinotopic anisotropy in coherent motion correlation (Figure 2.14j; V1: -0.81 ± 0.05, t_9 = 5.3, -10.3, $p = 1.4 \times 10^{-6}$; LM: -0.44 ± 0.08, $t_9 = -3.3$, $p = 4.3 \times 10^{-3}$; AL: 0.03 ± 0.14, $t_9 = -1.1$, $p = 0.85$; PM: -0.78 ± 0.06, $t_9 = -8.9$, $p = 4.5 \times 10^{-6}$; LI: -0.04 ± 0.11, $t_9 = -0.6$, $p = 0.73$; RL: -0.27 ± 0.10, $t_9 = -2.1$, $p = 0.035$; AM: -0.36 ± 0.14, $t_9 = -2.0$, $p = 0.036$; S1: -0.14 ± 0.09, $t_9 = -1.3$, $p = 0.11$; Bonferroni-corrected threshold $p < 0.006$, mean ± s.e.m., single-sample t test). This pattern of coherent motion correlation may be explained by the visual hierarchy, with lower visual areas (V1, PM, and LM) showing strong motion coherence correlation, but higher areas (AM, RL) showing weaker motion correlation. Note that the negative correlation between the preferred elevation and motion response could not be explained by a decreasing anterior-to-posterior anatomical gradient, as several HVAs (e.g., area PM) have vertical retinotopic gradients that are not co-oriented to the anatomical gradient. Furthermore, the negative correlations tended to be strongest in regions in which the pixels subtended a larger range of elevation (Figure 2.13), as measured by the elevation covered by 95% of the pixels (E95%), such as V1 (E95% = 58.42°) and PM (E95% = 32.16°), compared with areas AM (E95% = 25.25°) and AL (E95% = 20.85°). There was no relationship between azimuth correlations and azimuth coverage (A95%; Figure 2.13C). Although the retinotopic coverage of the HVAs is similar to that reported with intrinsic signal imaging in previous work [90], it is possible that the population averaging and low-pass filtering inherent to wide-field population imaging approaches may underestimate the retinotopic extent of the individual neurons within each region.

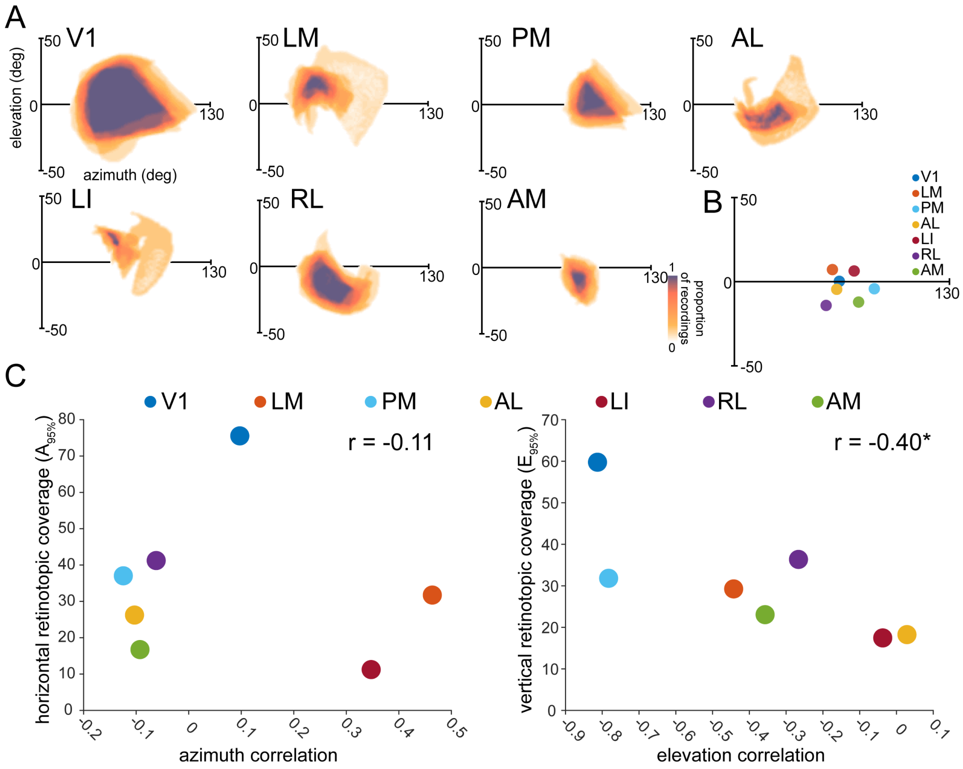

Figure 2.13: Relationship between retinotopic correlation and visual coverage **A)** Visual field coverage of each identified visual area. The center of the axes is the center of V1, denoting (0, 0) in a monocular retinotopic space. **B)** Centers of each identified area, showing the varying biases of each visual area to different parts of the visual field. **C)** Comparison between the retinotopic correlation and retinotopic coverage (A95%) in its respective axis for azimuth (left) and altitude (right). Azimuth correlation does not depend on the visual span of each area in the azimuth; whereas, the altitude correlation decreases strongly with decreasing vertical span (azimuth: $p = 0.81$, altitude: $p = 6.7 \times 10^{-4}$; n = 10 sessions over mice, two-tailed single-sample t-test).

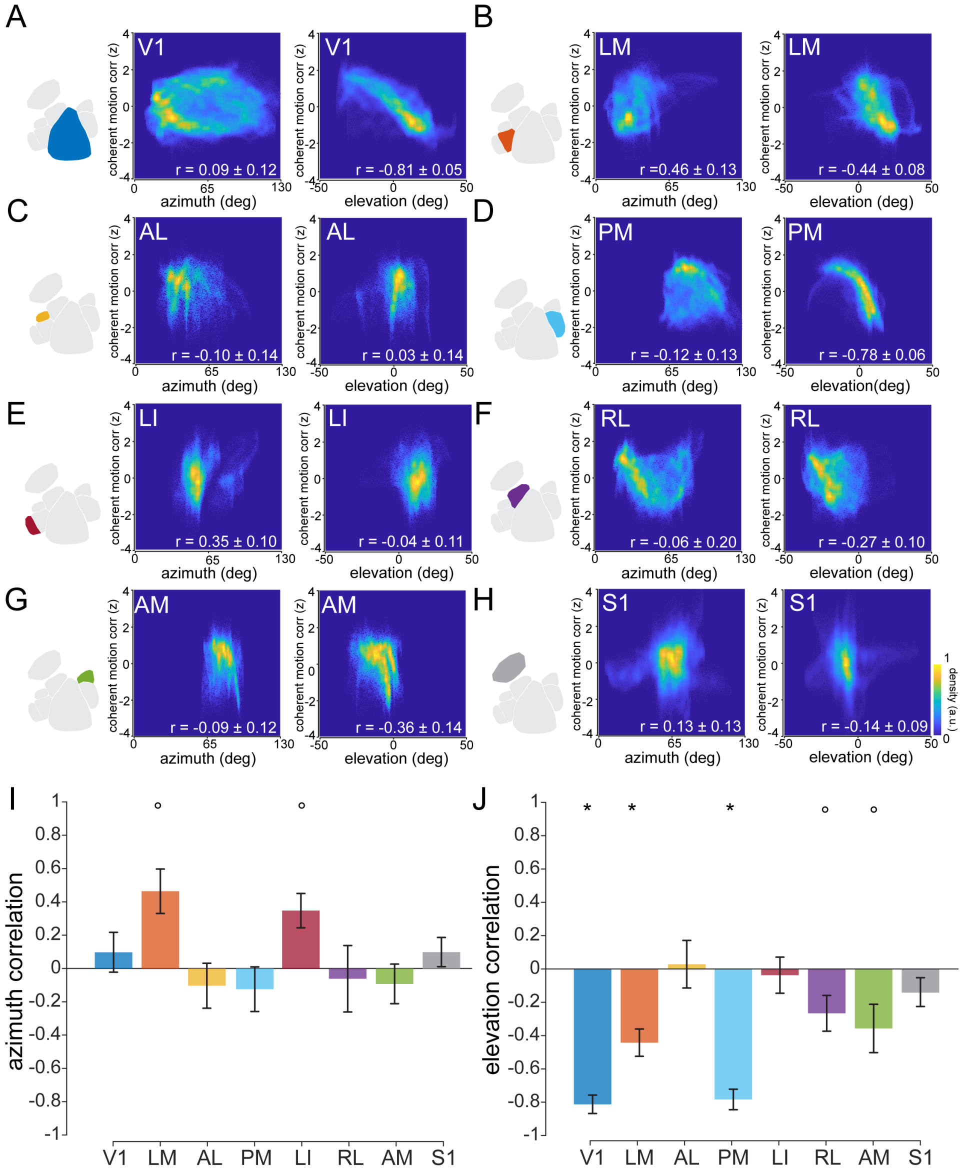

Figure 2.14: Retinotopic dependence of coherent motion correlation in each visual area. **A)** Left: combined density scatter plot across all mice (n = 10 sessions over 10 mice) comparing z-scored coherent motion correlation to azimuth for area V1. Right: same as left, but for elevation. **B) - H)** Same as (A) for each HVA (LM, AL, PM, LI, RL, AM), and somatosensory cortex (S1). **I)** Mean Pearson's correlation coefficient between azimuth and coherent motion correlation for each area (V1: $p = 0.44$; LM: $p = 7.0 \times 10^{-3}$; AL $p = 0.46$; PM: $p = 0.38$; LI: $p = 8.0 \times 10^{-3}$; RL: $p = 0.76$; AM: $p = 0.46$; S1: $p = 0.33$; two-tailed single-sample t test). **J)** Same as (I), but for elevation. (V1: $p = 1.4 \times 10^{-6}$; LM: $p = 4.3 \times 10^{-3}$; AL: $p = 0.85$; PM: $p = 4.5 \times 10^{-6}$; LI: $p = 0.73$; RL: $p = 0.035$; AM: $p = 0.036$; S1: $p = 0.1$; two-tailed single-sample t test). $^{\circ}p < 0.05$; *Bonferroni adjusted $p < 0.006$, $p = 0.05$, 8 tests). Error bars are median ± quartiles.

2.4.4 Coherent motion correlations of single neurons

Although wide-field imaging revealed differences in coherent motion correlations both across and within visual regions, we wanted to confirm that individual neurons exhibited the same response distributions. To this end, we used two-photon calcium imaging to measure the activity of populations of Layer 2/3 excitatory neurons in regions V1 and a subset of HVAs (LM, PM, and AM) that exhibited varying levels of coherent motion correlation (Figure 2.15A, B). To determine whether individual neurons exhibit coherent motion correlations, we displayed RDKs in eight directions at a range of coherence values (0–100%), then measured the correlation coefficient between the average calcium response and the coherence trace for each direction (Figure 2.15C). We found that individual neurons showed significant coherent motion selectivity in V1 (74% of 11,018 cells, n = 27 sessions over 15 mice) and all imaged HVAs, including LM (83% of 2166 cells, n = 8 sessions over 8 mice), PM (84% of 1781 cells, n = 8 sessions over 8 mice), and AM (82% of 1178 cells, n = 7 sessions over 7 mice). As expected, individual neurons exhibited selectivity for particular coherent motion directions [57] (Figure 2.15B, C). As such, across all visual areas, population responses to direction were highly mixed, though there was a slight bias toward the horizontal directions (nasal and temporal; Figure 2.15D, E) that was consistent across imaging fields and mice (Figure 2.15F; p = 1.76 × 10-6, n = 3461 cells, Hodges–Ajne test for circular non-uniformity). Although the mean coherent motion correlation for the preferred direction was significant for all visual areas imaged (Figure 2.15G; V1: 0.26 ± 0.02, $t_{26} > 20$, $p = 1.6 \times 10^{-17}$; LM: 0.31 ± 0.01, $t_7 = 9.7$, $p = 1.3 \times 10^{-5}$; PM: 0.37 ± 0.01, $t_7 = 11.8$, $p = 3.6 \times 10^{-6}$; AM: 0.36 ± 0.01, $t_6 = 15.6$, $p = 2.2 \times 10^{-6}$; Bonferroni-corrected threshold, $p < 0.006$, mean ± s.e.m., single-sample t test), it was significantly higher in areas PM ($t_{33} = 2.3$, $p = 1.3 \times 10^{-2}$, Hedges' $g = 1.2$, unpaired two-sample t test) and AM ($t_{32} = 3.2$, $p = 1.7 \times 10^{-3}$, Hedges'

$g = 1.0$, unpaired two-sample t test) as compared with V1, similar to results from wide-field imaging (Figure 2.8).

2.4.5 Single neuron asymmetry in coherent motion correlation

Finally, we wanted to confirm that the lower field bias of coherent motion processing evident in the wide-field imaging experiments is also present at the level of individual neurons. To test this, we first measured the preferred azimuth and elevation of populations of V1 neurons using flashing bars with a flickering checkerboard pattern randomly presented at a range of locations (Figure 2.16A; see Methods). We then measured the coherent motion correlation in the preferred direction for each neuron (Figure 2.16B, C) and correlated the coherent motion correlation with the preferred azimuth and elevation. Similar to the wide-field imaging results (Figure 2.9), neurons preferring lower elevation exhibited greater coherent motion correlations than neurons preferring higher elevation (Figure 2.16D, E), although the individual neurons exhibited greater variance (Figure 2.16D) and the linear fits had a shallower slope than with wide-field imaging (two-photon: -0.63% deg^{-1}, wide field: -1.04% deg^{-1}). No correlation was present between coherent motion correlation and azimuth (Figure 2.17). Taken together, the individual neurons largely reflect both the areal differences and retinotopic asymmetry observed wide-field imaging, while also revealing a bias toward horizontal coherent motion that was not evident with mesoscale imaging.

2.5 Discussion

In this paper, we report three key findings: (1) all visual areas measured, including V1, exhibit reliable responses to global coherent motion independent of the spatial content of the retinal image, (2) HVAs respond heterogeneously to coherent visual motion, with

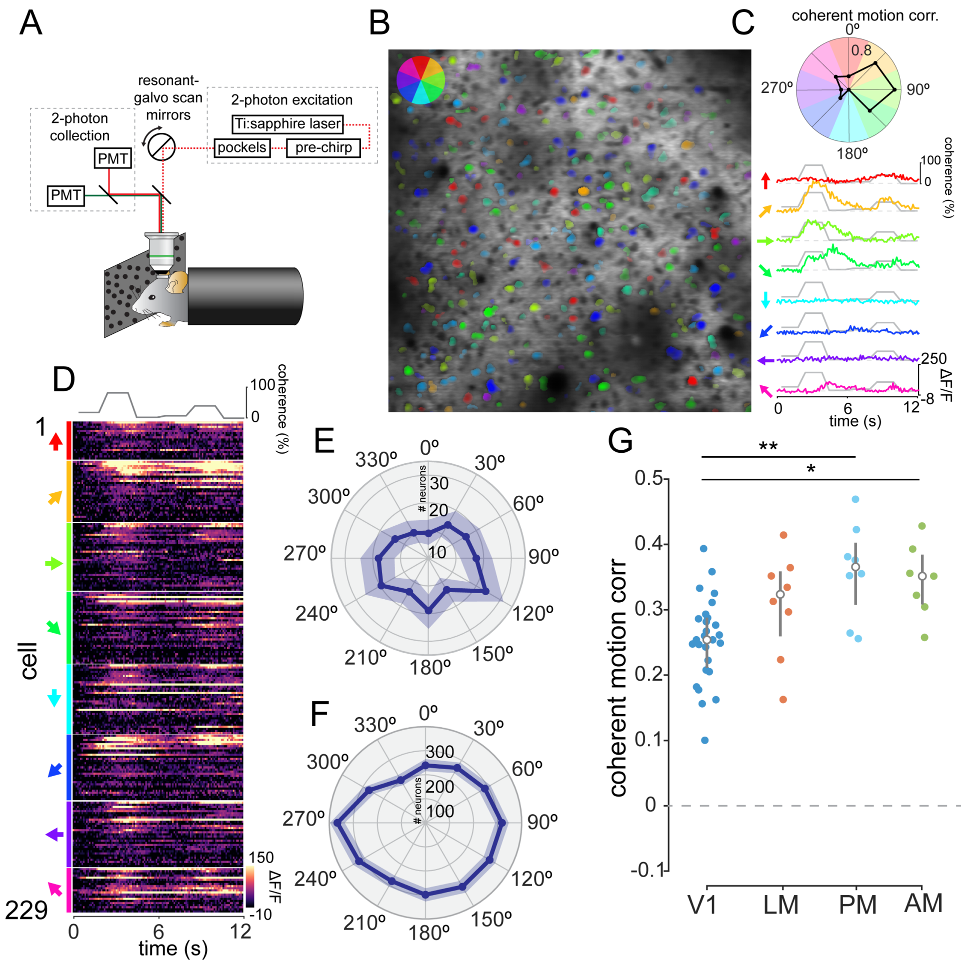

Figure 2.15: Coherent motion responses of single cells. **A)** Schematic of the two-photon microscopy experimental setup. **B)** Example two-photon imaging field from V1. Scale bar is 100 μm. **C)** Top: polar plot of coherent motion correlation for each motion direction. Bottom: responses of a single example neuron to each of the eight motion directions. **D)** Responses of each cell in the example session. **E)** Polar plot of averaged directional tuning to coherent motion across all cells in the example session. **F)** Histogram of 30° binned preferred direction of all neurons across all sessions. (n = 3461 cells from 13 mice, $p = 1.73 \times 10^{-6}$, Hodges–Ajne test for non-uniformity). **G)** Mean coherent motion correlation across HVAs. Each point represents the mean coherent motion correlation of all the cells in that session. Although all areas exhibit significant coherent motion correlations (V1: $p = 1.6 \times 10^{-17}$; LM: $p = 1.3 \times 10^{-5}$; PM: $p = 3.6 \times 10^{-6}$; AM: $p = 2.2 \times 10^{-6}$), areas AM and PM have significantly higher coherent motion correlations than area V1 (PM: $p = 1.3 \times 10^{-2}$; AM: $p = 1.7 \times 10^{-3}$; two-tailed unpaired two-sample t test). $^*p < 0.05$; $^{**}p < 0.01$, two-sample t test.

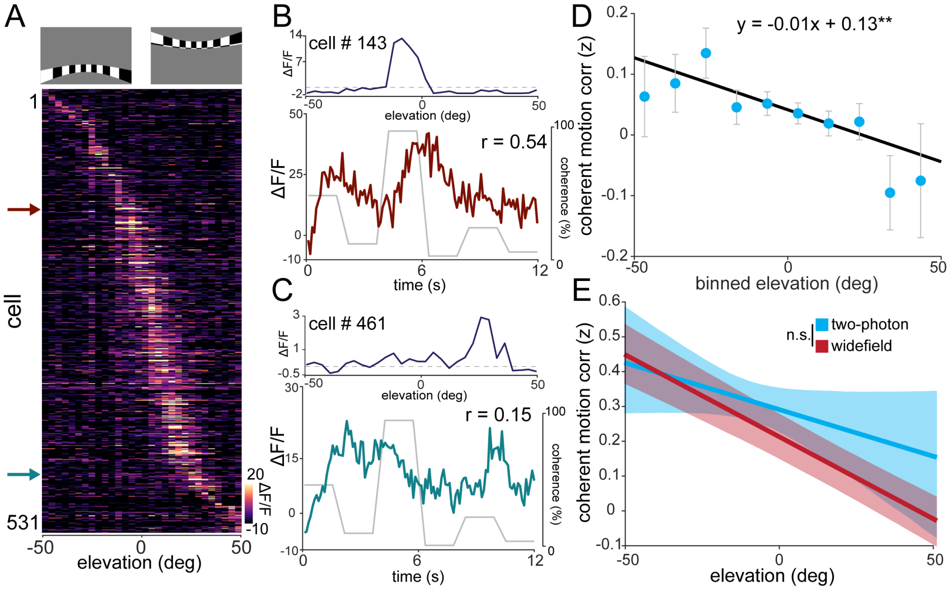

Figure 2.16: Retinotopic asymmetry of single-cell coherent motion correlations in V1. **A)** Top: examples of a high elevation and low elevation spherically corrected retinotopic bar stimulus. Bottom: averaged responses of each cell in the field to the elevation retinotopic bar stimulus, ordered by elevation preference. **B) and C)** Top: the preferred elevation location of the specified cell. Bottom: the calcium response of the cell during the RDK stimulus, with the coherence trace overlaid. **D)** Plot of elevation preference versus z-scored coherent motion correlation with neurons averaged within 10° elevation bins (n = 2680 cells from 13 mice). Error bars are mean ± s.e.m. **E)** Plot of mean elevation preference versus coherent motion correlation averaged across experiments for wide-field (red) and two-photon experiments (blue). The confidence band represents the bootstrapped 95% confidence intervals of the slope and intercept (wide field vs. two-photon$p = 0.51$, two-tailed unpaired two-sample t test). $*p < 0.01$.

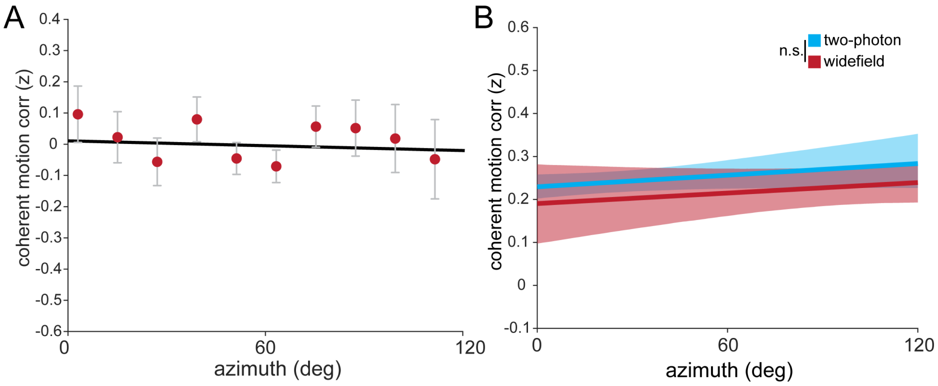

Figure 2.17: Coherent motion responsiveness across azimuth in V1 **A)** Plot of azimuth preference versus z-scored coherent motion correlation, averaged in 10° azimuth bins (n = 2680 cells from 13 mice). Error bars are mean ± s.e.m. **B)** Plot of mean azimuth preference versus coherent motion correlation averaged across experiments for widefield (red) and two-photon (blue) experiments, as in Figure 2.16E. Confidence band represents bootstrapped 95% confidence intervals of slope and intercept. The slopes between widefield and two-photon fit lines are not significantly different $p = 0.95$, two-tailed single-sample t-test).

stronger responses in putative dorsal stream areas, and (3) neurons which represent the lower visual field having significantly stronger responses to coherent visual motion across visual areas. These findings have implications both for our understanding of murine visual motion processing and for more generalized principles of cortical organization.

In highly visual mammals, researchers have found defined extrastriate regions that are specialized for processing of coherent visual motion, including posteromedial (PMLS) and posterolateral (PLLS) lateral suprasylvian cortex in cats [101, 102], MT and MST cortex in non-human primates [29, 64, 65, 66], and V5 in humans [103]. Anatomical [90, 41, 93] and functional [74, 42] evidence has suggested that mouse visual cortex might also have dedicated areas specialized for processing of coherent motion, but previous studies had not tested this possibility systematically.

In this paper, we used wide-field calcium imaging to systematically investigate the activity of seven visual areas (V1, LM, AL, PM, LI, RL, and AM) in response to coherent motion stimuli. We found that all visual regions exhibited reliable responses to coherent motion, but that areas AM, AL, and PM exhibited stronger correlations to coherent motion than RL, V1, LM, and LI (Figure 2.8). These findings held true at the single-cell level, as shown with two-photon calcium imaging of selected populations (Figure 2.15). This is mostly consistent with prior categorization of these regions into putative dorsal (AL, PM, RL, AM) and ventral (LM, LI) streams [90, 41, 93, 42]. One exception is area RL, which is generally considered a dorsal stream area, but in our study had moderate responses to coherent visual motion (in between ventral and dorsal stream areas) using RDKs, though not natural movies. A recent paper suggests that region RL might be preferentially involved in processing binocular disparity, with inferior responsive neurons particularly attuned to the near field visual stimuli rather than visual motion [104]. Another possibility is that the stimulus parameters used for the RDKs are not well-suited to driving RL neurons, but that coherent motion found in natural movies is more effective.

Although we do not currently know how downstream cortical regions use signals from visual HVAs in local computations, the cortico-cortical connectivity of the motion-responsive regions suggests an intriguing possibility. The HVAs with strong coherent motion correlations (PM, AL, and AM) are highly interconnected with regions involved in navigation, including the parietal cortex, retrosplenial cortex, anterior cingulate cortex, and the presubiculum [93]. Indeed, area AM is often considered a posterior parietal region [41] though there is not yet widespread agreement on the boundaries between HVAs and parietal cortices [105]. This connectivity profile suggests that neurons in these HVAs may play an important role in visually guided navigation, providing external motion cues to higher cortical regions.

Although we found that mice are similar to cats and primates in having specialized HVAs dedicated to coherent motion processing, we also found a new principal of organization within visual areas that had not been described in previous studies. Specifically, we found that motion processing in mouse visual cortex is asymmetric across elevation, with neurons representing the lower field exhibiting significantly stronger coherent motion correlations both across visual cortex and within defined visual areas (Figure 2.14 and 2.16). We also observed a trend toward a positive correlation in ventral stream areas (LM and LI) between azimuth and coherent motion responsiveness (Figure 2.14). However, the positive correlation was not statistically significant, and was not observed in V1 (Figure 2.14; Figure 2.17) or across the visual cortex as a whole (Figure 2.9). This is in contrast to the negative correlation between coherent motion correlation and elevation, which was robust across the visual cortex (Figure 2.9). The lower field bias is somewhat surprising since it is known that overhead radial motion (such as looming stimuli) can cause strong behavioral reactions such as freezing and escape responses [106]. Indeed, there may even be specialized RGCs for local motion in the superior visual field [79]. This may be due to specialized RGCs responding to different types of motion (radial versus linear). Alternatively, recent studies indicate that behavioral responses to overhead radial motion appear to be principally mediated by a direct circuit from retina to superior colliculus to brain stem nuclei [107, 108]. This raises the possibility that motion-responsive RGCs may project to separate thalamic or collicular targets depending on their retinotopy.

It has previously been found that V1 projections to different HVAs exhibit visual response properties consistent with the target area [109]. One way the dorsal stream areas (AL, PM, RL, AM) could inherit both a lower bias in visual field coverage [90] and strong responses to coherent motion relative to other HVAs would be if they received preferential innervation from anterior V1; with ventral stream areas (LM, LI) receiving preferential input from posterior V1.

An open question is whether there is a functional reason for the lower field bias in coherent motion correlations. One possibility is that coherent motion-responsive units convey external motion cues to downstream regions, which would be consistent with known cortico-cortical connectivity [93]. Since mice have coarse spatial resolution (10° receptive field size [40]) and their eye level is close to the ground, cues for external motion are likely more prevalent in the lower visual field. That the horizontal bias in preferred direction observed in single neurons (Figure 2.15D-F) also reflects a bias in the lower field external motion cues reaching the visual system is consistent with this interpretation.

These results also raise the question of whether the lower field bias of coherent motion correlations might also exist in other visual mammals such as primates. Since primates have higher acuity and their eye level is farther from the ground, it is possible that external motion cues are more distributed across the visual field than for mice, obviating the need for asymmetric processing of motion cues across retinotopic space. However, behavioral evidence of an "lower field advantage" in detecting motion suggests that there may indeed be some lower field bias present even in humans [110, 111], though this has not been confirmed at the cellular level.

It should be noted that although coherent motion correlations were stronger in particular HVAs and in retinotopic regions corresponding to the lower visual field at the population level, there was substantial heterogeneity at the level of individual neurons (Figures 2.15 and 2.16), and that coherent motion-responsive neurons could be found throughout the retinotopic gradient and visual areas.

One of the most surprising findings of the current study is that there is as much variability in coherent motion correlations within a visual area as across visual areas. Several recent studies have found similar mesoscale organization in other response properties in mouse visual cortex. For example, recent studies have found retinotopic asymmetry of color selectivity within area V1 [112] and binocular disparity preference within area RL [104]. Moreover, researchers also found that neurons in higher visual and parietal regions exhibit anatomical gradients of task-modulated responses during navigation in a virtual environment, and that these gradients cross retinotopic borders [113]. Together with our results, this suggests that visual input is not processed uniformly in each area as it progresses through the cortical hierarchy, but rather that there is considerable parallel processing along retinotopic axes within defined areas. Since topographic organization is present in many cortical areas, further research is necessary to determine whether this principle is present in other species and in other sensory, and non-sensory, cortices. These results suggest a general principle of sensory coding, which takes advantage of topographic mapping to selectively route visual information within areas throughout the cortical hierarchy, increasing the bandwidth for ethologically relevant stimuli across cortex.

Chapter 3

Coregistration of heading to visual cues in retrosplenial cortex

3.1 Preface

Spatial cognition depends on an accurate representation of orientation within an environment. Head direction cells in distributed brain regions receive a range of sensory inputs, but visual input is particularly important for aligning their responses to environmental landmarks. To investigate how population-level heading responses are aligned to visual input, we recorded from retrosplenial cortex (RSC) of head-fixed mice in a moving environment using two-photon calcium imaging. We show that RSC neurons are tuned to the animal's relative orientation in the environment, even in the absence of head movement. Next, we found that RSC receives functionally distinct projections from visual and thalamic areas, and contains several functional classes of neurons. While some functional classes mirror RSC inputs, a newly discovered class coregisters visual and thalamic signals. Finally, decoding analyses reveal unique contributions to heading from each class. Our results suggest an RSC circuit for anchoring heading representations to environmental visual landmarks.

3.2 Introduction

A sense of direction is essential for animals to accurately perceive and move through their environment. Rather than being coupled to absolute coordinates, such as magnetic north, direction is represented in the brain as the relative orientation of an animal in its current environment, termed “heading”. Although heading and head direction are generally aligned in a freely moving animal, they can be experimentally decoupled when head movement and environmental movement are independent. For example, researchers have observed heading responses in insects that track the movement of a virtual environment even with the head immobilized [114, 115, 116].

A distributed network [48, 117, 118, 119, 120] of head direction (HD) neurons found throughout the mammalian brain represent direction through increased firing when an animal’s head is in a specific orientation relative to the environment [121, 47, 122, 123, 48]. A central hub of this network is the ADN, which contains a high percentage of HD neurons and is crucial for navigation [123, 48, 124, 125]. Early investigations of responses in the HD cell network demonstrated that the vestibular system plays a critical role in both the generation and maintenance of HD neurons. Lesions of the vestibular system, either in sensory organs [126, 127, 87] or in upstream relay nuclei [128, 129], degrade the responses of HD neurons in ADN and other regions in the HD cell network, resulting in navigational deficits. Although HD cell responses have been observed in restrained rodents in virtual environments, all experiments to this point have involved physical head rotation, either animal-controlled [130, 131, 132, 133] experimenter-controlled [134, 135, 136]. Despite the importance of vestibular input, previous work has shown that the visual system, though not necessary for the generation of HD cell responses, plays a crucial role in anchoring the responses to cues in the external environment [47, 48, 134, 137]. Experiments which remove visual information by recording from animals in darkness, have shown that HD neuron firing gradually drifts from the animal's physical head direction over time [137, 47]. Moreover, turning on the lights results in a nearly instantaneous realignment of HD cell responses to visual cues, even if the cues were inconspicuously moved in the darkness, suggesting that visual information exerts a dominating influence on representations, supplanting cues from other sensory systems [138]. Indeed, behavioral experiments in several species that either dampen or remove vestibular information have shown that animals are still capable of successful navigation through the use of visual landmarks alone [139, 140, 127, 114, 141]; though other sensory inputs, such as optic flow [142, 131], proprioception [143], motor efference copy [144], and olfaction [145] also contribute. Although visual input is known to play a critical role in registering heading representations to the environment, the mechanism of alignment has not been fully elucidated.

Recent research has suggested that the RSC, a cortical region in the HD cell network, may play an important role in the integration of these signals [118, 119]. Lesioning RSC degrades HD cell responses in ADN [146, 147], suggesting that RSC directly contributes to HD cell tuning, which is further supported by reciprocal projections from RSC to ADN [148, 149, 150, 151]. Furthermore, RSC is one of only two principal areas, the other being the postsubiculum [148, 149], that receives direct innervation from both the visual cortex and the ADN. RSC also has important roles in navigation, particularly regarding landmark detection [152, 153, 154, 155, 156, 157] and path integration [158, 159], and has been shown to integrate visual information with vestibular input in the angular head velocity (AHV) system [160]. Finally, in the presence of conflicting visual landmarks, individual HD neurons in RSC exhibit multimodal tuning curves that capture the angular offset with respect to each landmark, suggesting that RSC can represent and resolve this ambiguity [155, 161]. These findings suggest that RSC is uniquely situated to receive and integrate sensory information from visual system into a unified representation of heading. Here, we use 2-photon calcium imaging of RSC cell bodies and axonal inputs to investigate how visual cues are used to register heading to the external environment.

3.3 Methods

3.3.1 Animals

For cortex-wide calcium indicator expression, Emx1-Cre (Jax Stock #005628) × ROSA-LNL-tTA (Jax Stock #011008) × TITL-GCaMP6s (Jax Stock #024104) triple transgenic mice or Slc17a7-IRES2-Cre (Jax Stock #023527) × TITL2-GC6s-ICL-TTA2 (Jax Stock #031562) double transgenic mice were bred to express GCaMP6s in cortical excitatory neurons. For axon imaging experiments, wild-type C57BL/6J mice were used. For all imaging experiments, 6-12 week old mice of both sexes (12 males and 10 females) were implanted with a head plate and cranial window and imaged starting 2 weeks after recovery from surgical procedures and up to a maximum of 10 months after window implantation. The animals were housed on a 12h light/dark cycle in cages of up to 5 animals before the implants, and individually after the implants. All animal procedures were approved by the Institutional Animal Care and Use Committee at UC Santa Barbara.

3.3.2 Surgical Procedures

All surgeries were conducted under isoflurane anesthesia (3.5% induction, 1.5–2.5% maintenance). Prior to incision, the scalp was infiltrated with lidocaine (5 mg kg-1, subcutaneous) for analgesia and meloxicam (2 mg kg-1, subcutaneous) was administered pre-operatively to reduce inflammation. Once anesthetized, the scalp overlying the dorsal skull was sanitized and removed. The periosteum was removed with a scalpel and the skull was abraded with a drill burr to improve adhesion of dental acrylic. For all chamber-rotation mice, a 4 mm craniotomy was made centered over the midline (centered at 3.0 mm posterior to Bregma), leaving the dura intact. For a subset of these mice, Syn-GCaMP7b was injected into either AM (3.0mm anterior, 1.7mm lateral), PM (1.9mm anterior and 1.6mm lateral to Lambda), or ADN (0.8 mm posterior and 0.8mm lateral to Bregma, 3.2 mm depth [162]). For head rotation experiments, the 4 mm craniotomy was centered 3.0 mm posterior and 1.0 mm lateral to Bregma, so that the axis of rotation was not centered over the sagittal sinus. A cranial window was implanted over the craniotomy and sealed first with silicon elastomer (Kwik-Sil, World Precision Instruments) then with dental acrylic (C&B-Metabond, Parkell) mixed with black ink to reduce light transmission. The cranial windows were made of two rounded pieces of coverglass (Warner Instruments) bonded with a UV-cured optical adhesive (Norland, NOA61). The bottom coverglass (4 mm) fit tightly inside the craniotomy while the top coverglass (5 mm) was bonded to the skull using dental acrylic. A custom-designed stainless-steel head plate (eMachineShop) was then affixed using dental acrylic. In all conditions, the head plate was carefully positioned to ensure a natural gait under recording conditions. After surgery, mice were administered carprofen (5 mg kg^{-1}, oral) every 24h for 3 days to reduce inflammation. The full specifications and designs for head plate and head fixation hardware can be found on our institutional lab website (`https://goard.mcdb.ucsb.edu/resources`).

3.3.3 Floating chamber design and set-up

For the floating chamber experiments (Figure 1A), we used a set-up based on the Mobile HomeCage system (Neurotar Ltd.). Briefly, a 250 mm diameter carbon fiber chamber was placed on top of a perforated metal base. Pressurized air fed into the metal base floated the chamber, reducing friction and allowing the chamber to move readily. Mice were then head fixed in the center of this chamber and allowed to ambulate, which moved the chamber around the mouse while the mouse remained still. The air pressure was tuned (2-4 PSI) so that the chamber provided enough friction to create a natural gait. The chamber contains a set of magnets which are read by the base in order to report information about the position of the chamber (Tracking Software v2.2.1, Neurotar Ltd.), which are then transformed using custom code (MATLAB 2020b, Mathworks) to extract the position, angle and velocity of the mouse relative to the chamber.

For single cue experiments, the walls of the chamber contained a single black cue (width: 60mm) set on top of a white noise background that spanned the entire inner circumference of the chamber.

For dual cue experiments, the walls of the chamber contained a repeating pattern of stars or bars (width: 180mm), in an A - B - A - B pattern. These stimuli were separated by black bars to separate the cues (width: 15mm).

For remapping experiments, the walls of the chamber was divided into four quadrants, each with a different stimulus. Between recordings, the stimuli were replaced with four new unique stimuli in complete darkness, so that the mouse could not see the transition between stimuli.

All wall cues were printed on nylon waterproof paper and attached to the chamber walls using double-sided tape.

Forced rotation experiments

To ensure even sampling of the entire rotation space, we carefully controlled the rotation of the chamber. Three stabilizing bearings (608-2RS) were mounted on optical posts (TR-series, Thorlabs) and placed around the cage to eliminate any X-Y translation.

A DC motor (ZGA37RG, Greartisan) was coupled to a rubber wheel and used to spin the chamber using the outer surface. The speed of the DC motor was controlled with a microcontroller (UNO R3, Arduino) drive the rotation of the chamber (3-7 rpm).

The chamber was rotated for 90 - 120s followed by a 5s rest period, which was then repeated 2 - 6 times for each recording. Mice were monitored via video to ensure that they followed along with the chamber rotation. The total time spent rotating on the floating air chamber never exceeded 15 minutes, in order to limit potential discomfort.

For experiments in light and darkness, the lights in the experimental box were switched using a microcontroller (UNO R3, Arduino). The initial repeat was always performed in a light on trial, so that the mouse could register visual landmarks in its environment. Afterwards, the box lights were turned on or off in between repeats, during the rest period.

The chamber was thoroughly cleaned and disinfected between experiments in order to remove any odor traces.

Physical head rotation experiments

The head rotation apparatus consisted of a rotation collar (LCRM2, Thorlabs Inc.) attached to a translating mount (LM2XY, Thorlabs Inc.) and a quick release adapter (SM2QA, Thorlabs Inc.) The translating mount allowed for independent adjustment of the imaging field about the axis of rotation to optimize the imaging field. The quick release adapter was used in order to easily head fix mice to the apparatus. A closed timing belt for 3D printers (2GT-610) was looped around the rotation collar and attached to a DC motor (ZGHA37RG, Greartisan) and belt tensioner (6mm belt pulley). Due to the danger of physically rotating the mouse, we limited the speed of the head rotation to 2 rpm and installed safety bars alongside the body of the mouse to ensure that the body of the mouse did not become twisted under the collar.

3.3.4 Two-photon imaging

After >2 weeks recovery from surgery, GCaMP6s fluorescence was imaged using a Bruker Investigator two-photon microscopy system with a resonant galvo-scanning module. Posterior dysgranular RSC was targeted by imaging just lateral of the sagittal sinus and just anterior the the transverse sinus.

For fluorescence excitation, we used a Ti:Sapphire laser (Mai-Tai eHP, Newport) with dispersion compensation (DeepSee, Newport) tuned to $\lambda = 920nm$. For collection, we used GaAsP photomultiplier tubes (Hamamatsu). To achieve a wide field of view, we used a 16×0.8 NA microscope objective (Nikon) and imaged at a $414 \times 414\mu m$, $690 \times 690\mu m$, or $829 \times 829\mu m$ field of view spanning 760×760 pixels. Laser power ranged from 40 to 75mW at the sample depending on GCaMP6s expression levels. Photobleaching was minimal ($< 1\%$ min^{-1}) for all laser powers used. A custom stainless-steel light blocker (eMachineShop) was mounted to the head plate and interlocked with a tube around the objective to prevent ambient light from reaching the PMTs.

3.3.5 Two-photon post-processing

Images were acquired using PrairieView acquisition software (Bruker) at 10Hz and converted into TIF files. All subsequent analyses were performed in MATLAB (Mathworks) using custom code. First, images were corrected for X-Y movement by registration to a reference image (the pixel-wise mean of all frames) using 2-dimensional cross correlation.

To identify responsive neural somata, a pixel-wise activity map was calculated using a modified kurtosis measure. Neuron cell bodies were identified using local adaptive threshold and iterative segmentation. Automatically defined ROIs were then manually checked for proper segmentation in a graphical user interface (allowing comparison to raw fluorescence and activity map images). To ensure that the response of individual neurons was not due to local neuropil contamination of somatic signals, a corrected fluorescence measure was estimated according to:

$$F_{\text{corrected}}(n) = F_{\text{soma}}(n) - \alpha(F_{\text{neuropil}}(n) - \overline{F}_{\text{neuropil}}) \tag{3.1}$$

where F_{neuropil} was defined as the fluorescence in the region $< 30\mu m$ from the ROI border (excluding other ROIs) for frame n. $\overline{F}_{\text{neuropil}}$ is $F_{neuropil}$ averaged over all frames. α was chosen from $[0, 1]$ to minimize the Pearson's correlation coefficient between $F_{\text{corrected}}$ and F_{neuropil}. The $\Delta F/F$ for each neuron was then calculated as:

$$\Delta F/F = (F_{\text{n}} - F_0)/F_0 \tag{3.2}$$

where F_n is the corrected fluorescence ($F_{corrected}$) for frame n and F_0 defined as the mode of the corrected fluorescence density distribution across the entire time series.

De-rotation of image time series

Because the microscope is fixed relative to the mouse in the head rotation experiments, the images from the microscope were de-rotated in order to be properly processed [163]. The initial non-rotation period was used to create a template that the remainder of the images would be registered to. Registration was performed by maximizing the Mattes mutual information between each frame and the template via a one plus one optimizer (MATLAB, Mathworks). The geometric transformation of the previous successfully registered image was applied as an initial transform in order to optimize the performance and speed of the registration. After de-rotating each frame, an occupancy map was calculated from the resulting images, and the image was cropped so that only areas that contained all frames were included in further analyses. The final image series was subsequently analyzed using the two-photon processing pipeline described above.

Axon terminal imaging

For axon terminal imaging, we processed the TIF files using the Python implementation of Suite2P [164]. Briefly, TIFs underwent rigid registration using regularized phase correlations. Regions of interest were extracted via clustering correlated pixels, and were manually checked based on location, morphology, and $\Delta F/F$ activity. A specific configuration of Suite2P was used that is optimized for detecting axon processes [165]. After defining ROIs, we used custom code (MATLAB) to check that the same axon process was not sampled multiple times (for ROIs with Pearson correlation > 0.5, one ROI was excluded).

3.3.6 Analysis of calcium data

To avoid low pass filtering of heading tuning curves due to slow calcium dynamics, we used a MATLAB implementation of a sparse, nonnegative convolution algorithm (OASIS) on $\Delta F/F$ traces [166] with an auto-regressive model of order 1 for the convolution kernel.

For the floating chamber experiments with voluntary control, the Rayleigh vector length (RVL) was used to determine if a cell was heading selective. The RVL was calculated for each cell and compared against a shuffled distribution. To create the shuffled distribution, each cell's spike data was circularly shuffled and the tuning curve and resulting RVL was calculated. This was repeated 1000 times to create a distribution of shuffled RVLs. Cells whose true RVL met or exceeded the 99^{th} percentile of this distribution were considered to be heading selective.

For calculation of heading selectivity in the rotating chamber experiments, each cell's spike time series was divided into trials, with each trial representing a single full rotation of the chamber. To calculate tuning curves, the orientation of the chamber at each frame was first binned into 60 bins of 6 degrees. Then, the response was calculated for each trial using the spike rate of the cell at each heading bin, smoothed by a 15°moving average filter. The overall tuning curve was calculated by averaging the responses across all trials.

Next, we determined whether each cell (or axon terminal) was significantly heading selective. First, the reliability each cell's heading preference across trials was calculated by randomly splitting the trials into two groups and calculating the correlation coefficient between the resulting tuning curves. Then, each trial's activity was circularly shifted prior to calculating the correlation coefficient. This was repeated 1000 times for each cell, creating a real and shuffled distribution, which was compared via a two-sample Kolmogorov-Smirnov test.

Cohen's d was calculated to gauge the separation between the two distributions. A cell was considered reliable if it passed the two-sample Kolmogorov-Smirnov test at $p < 0.1$ and had a Cohen's $d > 0.8$. Additionally, A single-term (for single cue) or two-term (for dual cue) gaussian was fit to the trial averaged tuning curve as well as the trial averaged shuffled tuning curves. As before, the tuning curves were shuffled and fit 1000 times. The goodness of fit (r^2) of the true fit was compared against the 90^{th} percentile of r^2 for the shuffled fits to determine if the cell's tuning curve had the proper shape. These threshold values were chosen so that the combined significance value of the two measures is $p = 0.01$. When repeating these procedures using pre-shuffled data, no cells passed these criteria, suggesting that the number of heading selective cells is accurate, and not due to chance.

To compare tuning curves across cells regardless of preferred direction, a cross-validated alignment was performed. For each trial, the responses from every other trial was used to construct a tuning curve, and the peak index of that tuning curve was used to align the held out trial. For light-on and light-off experiments, individual tuning curves for each condition were first calculated by only averaging trials that belonged to each light condition. Cross-validated alignment was performed on the light-on tuning curves, and the offsets applied to the light-off tuning curves, so that the same circular offset was applied to both conditions.

Calculation of coherent remapping

To determine whether or not a population of neurons remapped coherently, we created cross-validated procedure for testing individual cells. For each neuron in a recording, the difference between its preferred direction in the first and second context was calculated. Next, all other cells in the recording were used to calculate an "expected offset" by taking the median across all cell pair differences in preferred direction across contexts. Lastly, the difference between the neuron of interest and the median difference was taken to determine if the neuron of interest remapped coherently with the remainder of the population. This procedure can be summarized as follows:

$$\Delta\text{phase offset}_n = (\text{pref}_{(A,\,n)} - \text{pref}_{(B,\,n)}) - (\widetilde{\text{pref}}_{(A,\,[0,\,N]\neq n)} - \widetilde{\text{pref}}_{(B,\,[0,\,N]\neq n)}) \tag{3.3}$$

where pref_A and pref_B is the preferred direction in context A or B, respectively, of neuron n and N is the total number of neurons. $\widetilde{\text{pref}}$ denotes the median of preferred directions. Perfect remapping would result in a difference of 0, suggesting that each neuron exhibited the exact same heading offset as the rest of the population. This process was repeated for each recording to measure the amount of coherent remapping for each neuron in each recording. These values were compared against a shuffled distribution, in which random neurons were chosen and compared, rather than defined cell pairs.

Clustering of RSC soma responses

To categorize the response profiles of RSC somata, unsupervised clustering was performed. First, all cells were fit with a sum of Gaussians as defined below for both light-on and light-off conditions:

$$f(x) = a_0 + a_1 \times e^{-((x-b_1)/c_1)^2} + a_2 \times e^{-((x-b_2)/c_2)^2} \tag{3.4}$$

where a_0 is the baseline offset, a_1, b_1, c_1, a_2, b_2, and c_2 are the amplitude, location, and standard deviation for the first and second peaks, respectively. The coefficients a_1, a_2, c_1 and c_2 for each the light-on and light-off tuning curves were fit with an 8 component Gaussian mixture model (GMM). Coefficients b_1 and b_2 were omitted so that the location of the peak was not a determining factor in clustering. A cluster evaluation using silhouette analysis was performed to determine the optimal number of clusters, which reported a local maximum at $k = 3$ clusters, resulting in a 3 component Gaussian mixture model (GMM). Following clustering by the GMM, an additional exclusion step was performed to remove cells with poor tuning curves. The archetypal cluster response was created by averaging all the tuning curves within a single cluster, and the correlation coefficient between each member and the archetypal response was calculated. Individual cells with a correlation < 0.5 were moved to an unclassified cluster.

Because of the high dimensionality of the GMM components, a dimensionality reduction was performed for visualization (Figure 5B). First, the GMM was used to generate 100,000 data points from the three defined components. An LDA was trained on these data points, and the weights from the trained model were used to reduced the dimensionality of the real data to the first two dimensions for visualization.

Calculation of light sensitivity

Light sensitivity was calculated as an index based on the Rayleigh vector length (RVL) of each tuning curve. Because the RVL considers both direction and magnitude, we first used an angle doubling procedure to turn bimodal distributions into unimodal distributions, similar to previous work [155]. The RVL index was then calculated for the light-on and light-off tuning curves as follows:

$$RVL_{\text{index}} = (RVL_{\text{ON}} - RVL_{\text{OFF}})/(RVL_{\text{ON}} + RVL_{\text{OFF}}) \tag{3.5}$$

where RVL_{ON} is the cell's RVL in light-on and RVL_{OFF} is the cell's RVL in light-off. This index ranges from $[-1, 1]$, with values closer to -1 indicaitng stronger tuning in light-off, value closer to 1 indicating stronger tuning in light-on, and values around 0 indicating equal strength tuning in both conditions.

Calculation of bimodality

To represent the bimodality of a neuron, we used a flip score metric also described previously [155]. Briefly, an autocorrelation of each cell's tuning curve was performed. A bimodal cell resulted in a peak centered at 180°, which was absent in unimodal cells. The flip score was then calculated as follows:

$$\text{Flip Score} = CC_{180^\circ} - (CC_{90^\circ} + CC_{270^\circ})/2 \tag{3.6}$$

where CC_{180°, CC_{90°, and CC_{270° are the correlation coefficients of the autocorrelation at the 180°, 90°, and 270°positions, respectively.

Calculation of input index

An input index was calculated to determine the degree of similarity between each RSC soma's tuning curve and ADN or visual axonal responses. First a two-term Gaussian was fit to tuning curves from the ADN or visual cortical axonal responses, similar to for clustering rsc soma. Then a Gaussian mixture model was independently fit to each of the datasets, so that there was a single GMM for the ADN axonal data and another for the visual cortical axonal data. Next, the Mahalanobis distance was calculated for each rsc soma to each GMM. Finally, the input index was calculated as follows:

$$\text{Input Index} = (D_{\text{VIS}} - D_{\text{ADN}})/(D_{\text{VIS}} + D_{\text{ADN}}) \tag{3.7}$$

: where D_{ADN} is the Mahalanobis distance between each cell and the center of the GMM fit to the ADN axon data, and D_{VIS} is the same, but for the visual cortical axon data. Scores closer to -1 indicate that the cell has tuning more similar to ADN and scores closer to 1 indicate that the cell has tuning more similar to visual cortical projections.

3.3.7 Decoding RSC somatic activity

Preprocessing and alignment of calcium data

In order to aggregate trial data across all recordings, the follow preprocessing steps were performed. First, each rest period in which the chamber does not rotate between light-on and light-off conditions was identified. Individual trials were then defined as full rotations either preceding or following the rest period, so that each trial contained a full rotation of the chamber. For light-off to light-on conditions, the rest period was identified that separated light-off from light-on periods. By defining full trials about the rest period, each trial was ensured to fully span 360°. Next, minor variations in the speed of rotation between individual trials were accounted for by resampling both the heading information and neural data to be equal length (200 bins) across all trials in all recordings. Last, to ensure that the training data were not used for decoding, we calculated each cell's tuning curve on a trial by trial basis, including all data except those associated with that trial. Therefore, each trial had an associated tuning curve constructed of that cell's response in all trials except the one currently being decoded.

For single recording decoding (Figure 1J), recordings with fewer than 10 heading cells were excluded.

Decoding strategy

After preprocessing, the data were aggregated and used to decode heading on a trial by trial basis [167]. First, a population-level likelihood curve was constructed as follows:

$$\text{likelihood}_t = (\vec{FR_t} \times T) \oslash \sum(\vec{FR_t} \times T) \tag{3.8}$$

where $\vec{FR_t}$ is a vector of firing rates of all neurons at time t, T is a matrix containing the tuning weights of all neurons, and $\oslash$ represents element-wise division. The index of the maximum likelihood of the curve was used to determine the decoded heading bin at each time point.

Calculating decoder performance metrics

Because each pseudopopulation had uneven numbers of neurons, we first performed a bootstrapping procedure prior to calculating performance metrics. We sampled, with replacement, neurons from each group, with the number of neurons determined by the size of the smallest group ($n = 162$ cells). The analysis was performed on sampled subpopulations for 1000 iterations to calculate the mean and bootstrapped s.e.m. at each time point.

The decoder error for each frame was calculated as follows:

$$\text{Decoder Error} = |H_{\text{decoded}} - H_{\text{actual}}| \tag{3.9}$$

where H_{decoded} is the decoded heading at each frame and H_{actual} is the actual heading at each frame. Because of the overrepresentation of 180°errors due to the landmark cell contribution, we found that the average decoder error did not well represent the actual trial performance. Therefore, in addition to decoder error, we calculated the decoder accuracy for each trial as follows:

$$\text{Decoder Accuracy} = \sum (\text{Decoder Error} < 18^{\circ})/N_{\text{frames}} \times 100 \tag{3.10}$$

where N_{frames} is the total number of frames in the current trial.

Decoder accuracy was displayed as bootstrapped plots with error bars denoting the 2.5^{th} and 97.5^{th} percentile. If the confidence interval did not overlap chance (0.18), the decoder accuracy was deemed to be statistically significant. The specific decoding and decoder error examples in the Figure 6 plots were taken from the iteration with median performance based on decoder accuracy to illustrate a representative decoding session.

3.3.8 Statistical Information

To test decoding error across recordings, paired t-tests were performed. To test whether angular data were clustered around a mean angle, a V-test was performed (Circular Statistics Toolbox, MATLAB). To compare the differences between two distributions, a two-sample Kolmogorov-Smirnov test was performed. For all other significance testing, bootstrapped 95% confidence intervals were calculated. The confidence intervals were then compared against either other confidence intervals or reference numbers. If there was no overlap between the confidence interval and the reference, it was considered to be statistically significant. When performing bootstrapping, data were randomly sampled with replacement. Statistical comparisons between groups were performed as two-tailed tests.

3.3.9 Code Availability

Th-e code for generating all figures is available on the following GitHub repository: `https://github.com/kevinksit/HeadDirectionProject`

3.4 Results

3.4.1 Neurons in the RSC represent heading in the absence of physical head movements

In order to investigate the interaction of visual input and heading using 2-photon imaging of somata and axon terminals, we developed a preparation in which mice are head restrained in a moving environment (Figure 3.1A). To clarify our terminology, in previous studies the relative orientation of the head to the environment was generally determined by physical movement of the animal's head in a stationary environment, leading to the term "head direction cells". Since our experiments have the head immobilized, we define tuned neurons as "heading" cells, since they represent the relative orientation of the stationary head to a moving environment. Heading responses have been found in invertebrates in preparations in which the head is immobilized [114, 115, 116], but to date all experiments investigating HD cells in mammals have incorporated physical head movement [131, 130, 132, 133]. Virtual reality systems [168, 169, 132, 170] are commonly used for navigation tasks in head-fixed preparations, but have some significant drawbacks, such as a lack of depth cues, somatosensory feedback, and limited proprioceptive input. To address these limitations, we opted to use a walled circular chamber that floats on an air table [171], and contains an array of sensors to collect measurements from the chamber, including linear position, angular orientation, and speed (Figure 3.1A, D, see Methods). This approach holds vestibular input constant, while allowing the mice to experience the visual and proprioceptive inputs associated with movement relative to the environment.

To determine if mammalian RSC neurons show tuning for heading even when the head is stationary, we allowed head-fixed mice to ambulate within a floating chamber while simultaneously imaging from the posterior dysgranular RSC ($n = 4$ recordings over 3 mice, Figure 3.1B). Posterior dysgranular RSC was chosen because it receives direct projections from visual cortex [150, 157, 172]. To avoid excessive smoothing of heading responses due to the slow temporal dynamics of calcium imaging, we deconvolved the calcium traces and inferred spikes for all analyses (Figure 3.1C). We then measured the response of each neuron as a function of the angular position of the cue card, revealing that a proportion of neurons in RSC faithfully represent heading (14.0%, 373/2665 neurons; Figure 3.1D-E), similar to the proportion found in freely moving rodents [118, 119]. However, we observed that mice did not always fully sample the entirety of the cage in each recording (Figure 3.2). Additionally, mice may have been able to use other sensory cues besides vision, such as odor, to determine their heading.

To isolate the visual contribution to heading representations, we transitioned to a controlled rotation design. We used guide bearings to limit translation while rotating the chamber with a motorized wheel (Figure 3.1F). This approach has three distinct advantages: 1) it creates a regular trial structure in the data, 2) it ensures equal sampling of the entire range of headings, and 3) it reduces changes in the appearance of the visual

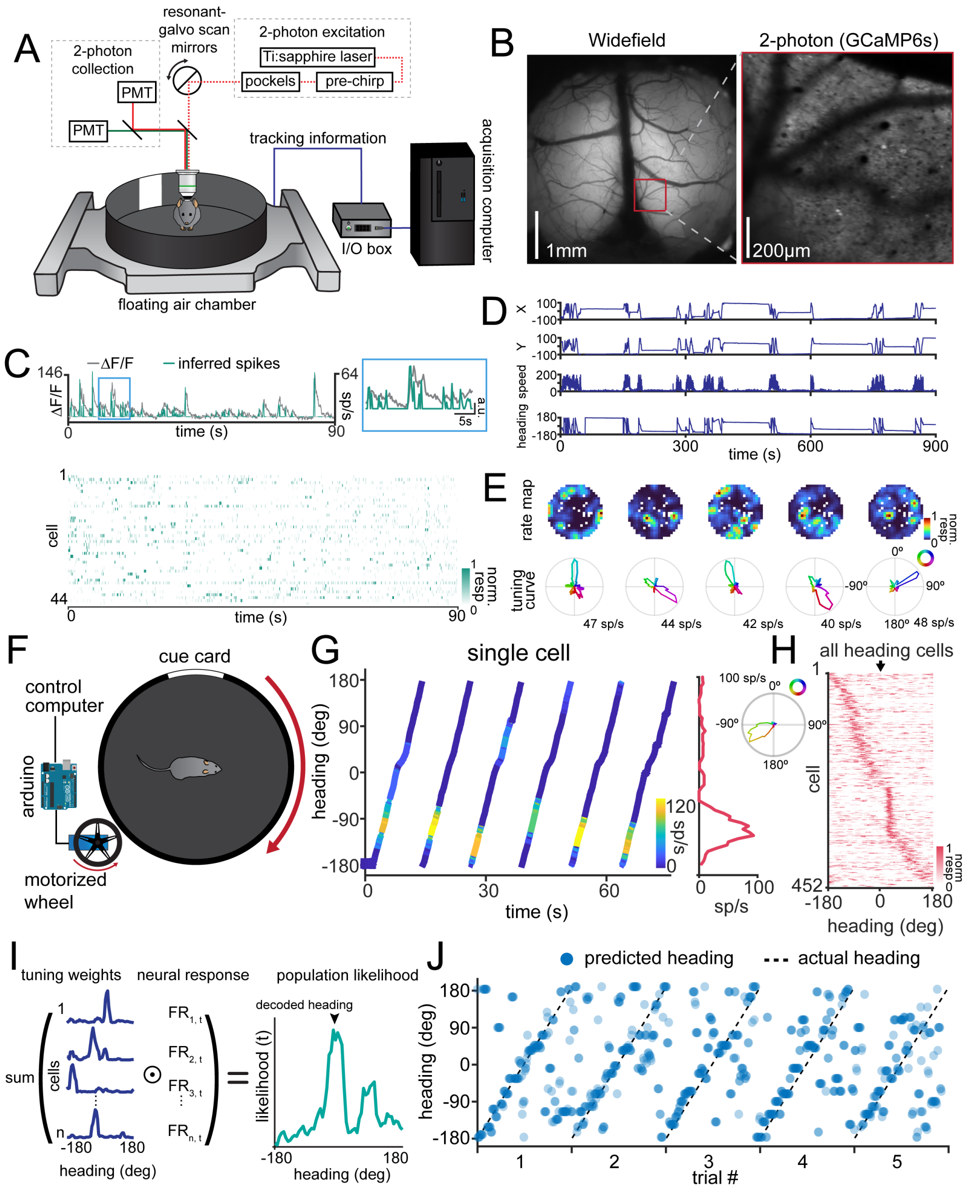

Figure 3.1: Individual neurons in the RSC exhibit heading responses in the absence of physical head movement. **A)** Schematic of the imaging set up. **B)** *Left:* Example widefield image. Scale bar = 1 mm. *Right:* Example two-photon image. Scale bar = 200 μm. **C)** *Top:* Spike inferencing method. Gray traces show the $\Delta F/F$ trace and the green trace shows the inferred spikes. *Inset:* Zoomed section of the blue box on the left. *Bottom:* Example inferred spikes. **D)** Example chamber tracking data from a single experiment. **E)** Example rate maps (top) and tuning curves (bottom) from neurons recorded from RSC. **F)** Schematic of the controlled rotation set up. **G)** *Left:* Example of a single neuron's response to rotation in the chamber. *Right:* Average tuning curve across all trials. **H)** Tuning curves of all responsive neurons. **I)** Schematic of the decoding method. ⊙ represents elementwise multiplication. **J)** Decoding of heading from population responses from a single recording.

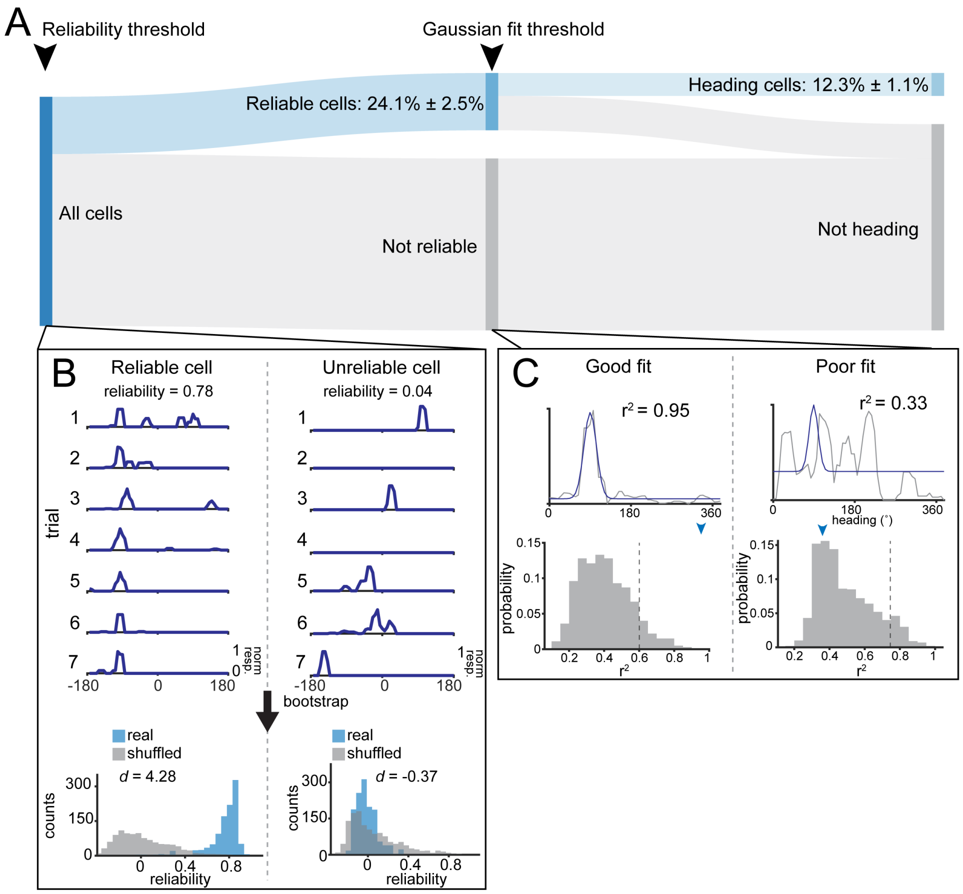

Figure 3.2: Schematic of procedure for determining whether a cell is heading responsive. **A)** Sankey diagram showing the percentage of cells passing each selection criteria for determining heading responsiveness. All cells first pass through a reliability threshold, followed by a Gaussian fit threshold. Both thresholds were calculated via a shuffling procedure (see Methods). Only cells which pass both thresholds were included in analyses. **B)** Schematized reliability threshold using an example cell. *Left:* Trial-by-trial tuning curves for a reliable neuron showing a prominent peak in the same location over trials. Below are histograms comparing bootstrapped reliability of this cell versus a shuffled distribution. *Right:* Same as *left*, but for an unreliable cell. **C)** Schematized procedure for Gaussian fit threshold. *Left:* Cells are fit with a single term Gaussian. A shuffled distribution of r^2 is created by circularly shifting tuning curves from each trial (see Methods). The distributions of r^2 are shown with a dotted line denoting the 99^{th} percentilie and the blue arrow showing the reliability of the current cell. *Right:* Same as *left*, but for a poorly fit cell.

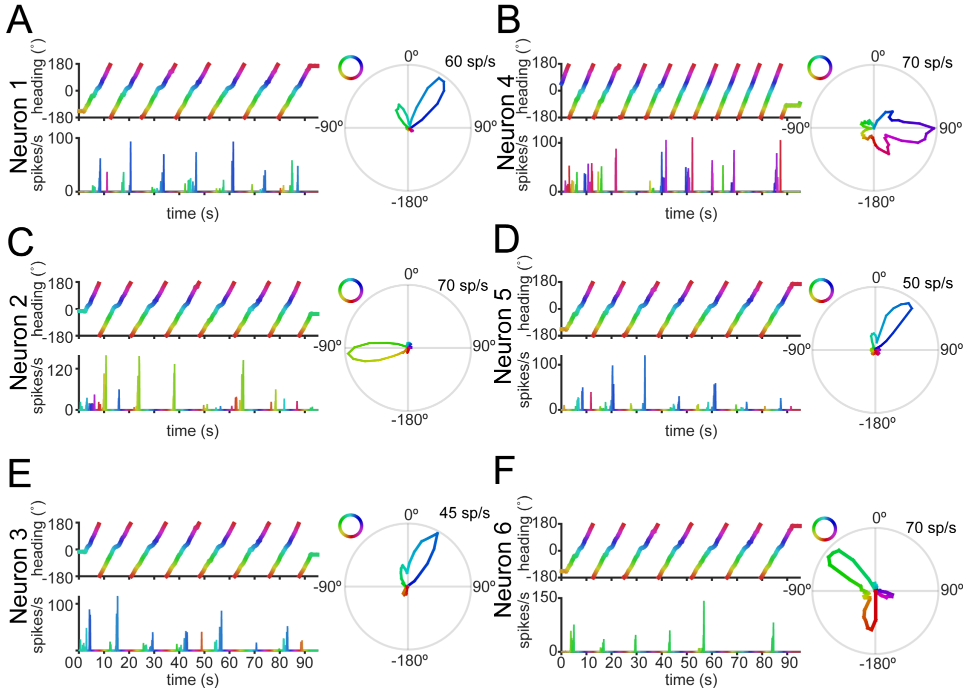

Figure 3.3: Neurons in the controlled rotation condition represent heading faithfully over multiple trials. **A)** *Left, top:* Recorded heading over time, color coded by the current heading. *Left, bottom:* An example neuron's spike rate over the same duration, with the color of the line matched to the heading shown above. The similar color of the peaks show that the neuron is responding to the same heading on each trial. *Right:* Tuning curve from the example neuron constructed across all trials. For clarity, only a single block of consecutive trials is shown here for each neuron. **B-F)** Same as **A** for additional example neurons.

cues due to variable proximity during chamber translation. To take advantage of the trial structure of our data, we created a new method with a low false positivity rate to determine if a neuron was heading selective (Figure 3.3, see Methods).

Using this method, we found a similar percentage heading neurons as in the experiments without controlled rotation, comprising 14.2% (452/3179 neurons) of the total number of cells recorded ($n = 16$ recordings over 5 mice, Figure 3.1G, Figure 3.4). We wanted to ensure that the recorded cells were not simply activated by the passing of the visual cue over a visual receptive field. We aligned all the cells using their cross-validated preferred direction (see Methods), showing that heading-responsive cells tile the entire

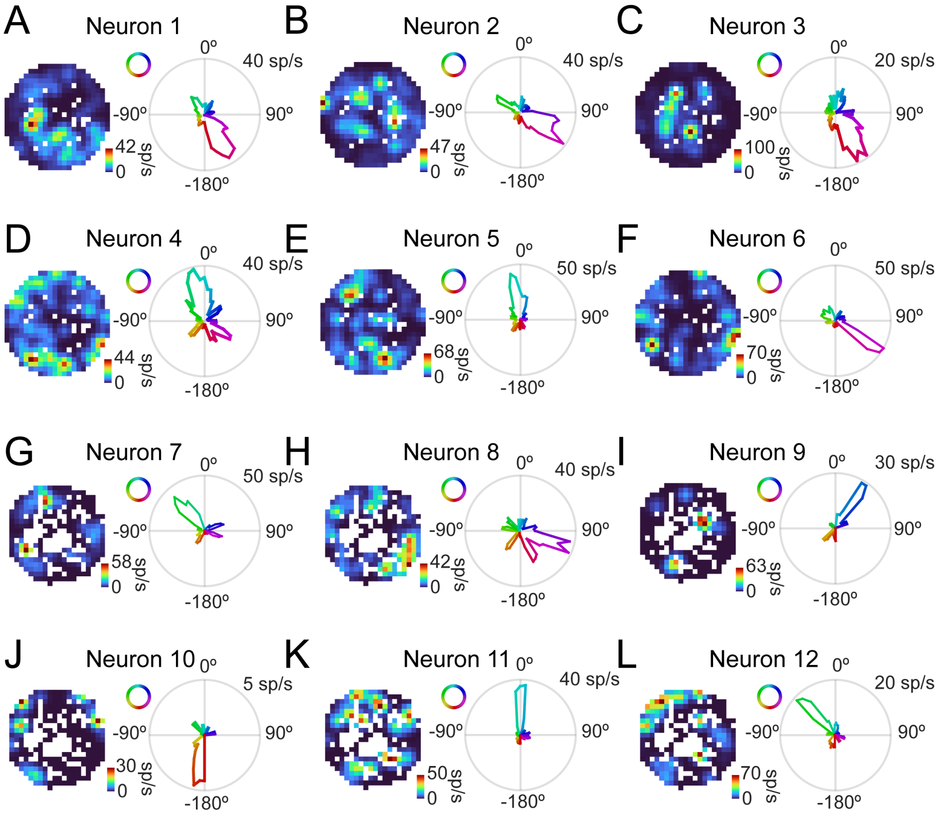

Figure 3.4: RSC neurons represent heading during locomotion in the floating chamber. **A)** *Left:* Example spike rate heat map of a single neuron, showing the neuron's response as chamber moves around the mouse. *Right:* Example tuning curve from the same neuron. **B-L)** Same as **A** for additional example neurons.

circumference of the chamber, even when the cue card is outside of the visual field of the mouse; though we note there is overrepresentation of responses when the cue is centered in front of the mouse at 0° (Figure 3.1H).

This suggests that the cells that we recorded are not simply relaying visual information. Next, we created a decoder to confirm that the population of recorded cells in a single recording contained sufficient information to accurately represent the heading of the animal. Briefly, the decoder uses the tuning curve of each neuron scaled by the activity at each time point to construct a population likelihood of perceived heading, and then selects the maximum likelihood as the predicted heading for that time point (Figure

3.1I). Using all of the heading cells in single recording, the decoder was able to predict the location of the cue card significantly above chance over multiple trials. ($t_8 = 5.4$, $p = 6.6 \times 10^{-4}$, paired t-test; Figure 3.1J). Together, these results suggest that the visual and proprioceptive input from the rotating chamber sufficiently drive dysgranular RSC neurons to accurately represent heading, even in the absence of vestibular modulation.

3.4.2 Heading cells exhibit similar preferred directions during rotation of the animal or the environment

Previous research has emphasized the importance of vestibular information for the function of the heading network [173], so we next investigated whether the same neurons exhibit matched tuning during head fixation in a rotating environment versus during rotation of the head in a fixed environment. To address this, we added a belt-driven rotation collar to the previous experimental set up, allowing physical rotation of the mouse head plate with the window centered underneath the imaging objective (Figure 3.5A). The rotation had a constant, low angular velocity to allow the animal to walk along as the head plate was rotated. This approach allowed us to compare responses in the same neurons across two conditions: 1) in which the head rotates but the chamber is fixed or 2) in which the chamber rotates while the head is fixed ($n = 5$ recordings across 4 mice; Figure 3.5B). Since the head is physically rotating under the microscope objective, we first registered each frame to a template calculated from the average frame during the chamber rotation recording (Figure 3.5C). After registration, we defined a single set of ROIs across the two recordings and manually checked the quality of each ROI for size, shape, and brightness to identify ROIs that contained the same cell across conditions (Figure 3.5D). We found that many neurons, though not all of them, exhibit similar tuning across the two conditions, with small differences in preferred direction

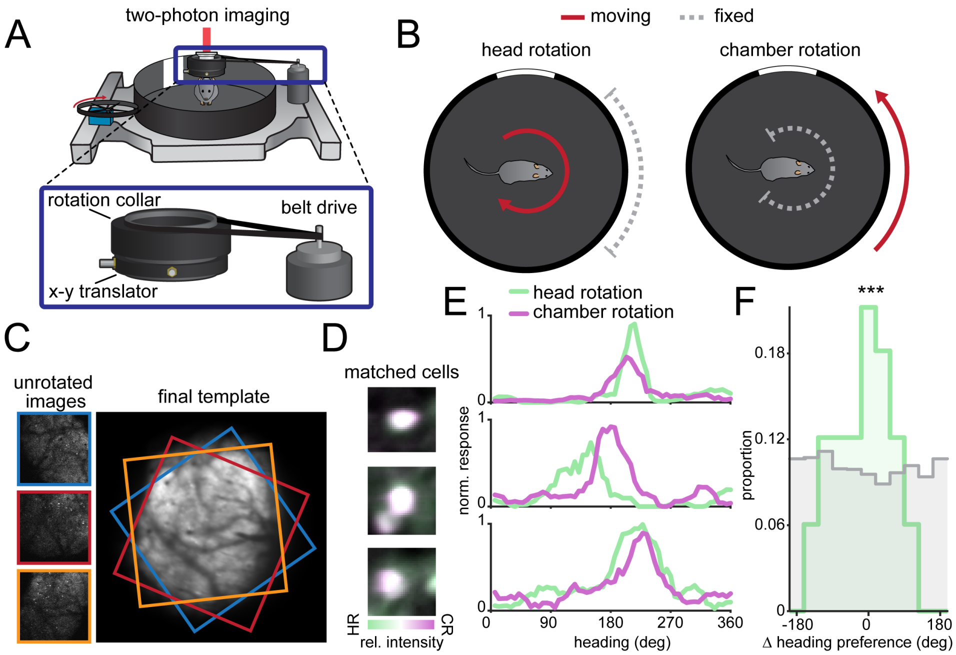

Figure 3.5: Neurons in the RSC retain similar tuning in head-rotation or chamber-rotation conditions. **A)** Example of the adapted head-rotation set up for comparisons between head-rotation and chamber-rotation experiments. In addition to the motor-driven wheel that can rotate the chamber while the head is immobilized, there is a separate rotation collar that can be used to rotate the mouse over the stationary chamber. *Inset:* Zoom in of the rotation collar assembly. The rotation collar contains an x-y translator to shift the axis of rotation to the center of the imaging field. A belt-drive connects the collar to a motor for controlled rotation. **B)** Schematic of the two experimental conditions. Either the chamber or the head rotates independently, shown with a red arrow, while the other remains stationary, shown with a dashed gray capped line. In both cases, this causes the visual cue card to move across the visual field in the same direction. **C)** Example of derotation process for image timeseries. Each of the three raw images is rotated to match the template on the right. Colored borders show the position and rotation of each individual image. The final template shown on the right is after all the images have been registered for the recording. **D)** Example of three matched ROIs from the recordings. Purple denotes greater brightness in the chamber-rotation recording, whereas green denotes greater brightness in the head-rotation recording. White denotes equal brightness and suggests good alignment of the ROIs across recordings. HR: Heading rotation, CR: chamber rotation **E)** Three example tuning curves from pairs of ROIs showing similar tuning preferences. The tuning curve in the head rotation condition is shown in green, whereas the tuning curve in the chamber rotation condition is shown in purple. **F)** Histogram showing the difference in peak heading preference across recordings for matched ROIs. The zero-centered peak in the data (green) indicates that cells remained tuned to the similar heading angles independent of head- or chamber-rotation. Shuffled distribution is shown in gray. ***: $p < 0.001$, V-test for circular nonuniformity against 0°.

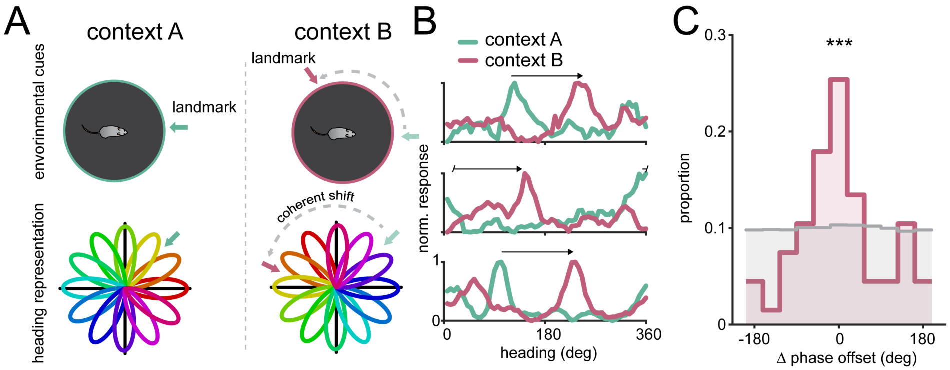

Figure 3.6: The heading network coherently remaps when visual cues are changed. **A)** Schematic showing coherent remapping across two different contexts. Because each individual neuron's preferred heading is mapped as a relative offset to visual landmarks, the relationships between neuron offsets would be expected to be preserved across contexts, leading to a coherent population shift. **B)** Three example neurons showing a unified shift in preferred heading from context A to context B. Tuning curve from context A is shown in green, while tuning curve from context B is shown in purple. Arrow shows the phase offset between contexts. **C)** Histogram showing that neurons coherently remap across conditions. For each recording session, a neuron's coherence with the population was calculated as the difference between the neuron's degree of remapping and averaged degree of remapping across the remainder of the population (see Methods). The peak around 0 suggests in the real data (purple) shows that individual neurons are shifting preferred directions in a similar amount to the rest of the population in each recording. Shuffled distribution is shown in gray. ***: $p < 0.001$, V-test for circular nonuniformity against 0°.

($V(32) = 14.1$, $p = 2.5 \times 10^{-4}$, V-test for nonuniformity against 0°; Figure 3.5E). Across all recordings, matched ROIs on average have the same heading preference with respect to wall pattern across conditions, suggesting that cells accurately represent heading with respect to the chamber's visual cues irrespective of head or chamber rotation (Figure 3.5F). Not all cells retain the same heading preference, possibly due to distal visual cues past the walls of the chamber, which are not informative in the chamber rotation condition, but provide potential landmarks in the head rotation condition.

3.4.3 Changing visual cues elicits coherent remapping in RSC neurons

The previous experiment demonstrates that many of the neurons we found that are tuned to changes in head angle are also tuned for changes in the rotation of the environment. Next, we wanted to confirm that heading-tuned neurons observed during head rotation exhibit similar population dynamics as HD cells. HD cells have been found to remap in different environments, while maintaining a constant angular offset between pairs of HD cells. As a consequence, moving an animal to an environment with new visual landmarks elicits "coherent remapping" [174], as the entire population rotates to align to the new landmarks, while retaining the same relative offsets between neurons (Figure 3.6A). To test whether heading cells in the rotating environment also have this quality, we replaced all of the visual cues on the chamber wall between recordings to alter the local landmarks and elicit remapping, creating two separate contexts. When comparing the same cells across the two contexts, we found that the majority of heading cells indeed shift by the same angular offset ($n = 12$ recordings over 4 mice; Figure 3.6B). The angular offset is not consistent across different recordings because the remapping due to changing contexts is random. Therefore, to compare across recordings, we first calculated the "phase offset" of each neuron, defined as the difference in preferred heading across conditions. Then, iterating through each neuron, we subtracted each neuron's phase offset to the averaged phase offset of all other neurons in the same recording ("Δ phase offset"; see Methods) to determine whether the neuron coherently remapped along with the population. When combining measurements across all recordings, we found that changing contexts caused the population of heading cells to coherently remap, as indicated by low Δ phase offsets ($V(66) = 25.6$, $p = 4.9 \times 10^{-6}$, V-test for nonuniformity against 0°; Figure 3.6C).

In summary, we show that heading cells retain their tuning whether vestibular signals are modulated (in head rotation) or not modulated (in chamber rotation). Additionally, we show that the heading network in a head-fixed preparation as a whole exhibits the same functional properties as in freely moving animals. Together, these results show that modulation of vestibular input is not necessary for eliciting heading responses in RSC if vision and proprioception are spared. Rather, many of the same heading neurons remain active and accurately represent the animal's heading relative to the moving environment. Importantly, these results also show that the mammalian heading network is capable of representing the animal's heading relative to the environment even when the head is immobilized.

3.4.4 The ADN and visual cortex send distinct information to RSC

In our previous experiments, we found that not all cells would retain their preferred direction across conditions or coherently remap, suggesting that there is significant heterogeneity in RSC, which may be due to differences in the inputs it receives from other brain regions. Previous anatomical tracing studies [148, 150] have shown that RSC receives direct projections from both ADN and the visual cortex which likely contribute to RSC heading representations. However, the responses of these projections has not been studied in freely moving animals, and the information that each area sends to RSC is not known. To measure the responses from RSC-projecting neurons in each of these regions, we microinjected an AAV expressing GCaMP7b into ADN or the higher visual areas AM/PM in separate cohorts of wild-type mice. We chose AM and PM since they provide the major input from visual cortex to RSC [93] as well as their role in the visual hierarchy [52]. We then imaged the axon terminals arising from ADN ($n = 17$ recordings

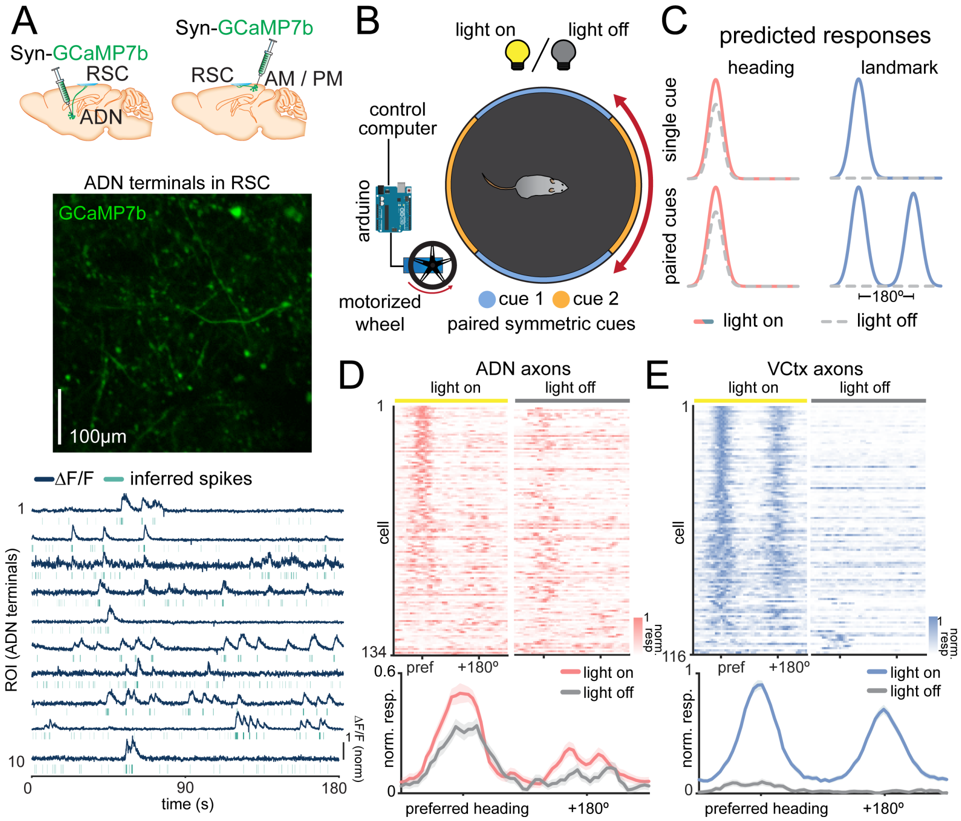

Figure 3.7: Imaging projections from ADN and visual cortex reveal distinctly tuned responses sent to RSC. **A)** *Top:* Example of injection sites in separate cohorts of mice. AAV-Syn-GCaMP7b was injected into either ADN or anteromedial (AM)/posteromedial (PM) of WT mice. *Middle:* Example imaging field in RSC of axon terminals originating from ADN. *Bottom:* Example $\Delta F/F$ traces and inferred spikes for imaged ADN terminals it RSC. **B)** Example schematic of experimental conditions. The single white cue card has been replaced with paired symmetric cues on the floating chamber, which is driven by a motorized wheel. Neurons from RSC are recorded across light-on and light-off phases. **C)** Schematic of expected axonal responses. *Left:* Axons terminals encoding heading independent of visual cues are expected to have unimodal tuning curves across both conditions that are not affected by the light condition. *Right:* Axons terminals responding to visual cues are expected to show a single peak in a single-cue condition, but dual peaks in the paired symmetric cue condition. In both cases, the responses will be reduced in the light-off condition. **D)** Responses of ADN axons across recordings. *Top:* Heat maps in the light-on (left) and light-off (right) condition. Each row represents the aligned response of a single axon, and axons are organized by similarity to a group mean in the light-on condition. *Bottom:* Averaged response across all ADN axons, showing an aligned unimodal peak in both light-on and light-off conditions. Traces shown are mean ± s.e.m.a **E)** Same as **D**, but for visual cortex axons. Averaged response shows a bimodal peak in the light-on condition, and no response in the light-off condition.

over 4 mice) or AM/PM in RSC ($n = 7$ recordings over 3 mice; Figure 3.7A). In order to distinguish classical visual responses from heading responses, we used a pair of symmetric cues on opposite sides of the chamber so that an identical visual stimulus would pass in front of the mouse twice for each full chamber rotation. We also recorded in both light-on and light-off conditions to selectively gate visual input (Figure 3.7B). We postulated that projections carrying heading signals would exhibit unimodal peaks that persist in the light-off condition, accurately representing heading regardless of light condition or cue symmetry. On the other hand, projections communicating visual landmark signals would exhibit a light-sensitive and bimodal tuning curve, with peaks separated by approximately 180° due to the symmetry of the visual stimulus (Figure 3.7C).

We found that responses from ADN and visual cortical projections exhibit distinct responses in these conditions. In the light-on condition, ADN axons show a unimodal tuning curve, whereas visual cortical axons show a bimodal tuning curve (Figure 3.7D, E). In the light-off condition, ADN axons maintain their response for several trials, whereas visual cortical axons lose their tuning. These results show that the information from the visual cortex is highly sensitive to environmental cues and cannot be entirely sufficient for driving heading responses, as any symmetrical environment would result in an inaccurate heading representation. The accurate internal heading representation regardless of environmental symmetry suggests that the information from the visual cortex must be processed prior to being integrated into the heading network. Together, these results indicate that ADN and visual cortex send distinctively tuned projections to RSC, which provide a basis for aligning the heading signal with external cues.

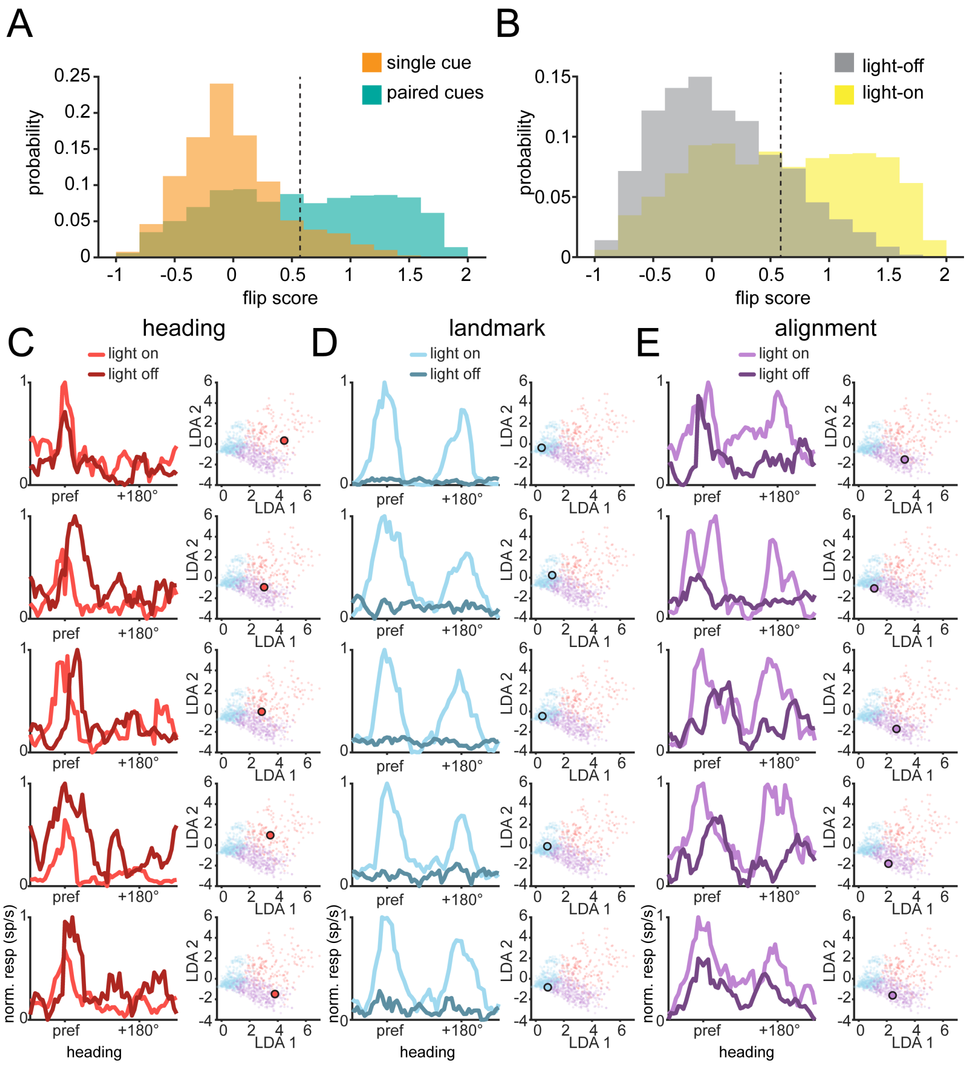

Figure 3.8: Neurons in the RSC have responses that cluster into three distinct profiles. **A)** Histogram of flip scores between the single cue experiments (orange, Figure 1) and paired cue experiments (green). **B)** Histogram of flip scores in the paired cue experiments comparing light-on (green) and light-off (gray) conditions. **C)** Example tuning curves for heading cells aligned by their preferred direction (pref), next to their position on the reduced dimensional space scatter plot. Each cell's position is shown with a large outlined dot. **D)** Same as **A**, but for landmark cells. **E)** Same as **A**, but for alignment cells.

3.4.5 A functional class of RSC neurons coregisters visual and heading signals

How do neurons in RSC combine the disparate responses from ADN and visual cortex? We imaged calcium activity in RSC cell bodies using the same experimental conditions, allowing us to determine whether RSC responses resemble thalamic or visual cortical inputs ($n = 36$ recordings over 6 mice). We found a diversity of responses in RSC that resembled both visual cortical inputs (discernible by a second peak in light) and ADN inputs (discernible by a single peak in the dark) (Figure 3.9A, Figure 3.8A-B). To help classify RSC responses, we fit a sum of Gaussians to the data then performed unsupervised clustering on the coefficients using a GMM to separate the cells into functional classes (Figure 3.9B; see Methods). We found that the data were optimally clustered into three functional classes (see Methods), although we note that the responses span a continuum rather than fully isolated clusters.

The model returned a prominent class of cells that mirrored the tuning curves of ADN axons, with a unimodal peak that is stable in either light-on or light-off conditions, which we call “heading cells” (Figure 3.9C). We also found another class that mirrored the tuning curves of visual cortical axons, with a bimodal peak in the light-on condition that disappears in the light-off condition, which we call “landmark cells” (Figure 3.9D). Finally, the clustering returned a third major class of cells, which combined the responses of ADN and visual axons, exhibiting bimodal responses in the light-on condition, but changing to a more unimodal response profile in the light-off condition, which we call “alignment cells” (Figure 3.9E). The light-off peak in these alignment cells was always at the same location as one of the two peaks in the light-on condition, suggesting that landmark and heading responses are precisely coregistered in the alignment cells. Of the total number of tuned cells (13%), landmark cells made up the plurality of cells (35%),

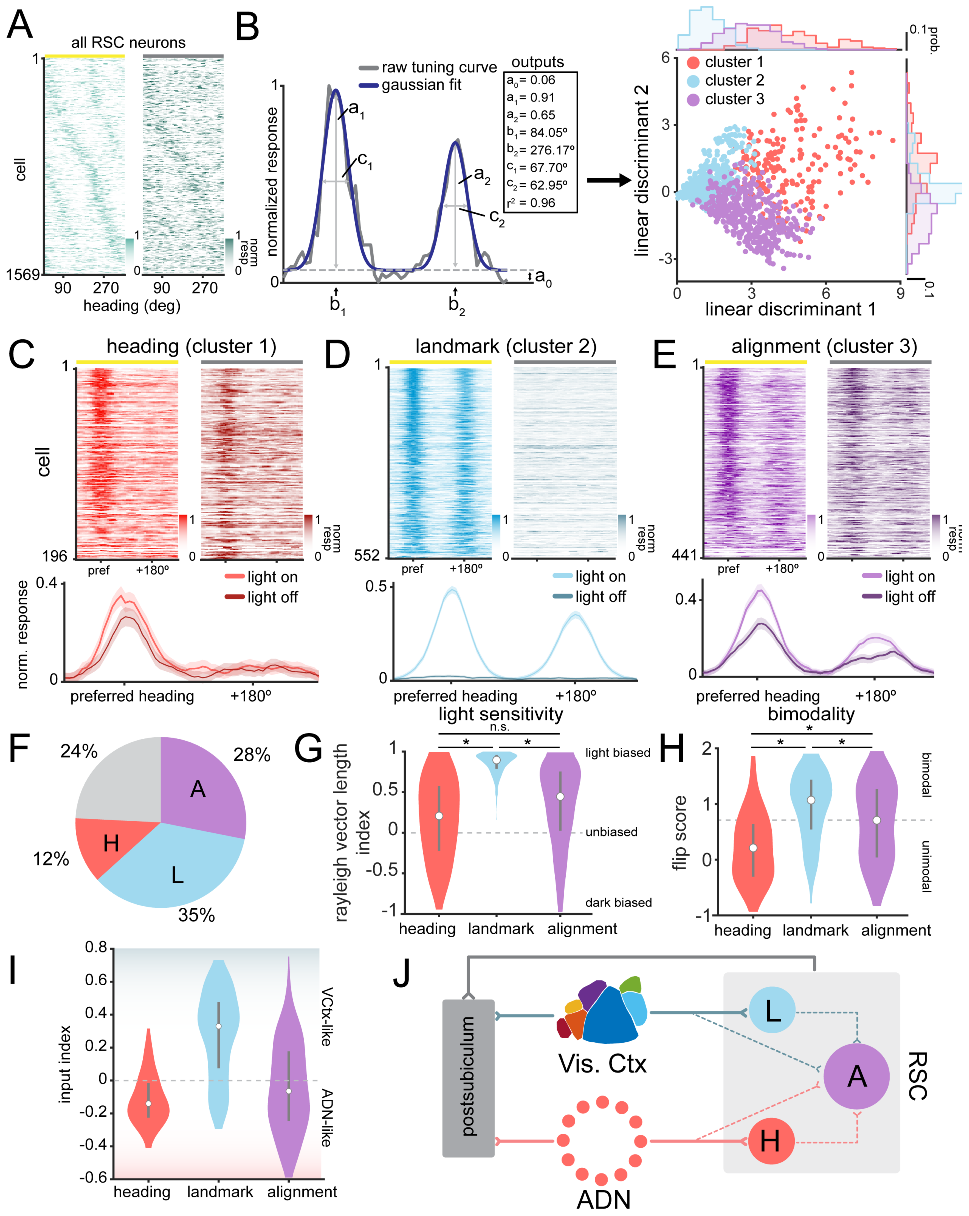

Figure 3.9: Unsupervised clustering of neural responses in the RSC reveals distinct functional classes. **A)** Heat maps of the responses of all somas imaged in RSC. **B)** *Left:* Example of a two-term Gaussian fit on an aligned and normalized tuning curve. *Right:* Scatter plot of clusters. **C)** *Top:* Heatmaps showing the aligned responses of the heading neurons. *Bottom:* Average responses of the neurons in the heading cluster. Traces are shown as mean ± s.e.m. **D)** Same as **C** for landmark neurons. **E)** Same as **C** for alignment neurons. **F)** Pie chart showing the proportion of cells in each cluster. **G)** Distributions of light sensitivity across cell types. **H)** Distributions of bimodality across cell types. **I)** Distributions of input index across cell types. **J)** Proposed model, dotted lines suggest putative projections. *: non-overlapping 95%CI. Center dot is the median and bars span from 25th to the 75th percentile.

followed by alignment (28%), and heading cells (12%) (Figure 3.9F, Figure 3.8). We then compared the cell classes in measures of light sensitivity and bimodality (Figure 3.9G, H). Across the classes, landmark cells showed significantly greater sensitivity to light condition (mean RVL index = 0.83, 95% CI = [0.81, 0.84]) than either alignment (mean RVL index = 0.25, 95% CI = [0.20, 0.30]) or heading cells (mean RVL index = 0.17, 95% CI = [0.10, 0.24]). Although alignment and landmark cells differed in their light sensitivity, alignment and heading cells did not, suggesting that alignment cells are robust to changes in light, like heading cells. On a measure of bimodality, landmark cells exhibited the highest flip scores due to their dual peaks (mean flip score = 0.82, 95% CI = [0.74, 0.89]), being significantly greater than both alignment (mean flip score = 0.56, 95% CI = [0.49, 0.63]) and heading cells (mean flip score = 0.19, 95% CI = [0.10, 0.28]).

Since ADN and visual cortex send tuned projections to RSC, we hypothesized that the somatic responses would be a result of specific combinations of tuned connections. To show this, we computed an input index that compares each RSC neuron's response to the average response from ADN and visual cortical axons (Figure 3.9I). Comparing across clusters shows the responses of heading cells are most similar to ADN axons while landmark cells are most similar to visual cortical axons. Alignment cells have widely distributed input indices, suggesting that they may receive information from both sources, or from intra-RSC projections. These results support the contention that projections from visual cortex and ADN synapse with specific targets in RSC, leading to a functional class of cells capable of coregistering visual cues and heading (Figure 3.9J).

3.4.6 Contributions of distinct classes to representation of heading

The functional classes observed would be expected to lead to very different representations of head direction. We sought to understand the contributions of each functional class to the population-level coding of heading. First, we confirmed that the heading network was able to accurately represent the animal's heading, even in an environment with symmetric visual information, by decoding heading from populations of cells within a single imaging frame. To combine multiple recordings, we created pseudopopulations of neurons by aligning trials across recordings and then randomly sampling a subset of these cells, determined by the number of cells in the smallest class (see Methods). Restricting decoding to subpopulations of cells within single imaging frames (of 100 ms duration) increased the dynamic range in decoder performance and allowed us to directly compare performance between classes. In the light-on condition, there is a systematic over-representation of 180° errors due to the symmetric visual cues. To prevent 180° decoding errors from biasing the performance metric, we opted to measure performance using "decoder accuracy", which is defined as the fraction of decoded headings that are within 18° of the actual heading in each time bin. When sampling across all the classes, the heading network shows remarkable accuracy, even in the presence of symmetric visual cues (mean decoder accuracy = 0.67, 95% CI = [0.59, 0.76], Figure 3.10A). When transitioning from light-on to light-off, there is a drop in the performance of the decoder, although the performance remains above chance, suggesting that the heading network continues to track heading, albeit less accurately, even in the absence of visual cues (mean decoder accuracy = 0.40, 95% CI = [0.33, 0.47], Figure 3.10A, bottom). In the transition from light-off to light-on, we found that the decoder rapidly recovered a high level of performance in the first trial following the transition (Figure 3.10B). These results confirm previous studies which have shown that the heading network gradually degrades in darkness, but is quickly restored in light [137, 47, 138].

To further parse the contributions of specific functional classes, we also performed population decoding restricted to cells of one response type (heading, landmark, alignment; Figure 3.9C-E). As with the entire pseudopopulation, we can examine the differences in decoder performance in light-on vs light-off conditions as well as the contribution of the symmetric visual cues, which manifests as increased 180° errors. We found that heading cells were able to accurately decode in both light-on (mean decoder accuracy = 0.43, 95% CI = [0.34, 0.50]) and light-off conditions (mean decoder accuracy = 0.35, 95% CI = [0.28, 0.41]), suggesting that they contribute to the heading signal in both conditions (Figure 3.10C). Because their decoder performance is lower than the population in the light-on condition, heading cells alone may be insufficient for optimally representing instantaneous heading. As expected based on their tuning curves, heading cells did not exhibit a preponderance of 180° errors (Figure 3.11), suggesting they do not represent visual information directly and were therefore not affected by the symmetric cues. In contrast, landmark cells have very high decoder performance in the light-on condition (mean decoder accuracy = 0.50, 95% CI = [0.41, 0.59]), with an over-representation of decoder errors at 180° (Figure 3.11), which immediately plummets to chance in the light-off condition (mean decoder accuracy = 0.22, 95% CI = [0.15, 0.29]; Figure 3.10D). This suggests that landmark cells strongly drive the heading signal when visual cues are present, but provide almost no contribution in their absence. Lastly, alignment cells show decoder performance that is between that of heading and landmark cells, taking advantage of improved decoding from the visual cues in the light-on condition (mean decoder accuracy = 0.45, 95% CI = [0.36, 0.54]), but retaining fairly accurate heading in the light-off condition (mean decoder accuracy = 0.40, 95% CI = [0.32, 0.49], Figure 3.10E). This suggests that alignment cells can take advantage of

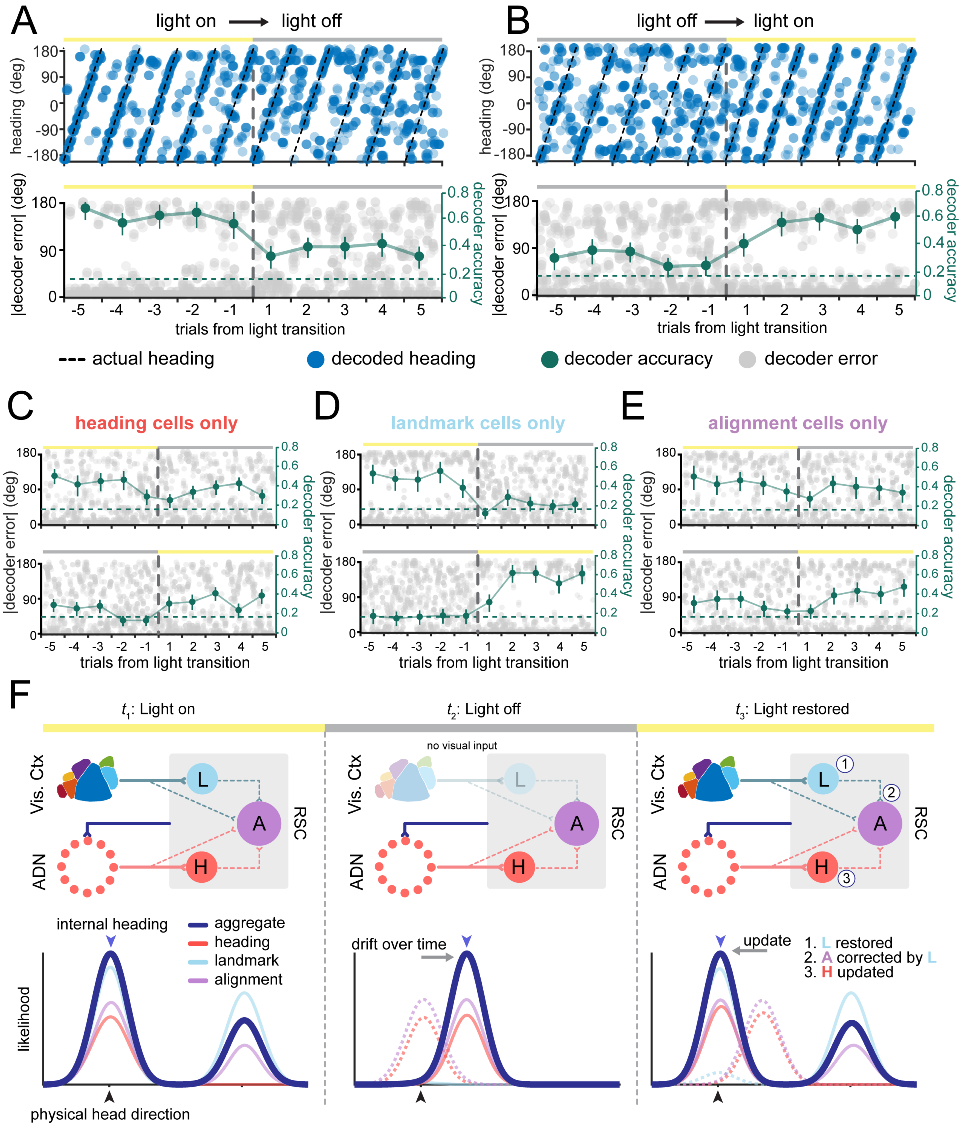

Figure 3.10: Decoding analysis shows independent contributions of each functional subclass to the overall heading representation in RSC. **A)** Pseudopopulation decoding of neural responses across trials. *Top:* Predicted heading (blue dots) overlaid on actual heading (black dotted line), transitioning from the light-on (yellow bar) to the light-off (gray bar) condition. *Bottom:* Decoder error (gray dots) and the average decoder accuracy for each trial (green dots and line)The dashed green line denotes chance level for decoder accuracy (0.18). Decoder accuracy is plotted as mean ± s.e.m. **B)** Same as **A**, but for light-off to light-on transition. **C)** *Top:* Decoder error (gray dots) and decoder accuracy (green dots and line) for decoder using only heading cells in light-on to light-off transition. *Bottom:* Same as top, but for light-off to light-on transition. **D)** Same as **C**, but for landmark cells only. **E)** Same as **C**, but for alignment cells only. **F)** Schematic of circuit for integration of visual information into the HD network.

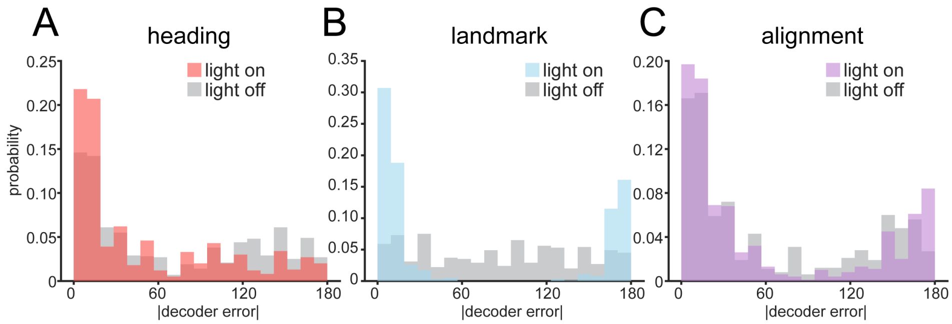

Figure 3.11: Histograms of decoder error reveal the preponderance of 180°errors in decoding landmark and alignment, but not heading, cells. **A)** Example histograms of decoder error in light-on and light-off conditions for heading cells only. **B)** Same as **A**, but for landmark cells. **C)** Same as **A**, but for alignment cells.

the visual cues in the light-on condition, while retaining accurate decoding in their absence in the light-off condition, positing that they may be responsible for integrating and registering visual landmark and heading information. Interestingly, decoding with sampling from the full population of heading cells outperformed any of the individual cell classes (Δdecoder accuracy$_{\text{all v. heading}} = 0.13 \pm 0.04$, Δdecoder accuracy$_{\text{all v. landmark}} = 0.33 \pm 0.04$, Δdecoder accuracy$_{\text{all v. alignment}} = 0.11 \pm 0.04$, mean ± bootstrapped s.e.m.), even with equal pseudopopulation sizes, suggesting that contributions from all three cell classes are important for an accurate internal heading.

Taken together, we propose a working model to describe the distinct roles played by heading, landmark, and alignment cells in the registration of heading representations to visual cues (Figure 3.10F). First, in the light-on condition, all three classes are active, with landmark cells faithfully representing the position of the visual cues, heading cells relaying information from the heading network, and a subset of alignment cells coregistering both sources of information, resulting in a internal heading that is well aligned with the true external heading. (Figure 3.10F, left). In the light-off condition, the landmark cells are silenced, leaving the heading cells as the primary driver of internal heading, and the alignment class exhibiting a response matched to the heading cells (Figure 3.10F, center). Moreover, the lack of anchoring visual information causes the heading network to drift over time, leading to the internal heading to become offset from the true heading. Upon restoring visual cues in the light-on condition, landmark cells regain their tuning, relaying this information to the appropriate subset of alignment cells, which are in turn updated (Figure 3.10F, right). The alignment cells then update the heading cells, and the broader network via feedback projections from RSC to the ADN, updating the heading representation throughout the heading system. We propose that the co-registration of visual landmark and heading signals in the alignment cells thereby plays a critical role in aligning the heading representation to external visual cues.

3.5 Discussion

One of the key findings of this paper is that heading, the relative orientation of an animal in an environment, can be encoded separately from physical head direction in the heading network. This finding is consistent with previous studies in which humans solve complex virtual navigation tasks without the requirement of physical movement, suggesting that they can create an abstract mental map of their direction independent of physical locomotion [175, 176, 177, 178]. Research in invertebrates further supports this view, as the E-PG ("compass") neurons of the *Drosophila* central complex, an analog of the heading network, is active in virtual environments even when the fly is immobile [114, 141, 115]. Here, we demonstrate for the first time that a neurons in the mammalian heading network show a similar capability during head immobilization, using multiple sensory inputs to accurately represent relative heading. Although previous experiments have examined the influence of nonvestibular sensory inputs on heading, they have uniformly allowed free angular rotation of the head [131, 130, 132, 133]. As compared to traditional head-fixed virtual reality set ups, our floating chamber designs confers several benefits. Beyond providing a three-dimensional visual environment, the floating chamber maintains somatosensory and proprioceptive cues present during locomotion through a physical environment. Using a combination of these sensory cues, the heading cells (many of which would be classified as HD cells in freely moving conditions) appear to be able to compensate for the absence of vestibular information, although not all neurons maintained their tuning between head rotation and chamber rotation conditions. Because of the heterogeneity of responses in RSC, a subset of RSC heading cells may be more strongly driven by vestibular input, and therefore lose their response during head fixation; whereas other, more visually driven, neurons are still responsive. This is reminiscent of previous studies which found that including additional sensory modalities improves the coding of AHV [160, 179] and HD [145] cells. However, our results show that, despite the reduced activity due to absence of vestibular input, neurons of the heading network in head-fixed mice remain functional and are able to accurately track heading, expanding the repertoire of experimental approaches.

The HD network has commonly been modeled as a ring attractor network, with heading represented by neurons as an ”activity bump” that can be shifted by sensory inputs. Along with the results presented here, other recent work has begun to elucidate the specific cells and mechanisms that may be responsible for anchoring the activity bump to visual landmarks. Jacob et al. found a specific class of cells that have bimodal tuning curves in a two-chamber symmetric environment, called ”within-compartment bidirectional cells”, that were postulated to develop their responses through Hebbian-based strengthening of visual information with information from the heading network [155, 154]. Similarly, LaChance et al. 2022 [180] found bidirectionally tuned cells in the postrhinal cortex that could represent and discriminate between symmetric visual cues, suggesting an important role in processing visual landmarks. Lastly, recent modeling work [181, 182] suggests mechanisms within the RSC that may be specifically responsible for anchoring heading to landmarks. However, there are some key differences in our findings. Previous work in RSC has found bimodal responses in two connected visually symmetric chambers, but not in a single chamber with symmetric cues [183]. In our recordings, we found cells in RSC with bimodal tuning curves in a single chamber with symmetric cues, akin to studies in postrhinal cortex [180]. We postulate that the difference in bimodal responses in RSC may be due to the mouse being fixed in the center, removing modulation of both vestibular signals and proximity-dependent visual cue size. Although our alignment cells may have some similar properties as the cells described above, we show that this subclass of cells changes from a bimodal to a coregistered unimodal tuning curve during the transition from light to darkness, suggesting that they are able to encode and align visual and heading signals.

Our results show that RSC integrates visual information into the heading network, but other areas in the HD cell network may also play important roles. The postsubiculum shares many of the same properties as RSC, as the only other area in the heading network receiving substantial monosynaptic input from both visual cortex and ADN [184, 185]. Lesioning postsubiculum degrades the heading signal in the ADN and results in an inability to register to visual landmarks, similar to RSC lesions [186]. Recent work has also suggested that the postrhinal cortex may also play a role, as it contains visually driven heading cells that can discriminate between visually symmetric landmarks [180]. Additionally, cells with bimodal responses have also been found in the medial entorhinal cortex [187], which has been show to affect RSC activity [188]. Given that cells in each of these areas exhibit similar visually-influenced tuning properties, are these systems redundant or complementary? Since the regions are highly interconnected [150, 189], it is possible that they may redundantly represent the same information, since registration of visual information is generally important for maintaining heading during spatial processing. Alternatively, the processing in each area may be complementary, biased by the strength of their connectivity with other brain regions [152]. For example, areas with input from primary visual cortex receive different signals than areas with input from higher visual areas. Further studies are necessary to understand how the distributed regions in the HD cell network interact during navigation.

In conclusion, our study provides evidence that neurons in the HD cell network are capable of representing the heading of the animal relative to the environment independent of physical head direction. The dysgranular RSC is able to combine multisensory information to create an abstracted map of heading, similar to how place cells can encode other variables besides position [190, 191, 192]. Finally, we propose a potential circuit based on a newly discovered class of neurons in RSC that act to coregister visual cues to the heading network. Future studies of how heading and other spatial signals are aligned to sensory input will be critical for understanding how internal representations of the spatial environment are generated, maintained, and updated by sensory information.

Chapter 4

Retinoic acid inhibitors mitigate vision loss in a mouse model of retinal degeneration

4.1 Preface

Because of our heavy dependence on vision as a primary sensory modality, diseases that impair or abolish vision are particularly deleterious. One class of diseases centers around the gradual degeneration of rod and cone photoreceptors in the retina, such as retinitis pigmentosa or age-related macular degeneration. While downstream neurons survive, they undergo physiological changes, including elevated spontaneous firing in retinal ganglion cells (RGCs). Recent evidence has shown that retinoic acid (RA) signaling is a molecular trigger of RGC hyperactivity, but whether this interferes with visual perception is unknown. Here, we show that treatments that target RA signaling improve behavioral image detection in vision-impaired mice. In vivo Ca^{2+} imaging shows that disulfiram sharpens orientation tuning of visual cortical neurons and strengthens fidelity of responses to natural scenes. These findings suggest that photoreceptor degeneration is not the only cause of vision loss in RP. RA-induced corruption of retinal information processing also degrades vision, pointing to RA synthesis and signaling inhibitors as potential therapeutic tools for improving sight in RP and other retinal degenerative disorders.

4.2 Introduction

Age-related macular degeneration (AMD) and retinitis pigmentosa (RP) are the most prevalent photoreceptor degenerative disorders, impairing vision or causing blindness in hundreds of millions of people worldwide [50, 51]. Both AMD and RP progress gradually, with retinal light responses and visual perception declining over years to decades. Despite the slow deterioration of rods and cones, most retinal ganglion cells (RGCs) survive and maintain synaptic connectivity with the brain until late stages in disease [193, 194, 195]. This has made RGCs a potential substrate for artificial vision restoration by optoelectronics [196, 197], optogenetics [198, 199], and optopharmacology [200, 201]. Because vision restoration technologies supplant light responses initiated by residual rods and cones, treatments based on these technologies are being deployed only in a small fraction of people with late-stage retinal degeneration. For patients whose vision is severely impaired but not yet eliminated, treatments for improving sight remain an unmet medical need.

Studies on mouse, rat, and rabbit models of RP show that, while downstream retinal neurons do survive, they nonetheless undergo morphological and physiological remodeling. Months after photoreceptors are lost, new dendritic branches begin to sprout from downstream neurons and their cell body positions start to change, mirroring remodeling events that occur over years to decades in advanced human RP [202, 203, 204, 205]. Much earlier, within days of photoreceptor loss, some RGCs become hyperactive, firing spontaneously at up to eight times their normal rates in healthy retinas [206, 207]. RGC hyperactivity results partly from changes in presynaptic neurons [208, 209] and partly from changes intrinsic to RGCs, including up-regulation of voltage-gated ion channels, which increases membrane excitability [210], and up-regulation of ligand-gated channels, which increases resting membrane permeability [201]. Recent studies indicate that retinoic acid (RA) is the signal that triggers morphological [211] and physiological [207, 212] remodeling. Adding exogenous RA to healthy retinas mimics remodeling, adding RA receptor (RAR) inhibitors to degenerated retinas suppresses remodeling, and increased RA-induced gene expression can be detected in degenerated retinas [207]. Local atrophy of photoreceptors, induced by subretinal implantation of a metallic chip, also caused elevation of RA-induced gene expression in corresponding RGCs, leading to local hyperactivity [213]. This suggests that RA-induced hyperactivity is a common sequel to photoreceptor loss, whether the underlying cause is hereditary, as in RP, or environmental, as in many cases of AMD.

The functional consequences of remodeling on information processing and visual perception have remained uncertain [214]. Heightened spontaneous RGC firing could mask responses triggered by residual photoreceptors, as has been observed in the rd10 mouse model of RP [207]. However, degeneration-induced hyperactivity [208] and hyperpermeability [201] apply only to Off-RGCs. Accelerated spontaneous firing in Off-RGCs is predicted to compress the dynamic range to light decrements that normally provoke firing and expand the dynamic range to light increments that normally suppress firing. How these seemingly opposite effects might affect higher-order information processing in the brain is unknown. The effects of hyperactivity on visual perception are also unclear. Genetically inhibiting RAR increased light avoidance behavior in vision-impaired rd10 mice [207], but whether this reflects improved visual acuity or enhanced photophobia is unknown.

There is circumstantial evidence that retinal hyperactivity also applies to humans with degenerative blindness [204, 214]. Patients with RP report persistent photopsia [215, 216] and they have a heightened threshold for perceiving phosphenes induced by electrical stimulation of the eye, consistent with interference from heightened spontaneous retinal activity [217]. However, without tools to suppress hyperactivity, it is impossible to differentiate the direct effects of photoreceptor signal loss from the indirect effects of increased RGC background firing (i.e., “noise”). Here, we have used a pharmacological approach to block RA signaling, giving us a way to discriminate the effects of decreased signal from increased noise. By investigating visual perception with behavioral experiments and higher-order neural processing with functional brain imaging, we show that RA-induced retinal hyperactivity is a major contributor to vision impairment in the rd10 mouse. Moreover, by inhibiting RA, we reveal a new therapeutic strategy for mitigating vision loss that may be applicable across a wide range of photoreceptor degenerative disorders, regardless of the underlying etiology.

4.3 Methods

4.3.1 Animals

C57BL/6J (WT) and rd10 (Pde6β-/- mutant) mice were purchased from the Jackson Laboratory (strain #000664 and #004297, respectively). All mice were kept in a 12:12 light/dark cycle room, except for experiments including dark rearing (see below). All animal procedures were approved by the Institutional Animal Care and User Committee at University of California (UC) Berkeley and UC Santa Barbara.

4.3.2 Chemicals and solutions

Dissections and ex vivo retinal assays (MEA and imaging) were performed in artificial cerebrospinal fluid (ACSF) containing 119 mM NaCl, 2.5 mM KCl, 1 mM KH2PO4, 1.3 mM MgCl2, 2.5 mM CaCl2, 26.2 mM NaHCO3, and 20 mM d-glucose. Disulfiram (tetraethylthiuram disulfide, C10H20N2S4) was purchased from Sigma-Aldrich (#86720) and formulated in mouse chow by Dyets Inc. (PA, USA) at a final concentration of 2 mg/kg. Food was refreshed every 4 to 5 days during treatment. BSM 493 was purchased from Tocris (#3509) and stored at -20° C in a final concentration of 5 µM in phosphate-buffered saline (PBS).

4.3.3 RAR reporter

To detect RAR-induced transcription, we used an AAV vector (Vigene Biosciences, Maryland, USA) that included a cytomegalovirus (CMV) promoter upstream to the coding sequence for the RFP ("mStrawberry"), followed by a polyadenylate tail and a stop sequence [207, 213]. A fragment containing three repetitions of the RARE sequence followed by the weak promoter SV40 was subcloned from pGL3-RARE-luciferase (Addgene, plasmid #13458), a gift of the Underhill Laboratory [218]. Last, a GFP sequence was subcloned downstream to SV40 for a final construct of AAV2-CMV-RFP-stop-RARE(x3)-SV40-GFP. The presence of inverted terminal repeat sequences was confirmed by enzymatic digestion.

4.3.4 Genetically encoded calcium indicator

To measure activity-dependent increases in intracellular Ca^{2+} resulting from spike activity, we used a commercially available AAV vector encoding the Ca^{2+} indicator GCaMP6s under the control of the CaMKIIa promoter (Addgene, #107790, AAV9-

CamKII-GCaMP6s-WPRE-SV40), which is expressed in excitatory neurons.

4.3.5 Intravitreal injections

Adult WT and rd10 mice (>P21) were intravitreally injected with drugs or virus. Before injection, animals were anesthetized with isoflurane (2%), and their pupils were dilated with tropicamide (1%) and phenylephrine (2.5%). Proparacaine (0.5%) was used as a topical analgesic. GenTeal was applied under a glass coverslip to keep the cornea lubricated. An incision was made through the sclera below the ora serrata with a 30 gauge needle. Solutions were injected into the vitreous with a blunt-ended 33 gauge Hamilton syringe or a 25- to 30-µm tip diameter glass pipette beveled at a 45° angle. After injection, the antibiotic tobramycin (0.3%) was applied to the eye. Injections of RAR reporter AAV2 were binocular, at a maximal volume of 1.5 µl, and using a titer of >1014 particles/µl. Injections of vehicle (PBS 1×) and BMS 493 (5 µM) were binocular or monocular (depending on the experiment), using a final volume of 1.0 µl. Final BMS 493 concentration was 500 nM, assuming a 1:10 dilution in the vitreous volume of the mouse (10 µl).

4.3.6 Retinal dissections

All dissections were performed in ACSF continuously gassed with 95% O2/5% CO2. Mice were euthanized using saturating levels of isoflurane gas followed by cervical dislocation. Mice were then enucleated, the cornea was excised from the eye, and the lens was removed. For live retinal imaging and MEA recordings, retinas were detached from the RPE and cut in quarters. Each retinal piece was mounted on nitrocellulose paper, RGCs facing up (imaging), or placed on top of the recording electrodes, RGCs facing down (MEA). Retinal pieces were kept at 34° to 35° C.

4.3.7 Cortical surgery

All surgeries were conducted with the mouse under isoflurane anesthesia (3.5% induction, 1.5 to 2.5% maintenance). Before incision, the scalp was infiltrated with lidocaine (5 mg/kg, subcutaneously) for analgesia. Meloxicam (2 mg/kg, subcutaneously) was administered preoperatively to reduce inflammation. Once anesthetized, the scalp overlying the dorsal skull was sanitized and removed. The periosteum was removed with a scalpel, and the skull was abraded with a drill burr to improve adhesion of dental acrylic. For mice in the disulfiram experiments, a single 4 mm craniotomy was made over the left visual cortex. For mice in the BMS 493 experiments, a 4 mm craniotomy was made over each bilateral visual cortex (centered at 4.0 mm posterior, 2.5 mm lateral to bregma on each side), leaving the dura intact. We used a motorized microinjector (Stoelting, 53311) to deliver 0.75 µl of virus AAV9-CamKII-GCaMP6s (titer = 1 × 1013 to 3 × 1013) to three to four injection sites within area V1 of the cerebral cortex. A cranial window was implanted over the craniotomy and sealed, first with a silicon elastomer (Kwik-Sil, World Precision Instruments) and then with a dental acrylic (C&B-Metabond, Parkell) mixed with black ink to reduce light transmission. The cranial windows were made of two rounded pieces of cover glass (Warner Instruments) bonded with an ultraviolet-cured optical adhesive (Norland, NOA61). The bottom cover glass (4 mm) fit tightly inside the craniotomy, while the top cover glass (5 mm) was bonded to the skull with the dental acrylic. A custom-designed stainless steel head plate (eMachineShop.com) was then affixed using dental acrylic. After surgery, mice were administered carprofen (5 to 10 mg/kg, orally) every day for 3 days to reduce inflammation. The full specifications and designs for head plate and head fixation hardware can be found on our institutional laboratory website (`https://labs.mcdb.ucsb.edu/goard/michael/content/resources`).

4.3.8 RAR reporter imaging assay

Live retinal pieces mounted on nitrocellulose paper were maintained under oxygenated ACSF perfusion at 34° C. A spinning disk confocal microscope (Olympus IX50) with a 40× water-submersible objective was used for fluorescence imaging to detect red or green fluorescence owing to RFP or GFP expression. Optical sections (1.5 µm thick) of the ganglion cell layer of the retina were compiled to generate Z-stacks. Z-stacks were flattened and analyzed with ImageJ [National Institutes of Health (NIH)]. Two to three fields of view were analyzed for each retinal piece, and individual regions of interest (ROIs) were drawn around every visible cell body, enabling measurement of mean gray value for both RFP and GFP fluorescence. The GFP/RFP ratio was calculated for each ROI and averaged across retinal pieces (individual data points) and mice (mean value).

4.3.9 Multielectrode array

Retinas were dissected and maintained in ACSF as described previously. Individual pieces of retina were placed ganglion cell layer down onto an array with 60 electrodes spaced 200 µm apart (1060-2-BC, Multi-Channel Systems). After mounting, each retinal piece was dark-adapted for 30 min under constant perfusion of 34° C oxygenated ACSF. Extracellular signals were digitized at 20 kHz and passed through a 200 Hz high-pass second-order Butterworth recursive filter. Spikes were extracted using a threshold voltage of 4 SD from the median background signal of each channel. Spikes were then aligned and clustered primarily in three-dimensional (3D) principal components space using the T-Distribution Expectation-Maximization (Offline Sorter, Plexon). Inclusion criteria for units included distinct depolarization and hyperpolarization phases, interspike interval histograms with peak values, and at least 50 contributing spikes. Exclusion criteria included multiple peaks, high noise, and low amplitude in channels with more than three detected units.

4.3.10 Electroretinogram

Photopic ERG responses were recorded in adult mice with the HMsERG LAB System (OcuScience) under isoflurane anesthesia (3.5% induction, 1.5 to 2.5% maintenance) at a stable rectal temperature of >35.8° C. The ground electrode was placed on the back above the tail, while reference electrodes were placed in the chick under the cheek (all subdermal). Mouse pupils were dilated with tropicamide (1%) and phenylephrine (2.5%). Proparacaine (0.5%) was used as a topical analgesic. To create and maintain contact between the lens containing the recording electrode and the cornea, a small drop of hypromellose was placed on the eye, and the lens was gently pressed against it. After recording, GenTeal was applied to both eyes, and mice were allowed to recover from anesthesia.

Photopic stimulation was performed inside a mini-ganzfeld stimulator including 10 min of light adaptation to background light at 300 $\mathrm{cd{\cdot}s/m^2}$, followed by 32 flashes (frequency = 2.0 Hz, duration = 20 ms) for eight different light intensities ranging from 0.1 to 25 $\mathrm{cd{\cdot}s/m^2}$. Responses were recorded over a period of 360 ms after each flash. Data were filtered at 50 kHz. The amplitude of the b-wave was measured from the peak of the first inward voltage deflection (a-wave) to the peak of the first outward voltage deflection and averaged across 32 flashes per intensity.

4.3.11 Cage design and manipulation

The automated behavioral cages were based on a design developed by E. Pugh [219] and custom-built by Lafayette Instrument (IN, USA). The cage includes three main components: (i) a unidirectional running wheel, orienting the mouse toward a computer display and a revolutions counter; (ii) a nose poke area with an infrared sensor, connected to a peristaltic pump triggering delivery of a water droplet reward; and (iii) a Raspberry Pi minicomputer and 1366 pixel by 768 pixel liquid crystal display (LCD) screens. Screens were calibrated to have the same brightness. Custom software linked image display with wheel running and reward availability. Cages were used in a dark room, and experiments were conducted throughout the night. The involvement of the animal handlers was minimal (introduction and retrieval), while protocol implementation and data acquisition were fully automated.

4.4 Behavioral experiment design and data

4.4.1 Analysis

Adult (>P35), male and female WT and rd10 mice, in littermate tandems, were used for these experiments. The cohort of rd10 mice used in disulfiram experiments (Fig. 4) was reared under 14:10 light/dark conditions. The cohort of rd10 mice used in BMS 493 experiments (Fig. 5) were dark-reared from <P10 to P55 to P65 (depending on training and testing) and under 14:10 light/dark conditions afterward. Mice were water-deprived for >9 hours ahead of each experiment. Mice learned the task through operant conditioning. Training and testing sessions were conducted for 12 hours (6 p.m. to 6 a.m.). During the habituation protocol, the visual stimulus (a full-contrast grating with a 0.51 cycle per degree frequency) associated with reward availability is continuous, and the mouse can poke and receive 10% sucrose water ad libitum. During training, running on the wheel gates the visual stimulus, displayed on the screen. This is paired with unlocking of the nose poke, enabling the mouse to obtain the reward. The reward availability period and the duration of pump activation are shortened during training sessions to increase response stringency. During testing, stimuli have the same total luminance, but the contrast is randomly chosen from nine different possible steps, including 0, 1, 2, 4, 8, 16, 32, 64, and 100%.

In all sessions, latency was defined as the elapsed time between onset of the visual stimulus to nose poke. The mean latency to the 100% contrast stimulus during the first contrast sensitivity test was used as a reference to assess performance in response to all other contrasts and for all subsequent tests. A successful response was defined as one with mean latency falling within the ±2 SD of the latency during the reference test. Exclusion criterion during training is as follows: if during session 3 success rate was <80% and/or mean latency was >4 s. Exclusion criterion during testing is as follows: if SD > 40% of the mean (SD/mean > 0.4). Initial analysis was performed with custom software to extract the data from text files and arrange responses by contrast steps in datasheets. Analysis of success rate was performed manually.

4.4.2 Visual stimuli

All visual stimuli were generated with a Windows PC using MATLAB and the Psychophysics toolbox [94]. Visual stimuli were presented on two LCD monitors that can display visual images to either eye independently. Each monitor (17.5 cm by 13 cm, 800 pixels by 600 pixels, 60 Hz refresh rate) was positioned symmetrically 5 cm from each eye at a 30° angle right of the midline, spanning 120° (azimuth) by 100° (elevation) of visual space. The monitors were located 3 cm above 0° elevation and tilted 20° downward. A nonreflective drape was placed over the inactive monitor to reduce reflections from the active monitor.

Orientation tuning was measured with drifting sine wave gratings (spatial frequency, 0.05 cycles/deg; temporal frequency, 2 Hz) presented in 1 of 12 directions, spanning from

0° to 330° in 30° increments. For a single repeat, each grating was presented once for 2 s with a luminance-matched 4 s intertrial gray screen between presentations. This was repeated for eight repetitions per session.

Natural scenes stimuli consisted of 900 frames from Touch of Evil (Orson Wells, Universal Pictures, 1958) presented at 30 frames/s, leading to a 30 s presentation time per repeat with a 5 s intertrial gray screen. The clip consists of a single continuous scene with no cuts, as has been previously described and is commonly used as a visual stimulus (`https://observatory.brain-map.org/visualcoding/stimulus/natural_movies`). Each presentation was repeated 30 times, with a 5 s intertrial gray screen.

4.4.3 Two-photon imaging

After >2 weeks of recovery from surgery, GCaMP6s fluorescence was imaged using a Prairie Investigator two-photon microscopy system with a resonant galvo-scanning module (Bruker). For fluorescence excitation, we used a Ti:sapphire laser (Mai-Tai eHP, Newport) with dispersion compensation (DeepSee, Newport) tuned to $\lambda = 920$ nm. For collection, we used GaAsP photomultiplier tubes (Hamamatsu). To achieve a wide field of view, we used a 16×/0.8 numerical aperture microscope objective (Nikon) at ×1 (850 µm by 850 µm) or ×2 (425 µm by 425 µm) magnification. Laser power ranged from 40 to 75 mW at the sample depending on GCaMP6s expression levels. Photobleaching was minimal (<1%/min) for all laser powers used. A custom stainless steel light blocker (eMachineShop.com) was mounted to the head plate and interlocked with a tube around the objective to prevent light from the visual stimulus monitor from reaching the photomultiplier tubes. During imaging experiments, the polypropylene tube supporting the mouse was suspended from the behavior platform with high-tension springs (Small Parts) to reduce movement artifacts.

4.4.4 Two-photon post-processing

Images were acquired using the Prairie View acquisition software and converted into TIF files. All subsequent analyses were performed in MATLAB (MathWorks) using a custom code (`https://labs.mcdb.ucsb.edu/goard/michael/content/resources`). First, images were corrected for X-Y movement by registration to a reference image (the pixel-wise mean of all frames) using 2D cross-correlation. To identify responsive neural somata, a pixel-wise activity map was calculated using a modified kurtosis measure. Neuron cell bodies were identified using local adaptive threshold and iterative segmentation. Automatically defined ROIs were then manually checked for proper segmentation in a graphical user interface (allowing comparison to raw fluorescence and activity map images). To ensure that the response of individual neurons was not due to local neuropil contamination of somatic signals, a corrected fluorescence measure was estimated according to:

$$F_{\mathrm{corrected}}(n) = F_{\mathrm{soma}}(n) - \alpha(F_{\mathrm{neuropil}}(n) - \overline{F}_{\mathrm{neuropil}}) \tag{4.1}$$

where F_{neuropil} was defined as the fluorescence in the region $< 30\mu$ m from the ROI border (excluding other ROIs) for frame n. $\overline{F}_{\mathrm{neuropil}}$ is $F_{neuropil}$ averaged over all frames. α was chosen from [01] to minimize the Pearson's correlation coefficient between $F_{\mathrm{corrected}}$ and F_{neuropil}. The $\Delta F/F$ for each neuron was then calculated as:

$$\Delta F/F = (F_{\mathrm{n}} - F_0)/F_0 \tag{4.2}$$

where F_n is the corrected fluorescence ($F_{corrected}$) for frame n and F_0 defined as the mode of the corrected fluorescence density distribution across the entire time series.

4.4.5 Blinding to experimental condition

For disulfiram experiments, disulfiram-containing chow or control chow of the same composition (Dyets Inc.) were given neutral codes by an investigator not involved in the study and administered to the mice with the experimenter blind to experimental condition. For BMS 493 experiments, vials of drug and vehicle were given neutral codes, and each solution was used for one eye. In both cases, the experimental condition was revealed only after the primary analysis was complete.

4.4.6 Orientation tuning

Neural responses to the orientation tuning stimulus were first separated into trials, each containing the response of the neuron across all tested queried orientations. For each neuron, we averaged the baseline-subtracted responses to each orientation, creating an orientation tuning curve for each trial. To calculate the OSI in a cross-validated manner, we first separated the orientation tuning curves into even and odd trials. We then aligned the even trials using the maximal response of the averaged odd trial for each neuron and vice versa, resulting in aligned responses. We then calculated the OSI from the averaged tuning curves for each neuron using the following equation

$$\mathrm{OSI} = \frac{R_{\mathrm{pref}} - R_{\mathrm{pref}\,+\pi}}{R_{\mathrm{pref}} + R_{\mathrm{pref}\,+\pi}} \tag{4.3}$$

where R_{pref} is the neuron's average response at its preferred orientation, defined by cross-validation on a different set of trials using the above procedure. Aligning the orientation tuning curves of the neurons using cross-validation provides a more accurate measurement of the orientation tuning of the neuron, as it prevents nonselective neurons from having high OSI values due to spurious neural activity.

4.4.7 Naturalistic movies reliability

Neural responses to the naturalistic movies were first separated into trials, with each trial containing the full response of the neuron to the entire presented movie. The reliability of each neuron to the naturalistic movie was calculated as follows

$$R_{\mathrm{c}} = \sum_{t=1}^{T} CC(r_{\mathrm{c,\ t}}, r_{\mathrm{c,\ [1,\ T]\ \neq\ t}})/T \tag{4.4}$$

where R is the reliability for cell c, t is the trial number from $[1, T]$, CC is the Pearson correlation coefficient, $r_{\mathrm{c,\ t}}$ is the response of cell c on trial t, and $r_{\mathrm{c,\ [1,\ T]\ \neq\ t}}$ is the average response of cell c on all trials excluding trial t. To separate neurons by reliability deciles, we independently calculated the decile cutoffs for each condition and then binned neurons into their respective deciles.

4.4.8 Naturalistic movies decoding analyses

To decode naturalistic movie responses from the population data, we first randomly selected neurons of a given pool size (pool sizes: 2, 4, 8, 16, 32, 64, 128, 256, or 512 neurons) from across all recordings. The neural responses to natural movies within that pool were then divided into even and odd trials. The average population activity across even trials was used to calculate a "template" population vector for each frame of the movie. We then estimated the movie frame (F_{Decoded}) from the population activity of each actual frame (F_{Actual}). To accomplish this, we calculated the population vector from the odd trials during F_{Actual} and compared to the template population vectors (even trials) for all of the frames. The frame with the smallest Euclidean distance between population vectors was chosen as the decoded frame (F_{Decoded}). This process was repeated for each frame (F_{Actual}) of the movie. For each pool size of neurons used, the entire procedure was iterated 1000 times, picking new neurons for each iteration. This resulted in a confusion matrix that describes the similarity of neural activity patterns for each frame between nonoverlapping trials. To assess decoder performance, we measured the percentage of decoded frames that fell within 10 frames of the actual frame (chance level = 7%).

4.4.9 Statistical analysis

For data shown in Figures 4.1, 4.2, 4.8, 4.9, and 4.10, we used gLMEMs to account for the individual differences between mice in our statistical analyses. The formula for these models is as follows

$$y = X\beta + Zb + \epsilon \tag{4.5}$$

where y is the response vector, X is the fixed-effects design matrix (denoting treatment condition), β is the fixed effects vector, Z is the random-effects design matrix (denoting different mice), b is the random effects vector, and ϵ is the observation error vector. After fitting the models for each experiment, we performed F tests on the appropriate contrasts to determine significance. For data presented in Figure 4.2 (D and H), significance between cumulative probabilities was tested using the Kolmogorov-Smirnov test. For data presented in Figure 4.4, 4.6, 4.7, 4.3, and 4.5, comparison between groups used nonparametric tests (Mann-Whitney U test for independent samples or Wilcoxon sign test for paired data), unless the data passed the normality test (Shapiro-Wilk) and could be analyzed with parametric tests (two-tailed t test).

4.5 Results

4.5.1 Inhibitors of RA synthesis or RA signal transduction reduce degeneration-induced gene expression in the retina of rd10 mice

We intervened at two different steps in the RA signaling pathway in an attempt to suppress or reverse degeneration-induced remodeling of RGCs in the rd10 mouse model of RP (Figure 4.1A). RA is a retinoid, derived from dietary retinol (vitamin A). Retinol is converted into retinaldehyde by retinol dehydrogenase, which is expressed in retinal pigment epithelium (RPE) cells and Müller glial cells [220, 221, 222]. 11-Cis retinaldehyde, the opsin chromophore for rod and cone phototransduction, can be regenerated after photoisomerization by enzymes of the visual cycle, which are also expressed in RPE and Müller glial cells. However, retinaldehyde can also be converted into RA by the enzyme retinaldehyde dehydrogenase (RALDH), which is expressed in choroid, RPE, and retina [223, 224]. RA crosses cell membranes and binds to RAR, a nuclear protein that heterodimerizes with the retinoid orphan receptor (RXR). The complex, in conjunction with other coactivator proteins, then binds to specific DNA sequences to enhance transcription of genes [225, 226, 227]. RAR and RXR are expressed in many cells, but because physiological changes intrinsic to RGCs can account for much of degeneration-induced hyperactivity [207], we focused specifically on RGCs.

To assess pharmacological inhibition of degeneration-induced gene expression, we used a reporter gene construct delivered to RGCs with an adeno-associated virus (AAV) vector (Figure 4.1B). The construct encodes red fluorescent protein (RFP), which is expressed constitutively in all virally transduced cells, and green fluorescent protein (GFP), which is expressed only upon RAR activation by RA [207, 213]. Because GFP expression

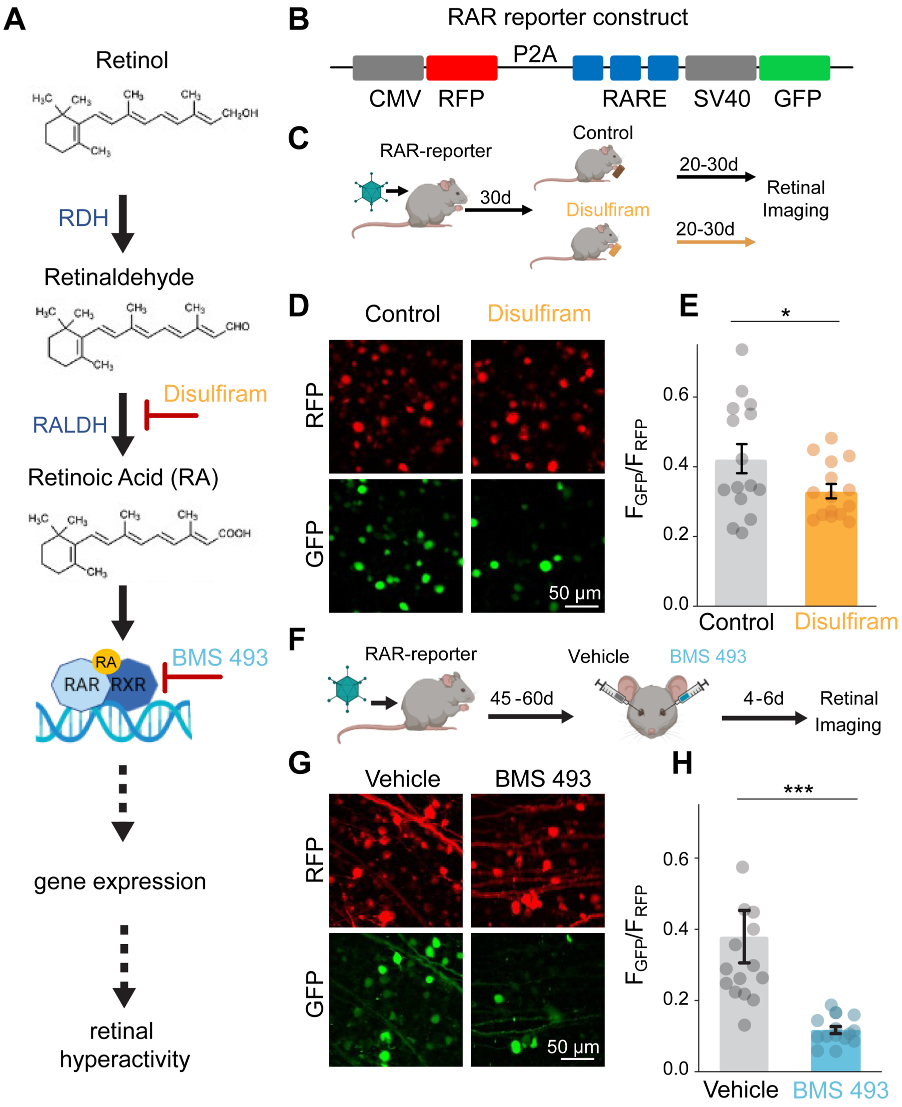

Figure 4.1: Disulfiram and BMS 493 reduce signaling through the RA pathway in the degenerated retina. **A)** RA signaling pathway. RDH, retinol dehydrogenase. **B)** Design of RAR reporter. CMV, cytomegalovirus promoter; RFP, red fluorescent protein; P2A, 2A self-cleaving peptide; RARE, RA response element; SV40, simian virus 40 promoter; GFP, green fluorescent protein. **C)** Design of disulfiram experiment. **D** Flattened Z-stacks of the ganglion cell layer showing cells expressing RFP and GFP. **E)** Quantification of RA-induced expression. The bar graph is mean ± SEM. Control: n = 733 cells from 15 retinal samples from 6 eyes in 3 mice; disulfiram: n = 535 cells from 15 retinal samples from 6 eyes in 3 mice. $F_{1,1266} = 12.51$, $^{***}p = 4.20 \times 10^{-4}$; two-tailed F test. **F)** Design of the BMS 493 experiment. **G)** Representative images for (F). **H)** Quantification of RA-induced gene expression similar to (E). Control: n = 385 cells from 15 retinal samples from 8 eyes from 4 mice; BMS 493: n = 448 cells from 15 retinal samples from 8 eyes from 4 mice. $F_{1,831} = 66.44$, $^{***}p = 1.32 \times 10^{-15}$; two-tailed F test.

reflects the level of RAR activation and RFP expression reflects the level of viral transduction that can vary between retinas, the GFP/RFP ratio can be used as a metric of degeneration-induced RA signaling [207]. Our first target for intervention was RALDH. RALDH is a member of a large family of enzymes known as aldehyde dehydrogenases (ALDHs). Disulfiram (Antabuse) is a Food and Drug Administration (FDA)–approved irreversible inhibitor of ALDHs [228], including all members of the RALDH subfamily [229]. Disulfiram is usually prescribed for chronic alcoholism and is taken orally. Ingested ethanol is converted into acetaldehyde, which is broken down by ALDHs. By preventing its breakdown, disulfiram allows buildup of acetaldehyde, discouraging alcohol consumption by causing severe hangover symptoms, known collectively as the disulfiram ethanol reaction. In the absence of alcohol use, treatment with disulfiram causes infrequent adverse reactions that resolve completely after stopping treatment [230].

To assess whether disulfiram can inhibit degeneration-dependent activation of the RA pathway, we injected the eyes of rd10 mice with the RAR reporter virus early in degeneration (Figure 4.1C). We continuously provided them with ad libitum regular food or food containing disulfiram (2 mg/kg) for 20 to 30 days and imaged their retinas later in degeneration (Figure 4.1D). RGCs in disulfiram-treated mice showed a GFP/RFP of 0.33 ± 0.02, significantly lower than control mice with a ratio of 0.42 ± 0.04 ($F_{1,1266} = 12.51$, $p = 4.20 \times 10^{-4}$; generalized linear mixed-effects model (gLMEM): fixed effect for treatment, random effects for mouse and retina grouped by mouse; Figure 4.1E). These findings establish that orally administered disulfiram can be absorbed in the gastrointestinal tract, cross the blood-retina barrier, and reach the retina at a concentration sufficient to suppress RA-induced gene expression.

Our second target for intervention was RAR. We used BMS 493, a high-affinity inverse agonist of all RAR isoforms [231]. We showed that BMS 493 increases the response of RGCs to photostimulation of residual rods and cones in rd10 mice [207], supporting our conclusion that RA, signaling through RAR, mediates degeneration-induced physiological remodeling.

To test whether BMS 493 can inhibit degeneration-dependent activation of the RA pathway, we injected rd10 mice with the RAR reporter virus early in degeneration (Figure 4.1F). In each mouse, we delivered BMS 493 in one eye and vehicle in the contralateral eye by intravitreal injections. Last, we imaged the retinas isolated from these mice (Figure 4.1G). RGCs in BMS 493–injected eyes had a mean GFP/RFP value of 0.12 ± 0.01, significantly lower than RGCs in vehicle-injected eyes with a ratio of 0.38 ± 0.07 ($F_{1,831} = 66.44$, $p = 1.32 \times 10^{-15}$; gLMEM: fixed effect for treatment, random effects for mouse and retina grouped by mouse; Figure 4.1H). These findings establish that delivery of BMS 493 through intravitreal injection suppresses RA-induced gene expression even more effectively than orally administered disulfiram.

4.5.2 Disulfiram and BMS 493 reduce RA-induced RGC hyperactivity without affecting residual photoreceptor function

We next asked whether inhibiting the RA pathway could suppress RGC hyperactivity in the rd10 retina. We used mice midway through the photoreceptor degeneration process (P40 to P45) when RGCs are already hyperactive [207, 232]. Oral disulfiram must cross several barriers to inhibit RA synthesis and subsequent downstream effects in the retina, so we assessed its effects on hyperactivity after 40 days of continuous treatment (Figure 4.2A), sufficient time to inhibit RA-induced gene expression (Figure 4.1E). Control littermates were given food without disulfiram for the same period.

After treatment, we isolated the retina and prepared flat-mounted samples for multielectrode array (MEA) recordings of spontaneous RGC activity. Recordings showed less spontaneous firing in darkness in samples from disulfiram-treated mice than from

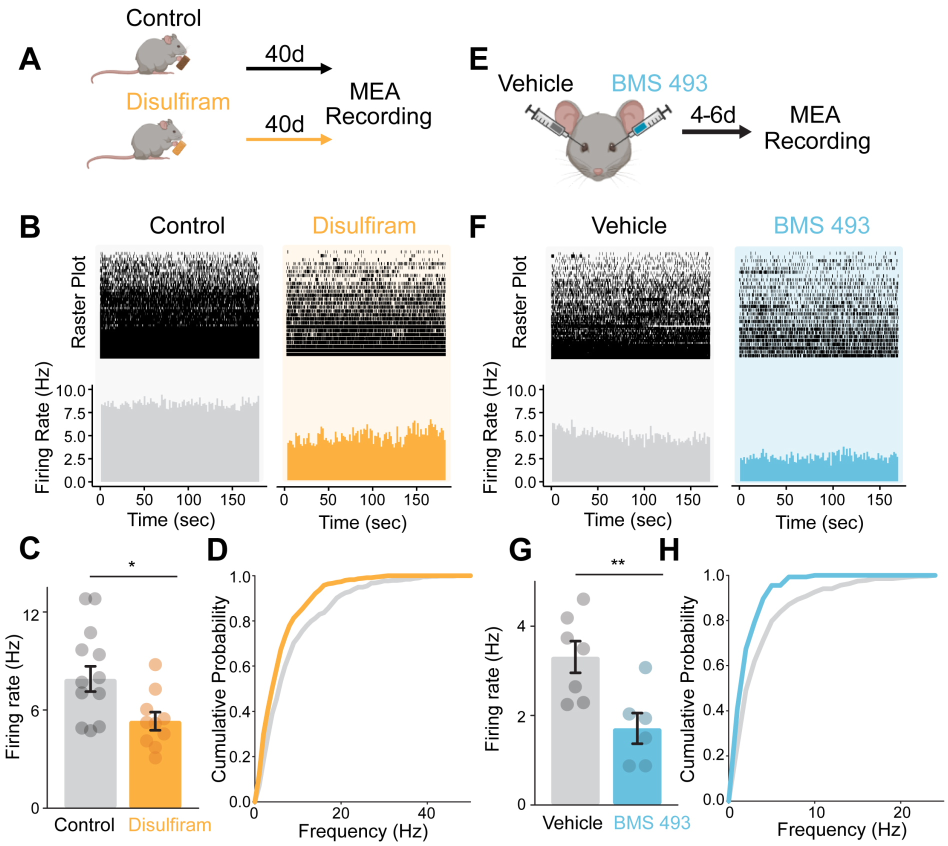

Figure 4.2: Disulfiram and BMS 493 reduce hyperactivity in the degenerating retina. **A)** Early-degeneration rd10 mice (P40 to P45) were given food with or without disulfiram (2 mg/kg) for 40 days. **B)** MEA recording from retinal samples (15 mm2 each) from control and disulfiram mice. Raster plots show spontaneous activity of individual units. Bottom: Mean firing rates across all units. **C)** Violin plots show mean firing frequency for every recorded unit. The bar graph shows means ± SEM. Control: n = 531 units from 11 retinal samples from eight eyes in four mice; disulfiram: n = 443 units from 10 retinal samples from six eyes in three mice. $F_{1,972} = 4.36$, $p = 0.037$; two-tailed F test. **D)** Cumulative probability of firing frequencies from control and disulfiram retinas as in (C). Disulfiram (orange) resulted in a leftward shift in the curve, indicating reduced firing across all units ($***p = 1.75 \times 10^{-5}$, Kolmogorov-Smirnov test). **E)** Early-degeneration rd10 mice (P40 to P45) were injected intravitreally with 1 µl of vehicle (PBS ×1) in one eye and 1 µl of BMS 493 (5 µM) in the other eye. At 4 to 6 days after injection, retinas were obtained for MEA recording as in (A). **F)** Retinal MEA recordings from vehicle- and contralateral BMS 493–injected eyes from one mouse. **G)** Firing frequencies similar to (C). Vehicle: n = 271 units from seven retinal samples; BMS 493: n = 135 units from six retinal samples; from a total of six eyes in three mice. $F_{14,404} = 20.87$, $***p = 6.53 \times 10^{-6}$; two-tailed F test. **H)** Analysis of spontaneous activity, similar to (D). Cumulative probability plot as in (G). The left shift in the BMS 493 curve (light blue) is statistically significant ($*\ p = 0.001$, Kolmogorov-Smirnov test).

control mice (Figure 4.2B). Overall, mean firing frequency across all units was 5.34 ± 0.54 Hz with disulfiram, significantly less than 7.90 ± 0.78 Hz for control ($F_{1,972} = 4.36$, $p = 0.037$; gLMEM: fixed effect for treatment, random effects for mouse and retina grouped by mouse; Figure 4.2C). Cumulative probability analysis shows that disulfiram scales down firing in highly active units ($p = 1.75 \times 10^{-5}$, Kolmogorov-Smirnov test; Figure 4.2D). In disulfiram-treated retinas, we detected a mean value of 44.3 spontaneously active units per retinal sample, as compared to 51.6 active units in control retinas, a reduction of 14.2%.

Next, we assessed BMS 493 (Figure 4.2, E to H). One eye of each mouse was injected with BMS 493 and the contralateral eye with vehicle, allowing intra-animal comparisons (similar to Figure 4.1F). We again used mid-degeneration rd10 mice (P40 to P45), but because the drug was injected directly into the eye and administered only once, inhibition of RA signaling begins much more quickly and is more transient. Therefore, recordings were obtained much earlier in the life of the mice, at 4 to 6 days after injection (P45 to P50) (Figure 4.2E). This is long enough to substantially inhibit RA-induced gene expression (Figure 4.1H), but at a younger total age than in the disulfiram experiments, accounting for the lower-baseline firing rate (compare Figure 4.2, B versus F).

Retinas obtained from eyes injected with BMS 493 showed less spontaneous activity than retinas from contralateral eyes injected with vehicle (Figure 4.2F). The mean firing rate of BMS 493–treated retinas was 1.71 ± 0.34 Hz, significantly lower than in vehicle-injected retinas of 3.31 ± 0.35 Hz ($F_{1,404} = 20.87$, $p = 6.53 \times 10^{-6}$; gLMEM: fixed effect for treatment, random effects for mouse and retina grouped by mouse; Figure 4.2G). Cumulative probability analysis of all units shows that similar to disulfiram, BMS 493 decreased the probability of encountering high–firing frequency RGCs $p = 0.001$, Kolmogorov-Smirnov test; Figure 4.2H). In BMS 493–treated retinas, the mean number of spontaneously active units per retinal sample was 22.5, while the same value was 38.7

in the vehicle-injected counterpart eye of the same mouse, a decrease of 41.9%.

RAR expression is abundant in the outer retina, particularly in cone photoreceptors [233]. Hence, it seemed possible that disulfiram and BMS 493 might affect events in the outer retina, independent of their effect on RGCs. To address this possibility, we recorded the photopic electroretinogram (ERG) in rd10 mice [234]. We focused on the b-wave, which reflects light-modulated synaptic transmission primarily from cones to bipolar cells, because the rods are largely degenerated at this age (P60 to P80). We found that neither disulfiram (Figure 4.3, A and B) nor BMS 493 (Figure 4.3, C to E) caused a significant change in the amplitude of the b-wave across a range of photopic intensities. These results suggest that inhibiting RA does not affect events in the outer retina, leaving events in the inner retina as the primary mechanism of RA-induced hyperactivity.

4.5.3 Disulfiram and BMS 493 enhance behavioral detection of images in rd10 mice

Genetically interfering with RA signaling augments light avoidance behavior in rd10 mice [207], but whether inhibiting RA signaling can improve image-forming vision has remained unknown. To investigate this, we used a contrast sensitivity test involving operant conditioning, inspired by a previous paradigm for measuring visual threshold [219]. We used a behavioral cage outfitted with a unidirectional running wheel, orienting the mouse toward a computer display (Figure 4.4A). The cage also has a nose poke sensor, which, when engaged, triggers delivery of a water droplet reward (10% sucrose). Running on the wheel digitally gates the onset of a full-contrast grating displayed on the screen, while simultaneously unlocking the nose poke. Mice are water- and food-deprived before each session, providing motivation for finding the association between the visual stimulus and availability of reward. The period of reward availability was shortened

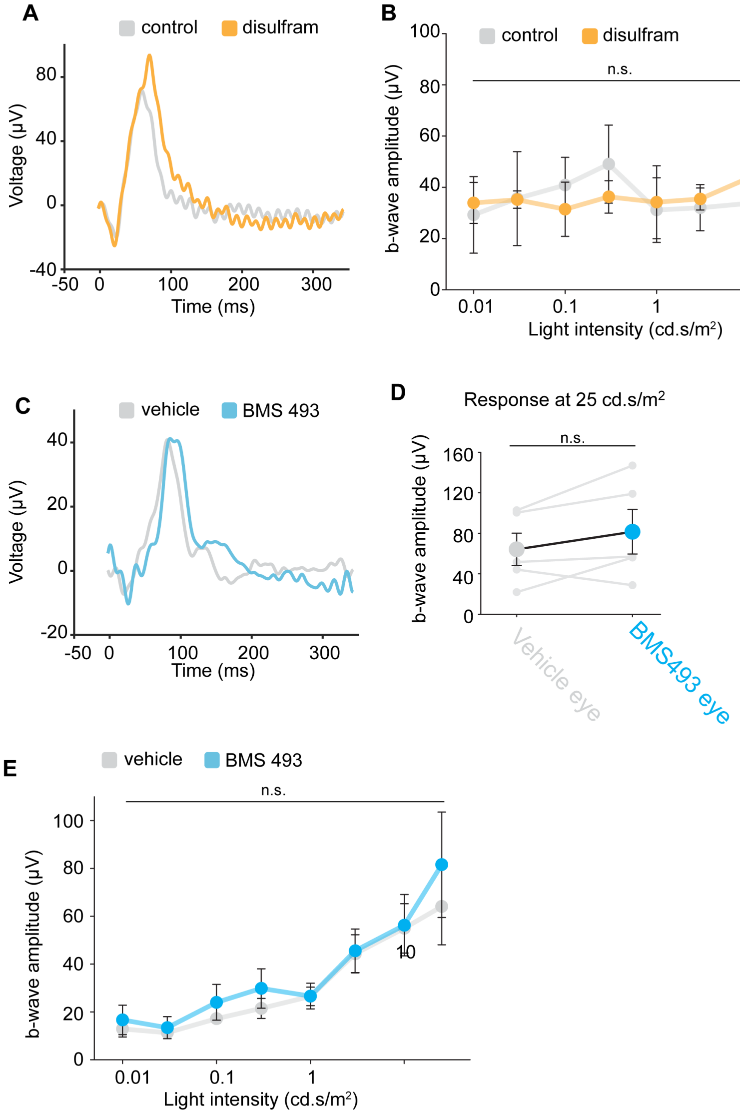

Figure 4.3: The ERG b-wave is unchanged by treatment with disulfiram or BMS 493. **A)** Electroretinogram (ERG) recordings of P80-90 rd10 mice treated for 40 days with disulfiram (orange) vs control (grey). **B)** Intensity-response curves. Recordings were obtained from 3 control mice (6 eyes) and 4 disulfiram mice (8 eyes) and are shown as mean ± SEM. n.s. - non-significant difference, p>0.05, 2-tailed t-test. **C)** ERG recordings 4-6 days after injecting vehicle (PBS ×1, grey) into one eye and BMS 493 (blue) into the contralateral eye. **D)** Responses from BMS 493-injected and vehicle-injected eyes in all 5 mice tested. **E)** Intensity-response curves showing no significant effect of BMS 493. Recordings were obtained from 5 mice (10 eyes), one eye injected with BMS 493 and the contralateral eye with vehicle. n.s. non-significant difference, p>0.05, 2-tailed paired t-test.

during three successive training sessions to increase response stringency (Figure 4.4B). Only those mice achieving a criterion level of success during training (>80% of trials with a response latency of <4 s) with 100% contrast were carried forward for subsequent testing of contrast sensitivity. This involved randomly varying the image contrast over nine distinct values over the course of a testing session (Figure 4.4C). All images were equiluminant irrespective of contrast, and monitors across different cages were calibrated for uniform brightness (see Methods).

Figure 4.4 (D to F) exemplifies the behavioral responses of an individual wild-type (WT) mouse during training and testing. During training, the mouse learns to associate the full-contrast image with the availability of reward (Figure 4.4D). At the beginning of training session 2, response latencies were prolonged and inconsistent, but by the end, responses occurred within 2 to 3 s of stimulus presentation. The response latency remained at 2 to 3 s during training session 3 when the reward availability period was reduced (Figure 4.4E), further reinforcing the association.

We tested contrast sensitivity on a mouse that had achieved the criterion level of success during training. We presented stimulus images at different contrasts, randomized from trial to trial. Low-contrast images elicited responses with longer and more variable latencies than high-contrast images (Figure 4.4F). The mean latency of five WT mice subjected to the contrast sensitivity test is gradually reduced from 8 s at 1% contrast to 2 s at 100% contrast (Figure 4.4G). The mean latency at 100% contrast was used to set the range of responses considered as successful ones for all other contrasts and subsequent tests (Figure 4.4F, "Test 100% contrast"). A nose poke was considered successful if it happened at a time range of -2 SD to +2 SD of the mean (a mouse with a response SD $\geq$ 40% of the mean was excluded from analysis; see Methods). Success rate was then used to generate a full contrast sensitivity curve (Figure 4.4H). To test the possibility that mice might fail the test because of behavioral extinction, we tested the same five mice 40

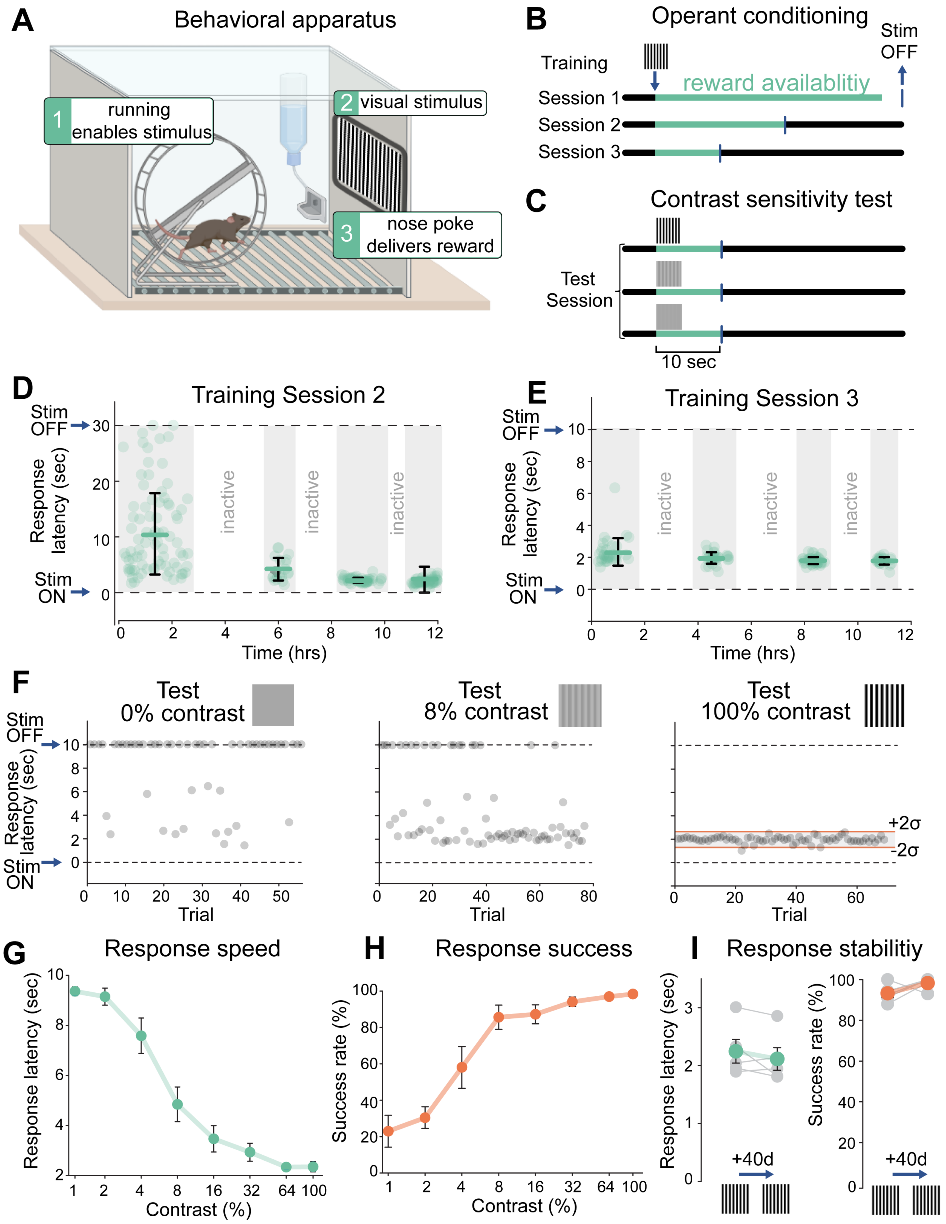

Figure 4.4: Measuring behavioral image detection in mice. **A)** Apparatus for operant conditioned image detection. **B)** Training to 100% contrast images occurs over three sessions (each 12 hours) with decreasing reward intervals, shaping response latency. **C)** Test condition. **D) to F)** Responses of an individual wild-type (WT) mouse during training sessions 2 (D) and 3 (E) and to three different contrasts (0, 8, and 100%) during contrast sensitivity test (F). **G)** Grouped data showing full contrast sensitivity curve. (n = 5 WT mice, P60). **H)** Same as (G), but for success rate. **I)** Comparison of response speed and success rate in the same group of WT mice at P60 versus P100. Individual data for each mouse are shown in gray; mean ± SEM values are shown in green (latency) and red (success rate), respectively. $P > 0.05$, Wilcoxon rank sum test.

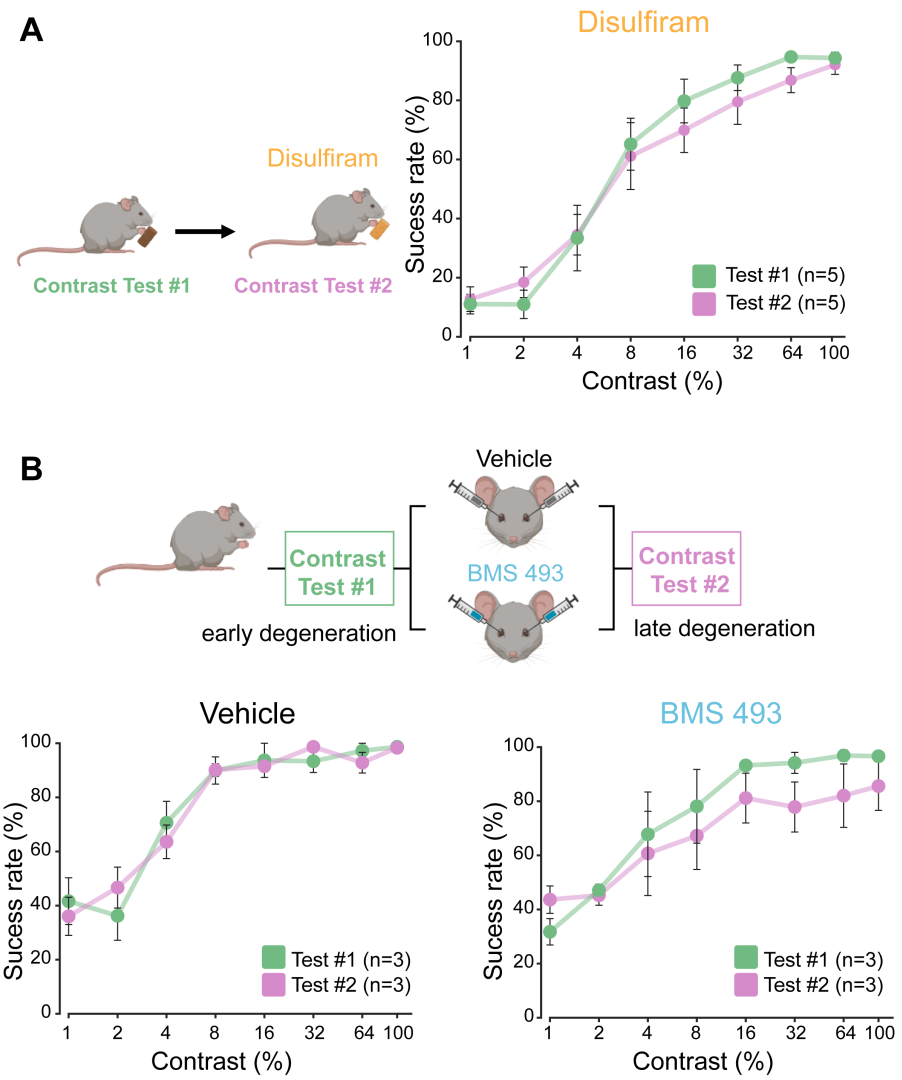

Figure 4.5: Testing disulfiram and BMS 493 in wild-type mice with normal vision. **A)** Left: experimental design. Mice were fed a regular diet without disulfiram and tested for contrast sensitivity (test #1), after which their food was switched to that containing disulfiram (2 mg/Kg) for 40 days. At P100 they were tested for the second time (test #2). Right: success rate for each contrast tested before (green) and after (pink) disulfiram treatment. **B)** Similar to A, above. Mice were trained and tested at P60, and then injected intravitreally in both eyes with 1 µl of vehicle (PBS x1) or BMS 493 (5 µM). At 4-6 days postinjection, they were tested for a second time.

days apart with no "refresher" training session in between (Figure 4.4I). We found that their response latency and success rate did not differ in the second test from the first, demonstrating that, once they learn, mice are able to retain this visually guided operant conditioning for long periods of time.

Next, we carried out the same procedure to quantify the effects of disulfiram on contrast sensitivity. Mice younger than P35 run on the wheel infrequently and are poor learners of this task. Therefore, we started training at P35 to P40, when some photoreceptor degeneration had already begun (Figure 4.6A) but early enough to ensure consistent short-latency responses to the 100% contrast image (Figure 4.6, B and C, left). All mice were first trained and tested in the absence of any pharmacological manipulation and were randomly assigned to treatment or control groups ahead of the second test.

Figure 4B shows the behavior of a trained rd10 mouse early (test #1) and late (test #2) in degeneration. Without drug treatment, short-latency responses disappeared nearly completely because of vision loss. However, in a mouse receiving disulfiram, short-latency responses were retained (Figure 4.6C). Group data from early degeneration rd10 mice show the already impaired contrast sensitivity caused by partial death of photoreceptors (compare Figure 4.6D to Figure 4.4H). After test #1 was complete, mice were randomly assigned to the control or disulfiram group, but retrospective analysis of their performance in test #1 showed similar contrast sensitivity ($p > 0.05$, Mann-Whitney test). However, when tested for the second time 40 days later, mice fed with disulfiram-containing food (2 mg/kg) performed significantly better than control when reacting to high-contrast images (64 and 100% contrast; $p = 0.005$ and $p = 0.002$, respectively, Mann-Whitney test). As expected, experiments on WT mice showed no significant effect of disulfiram on behavioral contrast sensitivity (Figure 4.5A), consistent with disulfiram acting specifically by inhibiting RA synthesis.

A similar series of tests were conducted to assess the efficacy of BMS 493 in boosting

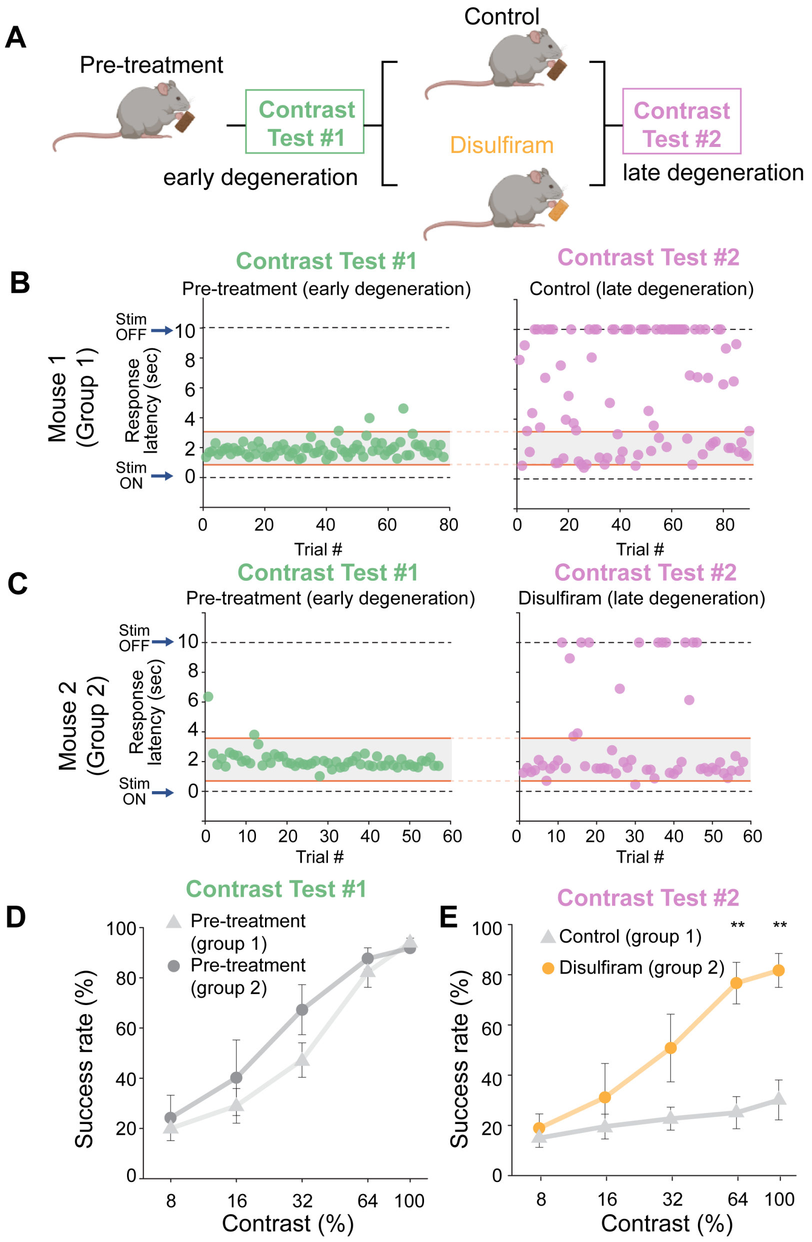

Figure 4.6: Disulfiram, a RALDH inhibitor, improves visual contrast sensitivity in rd10 mice. **A)** Experimental design. Rd10 mice were trained and tested at P35 to P40 (test #1), randomly separated into control or disulfiram groups, and tested again 40 days later at P75 to P80 (test #2). **B) and C)** Responses of individual mice in the control (B) and disulfiram (C) groups. **D)** Results of 13 mice on test #1. Success rate is plotted as a function of contrast; values are shown as means ± SEM. Retrospective analysis of mice for test #1, according to condition in test #2, found no significant differences $p > 0.05$ for all contrasts, Mann-Whitney test). **E)** Contrast sensitivity curve obtained later in degeneration and following 40 days of treatment with disulfiram or no treatment in control mice. $^{*}\ p < 0.01$ (for 64% contrast, $p = 0.005$; for 100% contrast, $p = 0.002$), Mann-Whitney test.

contrast sensitivity in degenerative rd10 mice (Figure 4.7A). Similar to experiments with disulfiram (Figure 4.6), rd10 mice were trained and tested and then randomly assigned for binocular intravitreal injections of BMS 493 or vehicle. An individual rd10 mouse receiving intravitreal BMS 493 showed more short-latency responses than an age-matched rd10 mouse injected with vehicle (Figure 4.7, B and C). Contrast sensitivity curves show that BMS 493 treatment preserved short-latency responses to 100% contrast stimuli (Figure 4.7, D and E), while almost none of these responses were seen in vehicle-treated mice $p = 0.041$, Mann-Whitney test). Control experiments on WT mice showed no augmentation of vision after BMS 493 treatment (Figure 4.5B). This is consistent with our previous studies showing little or no ongoing RA-induced gene expression in healthy retinas of WT mice [207], supporting the conclusion that BMS 493 improves vision specifically by blocking RAR. Together, these findings indicate that behavioral vision loss can be alleviated by inhibiting the RA pathway, consistent with RA-induced remodeling, making a major contribution to corrupting vision in retinal degenerative disorders.

4.5.4 Inhibiting the RA pathway sharpens the tuning of cortical neurons to complex visual stimuli

Behavioral evaluation of image-forming vision in mice requires days of training and testing, but physiological evaluation of neuronal responses can be characterized rapidly, without behavioral training, through functional Ca^{2+} imaging. Ca^{2+} imaging has the additional advantage of providing responses from many neurons simultaneously. Responses to a wide range of visual stimuli, from bars of specific orientation to movies with complex naturalistic scenes, can be elicited in a single session. Cortical imaging can provide a more thorough description of how photoreceptor degeneration degrades visual function and how the RA pathway inhibitors disulfiram and BMS 493 might alleviate vision

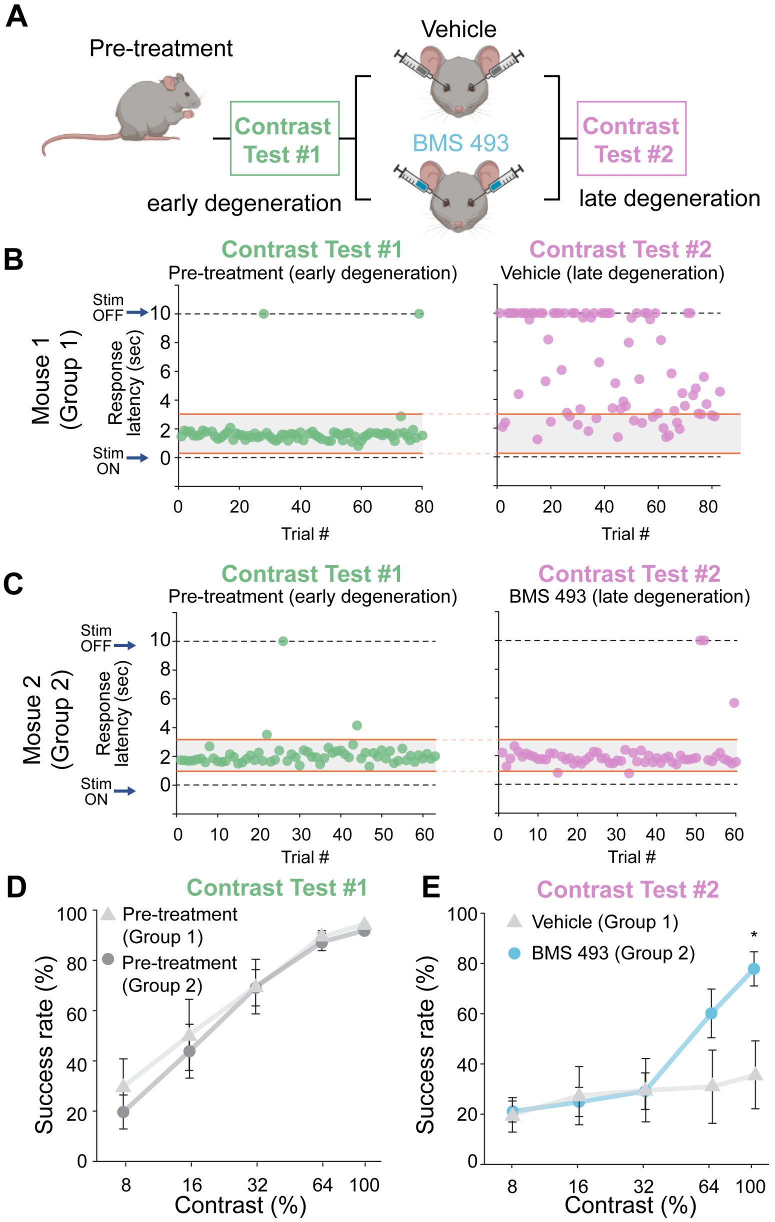

Figure 4.7: BMS 493, an RAR inhibitor, improves visual contrast sensitivity in rd10 mice. **A)** Experimental design. **B) and C)** Responses of individual mice in the vehicle (B) and BMS 493 (C) groups. **D)** Results of 12 mice before administration of drug during test #1. Success rate is plotted as a function of contrast; values are shown as means ± SEM. Retrospective analysis of mice for test #1, according to condition in test #2, found no significant differences $p > 0.05$ for all contrasts, Mann-Whitney test). **E)** Contrast sensitivity curve obtained later in degeneration and following treatment with vehicle or BMS 493. $p = 0.041$, Mann-Whitney test.

impairment.

To test the effect of disulfiram, rd10 mice were given a diet with or without the drug for 28 days, beginning early in the process of degeneration and ending late, after visual function was severely impaired (Figure 4.8A). Midway through the treatment period, we performed a surgical procedure (a hemicraniectomy) under anesthesia to facilitate intracortical injection of an AAV encoding the Ca^{2+} indicator GCaMP6s, which included the Ca^{2+}/calmodulin-dependent protein kinase II (CaMKII) promoter to target expression to excitatory neurons (see Methods). Following injection, we inserted a glass cranial window to provide optical access for subsequent imaging of GCaMP6s expressing neurons at the end of the treatment period. Imaging data were collected blind to treatment conditions.

Many excitatory neurons in the primary visual cortex respond selectively to stimuli of a particular orientation [6]. To determine whether disulfiram treatment influences orientation tuning, we measured responses to drifting periodic gratings presented to the eye contralateral to the cranial window (Figure 4.8, B and C). We found that a lower percentage of neurons were orientation-tuned in rd10 mice (16.06%) than typically observed in WT mice using a similar approach (30% in [235]), but the fraction tuned was significantly increased with disulfiram treatment (22.69%). In addition, disulfiram treatment caused significantly stronger orientation tuning as compared to control ($F_{1,1127} = 4.77$, $p = 0.029$; gLMEM: fixed effect for treatment, random effect for mouse; see Methods; Figure 4.8, D and E). This was quantified with a cross-validated orientation selectivity index (OSI) measure that compares the magnitude of response to preferred versus nonpreferred orientations, where the preferred orientation is determined using a separate subset of trials to eliminate spurious orientation tuning due to bursts of activity (see Methods).

We next asked whether inhibiting the RA pathway can improve the detection of

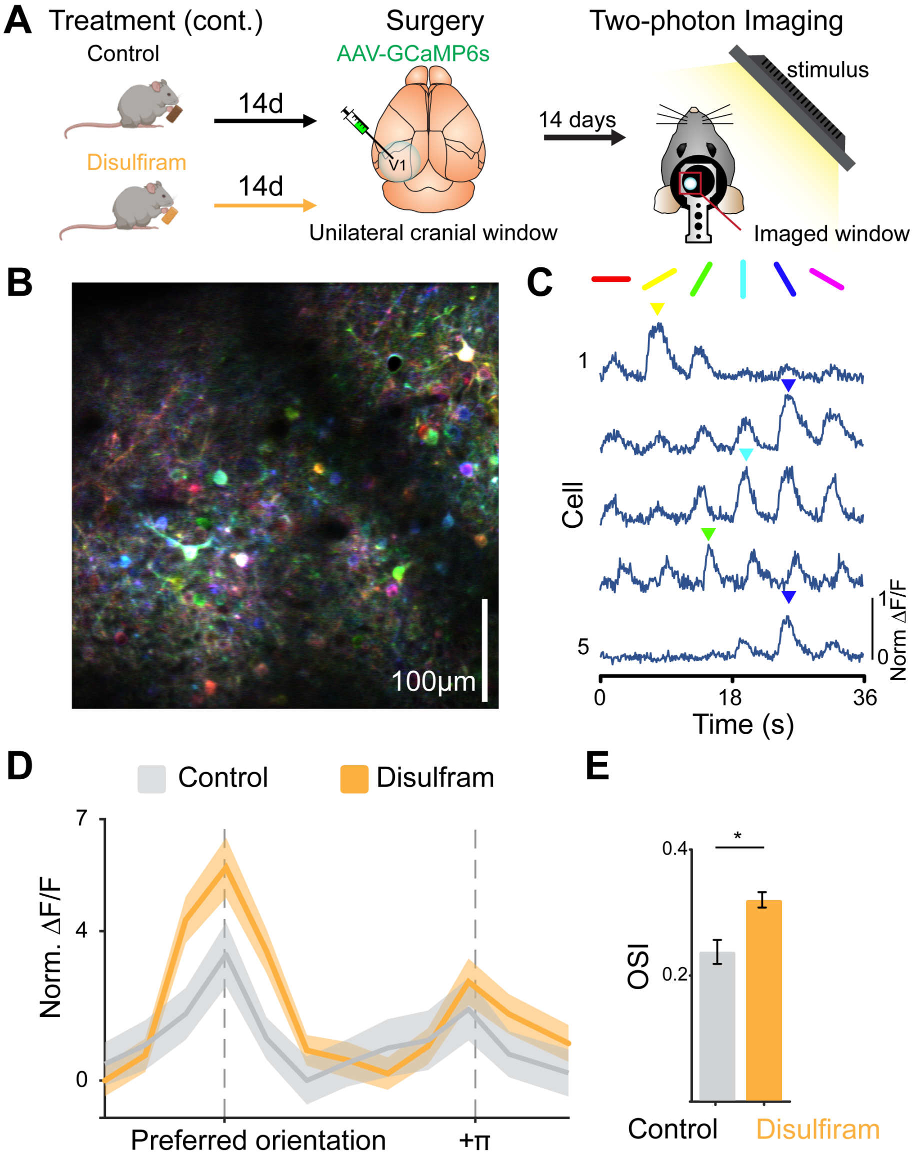

Figure 4.8: Disulfiram treatment sharpens orientation coding of visual cortical neurons. **A)** Experimental timeline for disulfiram experiments. **B)** Example traces from individual neurons in response to the drifting grating stimulus, showing responses to specific orientations. **C)** Example imaging of field from the two-photon microscope, with neurons pseudo-colored by preferred orientation (color map on the right). Scale bar, 100 μm. **D)** Aligned and averaged cross-validated tuning curves across neurons in each condition. Preferred orientation is determined using odd trials and averaged responses are shown for even trials. **E)** Disulfiram-treated neurons have significantly greater orientation selectivity indices (OSIs) than control neurons. Control: n = 605 neurons across five mice; disulfiram: n = 1791 neurons across seven mice. Values shown are means ± SEM. $F_{1,1127} = 4.77$, $p = 0.029$; two-tailed F test.

responses to complex naturalistic stimuli. To investigate this, we presented a 30 s natural scene (`http://observatory.brain-map.org/visualcoding/stimulus/natural_movies`) that contains a rich diversity of visual information. Others have found that individual neurons in the mouse visual cortex respond preferentially at different time points in the movie, reflecting their tuning to different combinations of higher-order features [236]. By presenting the same clip to the mouse many times, we could measure the response reliability across trials while remaining unbiased to any specific visual feature (Figure 4.9A). A highly reliable response suggests that a neuron is coding information about that particular frame with high fidelity.

We found high variability in the response properties of cortical neurons in rd10 mice, with many exhibiting low reliability. However, the distribution of reliability values was shifted significantly by disulfiram treatment, with an increase in the proportion of neurons showing high reliability ($F_{1,1610} = 4.79$, $p = 0.029$; gLMEM: fixed effect for treatment, random effect for mouse; Figure 4.9B). On average, reliability across the population was increased by >1.7 fold, from 0.1022 to 0.1751 by disulfiram, consistent with higher-fidelity detection of high-order visual features. Because of the high variability in response properties, we questioned whether disulfiram affected all cells equally (an additive shift) or unequally (a multiplicative shift). To answer this, we first calculated deciles of the reliability for each population of neurons and then separated and compared reliability within each matched decile group under control and disulfiram conditions (Figure 4.9C). We found a significant interaction between treatment condition and decile group, suggesting that the effects of disulfiram treatment differentially affect neurons, depending on their response fidelity (treatment and decile group interaction: $F_{1,1610} = 223.61$, $p = 2.13\times10^{-37}$; gLMEM: fixed effect for treatment and decile, random effect for mouse).

We next reasoned that sharpened feature selectivity would improve the population-level representation of the naturalistic movie stimulus. To test this, we used an ideal

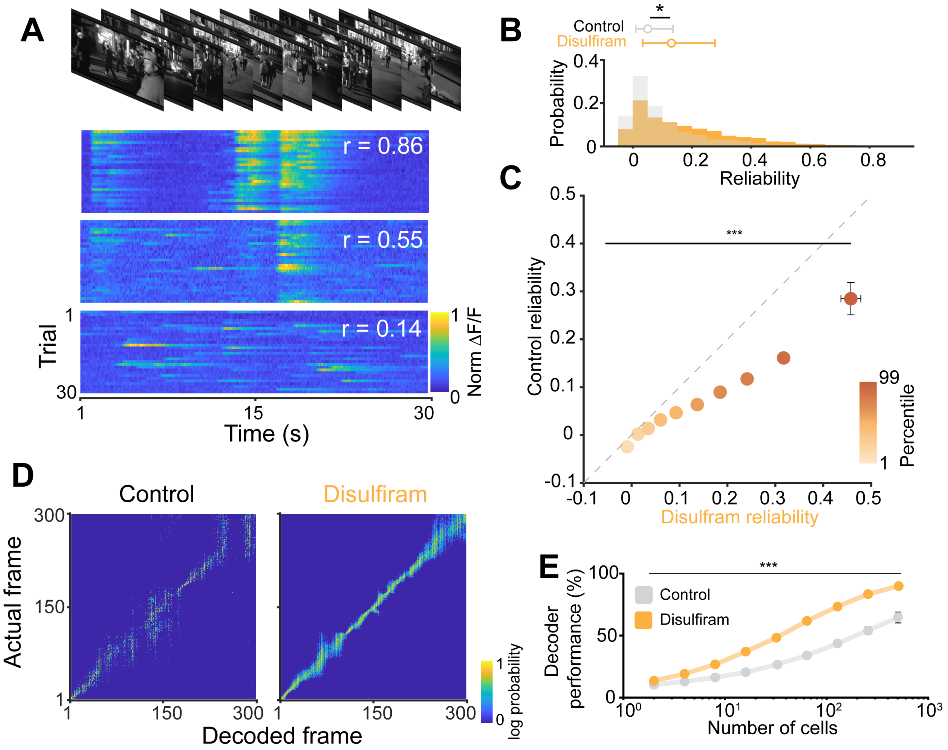

Figure 4.9: Disulfiram treatment improves coding of naturalistic scenes in V1. **A)** Top: Example frames from the movie clip presented to rd10 mice. Bottom: Example responses from three different neurons to repeated presentations of the movie. Each row is the response to a single presentation. Different neurons show varying amounts of response reliability to repeated presentations. **B)** Comparison of the response reliability of neurons from disulfiram-treated versus control-treated mice (experimental design similar to Fig. 6A). Neurons in disulfiram mice show significantly greater reliability compared to neurons from control mice. **C)** Comparison of reliability segmented by deciles. Reliability is similar in lower deciles but becomes significantly greater for disulfiram-treated mice in higher deciles. **D)** Performance of a population-level decoder across control (left) versus disulfiram-treated (right) mice. **E)** Across all population sizes used for decoding, disulfiram treatment shows significantly improved performance (predicted frame within 10 frames of actual frame) compared to control. (B, C, and E) Values shown are means ± SEM. Control: n = 1006 neurons across seven mice; disulfiram: n = 2075 neurons across nine mice. Two-tailed F test in (B), $F_{1,2066} = 5.27$, $p = 0.022$; in (C), $F_{1,2064} = 58.08$, $***p = 3.82 \times 10^{-14}$; in (E), $F_{1,79} = 16.20$, $***p = 1.30 \times 10^{-4}$.

observer analysis to decode the current frame of the movie based on the neuronal population responses (Figure 4.9D; see Methods). We carried out this analysis over many iterations, using different sized pools of randomly selected neurons from both disulfiram and control mice. To quantify the performance of the decoder, we calculated the percentage of iterations in which the decoded frame was within 10 frames (1 s) of the actual frame (Figure 4.9E). We found that decoding in disulfiram-treated mice consistently outperformed that of control mice across neuronal pool sizes (treatment group effect: $F_{1,79} = 16.20$, $p = 1.30 \times 10^{-4}$; gLMEM for treatment and pool size). These experiments indicate that disulfiram treatment leads to more robust encoding of complex features found in naturalistic scenes, consistent with improved visual perception.

We next repeated these analyses to ask whether inhibiting RAR with BMS 493 could also improve visual processing of complex stimuli (Figure 4.10A). For these experiments, each mouse was anesthetized and BMS 493 was injected intravitreally into one eye while the contralateral eye received vehicle. At 4 to 6 days after injection, we compared responses of cortical neurons to visual stimuli displayed individually to each eye. We recorded Ca^{2+} responses from the monocular zone of the primary visual cortex, which selectively receives information from the contralateral eye. This procedure allowed a within-mouse comparison of cortical response properties, eliminating possible concerns about variability in the degree of retinal degeneration between individual mice.

Comparison across treated and untreated neuronal populations showed significantly increased OSIs in neurons receiving input from the BMS 493–treated eye than from the vehicle-treated eye ($F_{1,1076} = 10.67$, $p = 0.001$; gLMEM: fixed effect for treatment, random effect for mouse; Figure 4.10, B and C). These neurons also exhibited markedly increased response reliability to the naturalistic movies ($F_{1,1961} = 102.51$, $p = 1.61 \times 10^{-23}$; gLMEM: fixed effect for treatment, random effect for mouse; Figure 4.10D). As with disulfiram, comparing reliabilities across deciles also suggested a multiplicative effect of BMS

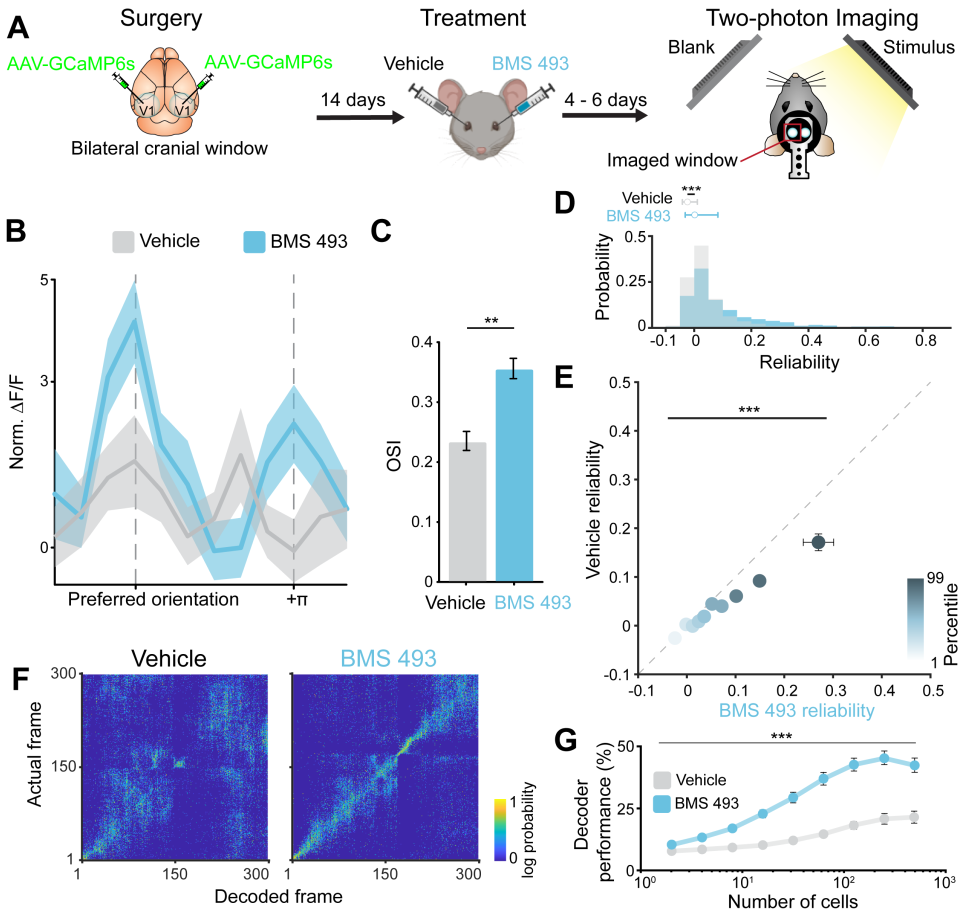

Figure 4.10: Intravitreal BMS 493 injection improves visual processing in contralateral V1. **A)** Experimental timeline for BMS 493 experiments. **B)** Aligned and averaged cross-validated tuning curves across neurons in each treatment condition. Preferred orientation is determined using odd trials, and averaged responses are shown for even trials. Injection of BMS 493 results in increased response amplitude at the preferred orientation compared to vehicle. **C)** Neurons contralateral to the BMS 493–treated eye show increased OSI as compared to neurons contralateral to the vehicle eye. Values are shown as means ± SEM. Control: n = 1428 neurons across 13 mice; BMS 493: n = 1577 neurons across 13 mice. $F_{1,1076} = 10.67$, * $p = 0.001$; two-tailed F test. **D)** Neurons contralateral to the BMS 493–treated eye show significantly higher average reliability compared to neurons contralateral to the vehicle treated eye. Control: n = 1429 neurons across 13 mice; BMS 493: n = 1599 neurons across 13 mice. $F_{1,1961} = 102.51$, $***p = 1.61 \times 10^{-23}$; two-tailed F test. **E)** Comparison of reliability segmented by deciles. Reliability is similar in lower deciles but becomes significantly greater for BMS 493 neurons at higher deciles. $F_{1,1959} = 191.58$, $***p = 1.23 \times 10^{-41}$; two-tailed F test. **F)** Performance of a population-level decoder across vehicle (left) and BMS 493–treated (right) populations. **G)** Across population sizes, BMS 493 treatment exhibits improved decoding performance as compared to vehicle. $F_{1,144} = 14.49$, $***p = 2.08 \times 10^{-4}$; two-tailed F test.

493 (treatment and decile group interaction: $F_{1,1959} = 191.58$, $p = 1.23 \times 10^{-41}$; gLMEM: fixed effect for treatment and decile, random effect for mouse; Figure 4.10E). Last, ideal observer analyses showed much greater decoding accuracy in V1 neurons contralateral to the BMS 493–treated eye compared to neurons contralateral to the vehicle-treated eye ($F_{1,144} = 14.49$, $p = 2.08 \times 10^{-4}$; gLMEM for treatment and pool size; Figure 4.10, F and G). Together, these experiments indicate that BMS 493 can rescue responses to complex visual stimuli in downstream cortical neurons during retinal degeneration.Comparison across treated and untreated neuronal populations showed significantly increased OSIs in neurons receiving input from the BMS 493–treated eye than from the vehicle-treated eye ($F_{1,1076} = 10.67$, $p = 0.001$; gLMEM: fixed effect for treatment, random effect for mouse; Figure 4.10, B and C). These neurons also exhibited markedly increased response reliability to the naturalistic movies ($F_{1,1961} = 102.51$, $p = 1.61 \times 10^{-23}$; gLMEM: fixed effect for treatment, random effect for mouse; Figure 4.10D). As with disulfiram, comparing reliabilities across deciles also suggested a multiplicative effect of BMS 493

(treatment and decile group interaction: $F_{1,1959} = 191.58$, $p = 1.23 \times 10^{-41}$; gLMEM: fixed effect for treatment and decile, random effect for mouse; Figure 4.10E). Last, ideal observer analyses showed much greater decoding accuracy in V1 neurons contralateral to the BMS 493–treated eye compared to neurons contralateral to the vehicle-treated eye ($F_{1,144} = 14.49$, $p = 2.08 \times 10^{-4}$; gLMEM for treatment and pool size; Figure 4.10, F and G). Together, these experiments indicate that BMS 493 can rescue responses to complex visual stimuli in downstream cortical neurons during retinal degeneration.

4.6 Discussion

As photoreceptors degenerate, the retina undergoes morphological and physiological plasticity, some of which is thought to be adaptive, but much of which is maladaptive. In certain respects, downstream circuit function is resilient. Selective loss of rods leads to compensatory changes in the rod synaptic pathway to restore synaptic strength [237, 238], and loss of cones leads to similar changes in the cone pathway [239]. However, our studies have shown that RA-induced hyperactivity is maladaptive, adding background noise that obscures signals that are already attenuated by the loss of photoreceptors [207]. Here, we find that RA-induced hyperactivity impairs not only simple light detection but also higher-order visual capabilities, such as reliable detection of specific visual scenes.

Visual information is ordinarily transmitted from the retina to the brain in the form of an RGC spike frequency code. Hypothetically, the code might be replicable with prosthetic devices or optogenetic tools that artificially stimulate RGCs in response to light [240]. However, accurate replication of the code is limited by the background firing rate of RGCs. If artificially stimulated firing is superimposed on hyperactive spontaneous firing, then the proper encoding of input stimuli will be altered, corrupting the accurate representation of visual features. Corrupted neural processing masks visual system function at multiple levels, from RGC responses [207] to orientation tuning and representation of scenes by the visual cortex to behavioral image recognition. The loss of photoreceptors is the ultimate cause of vision loss, but our findings indicate that physiological remodeling in downstream neurons contributes significantly to visual decline. Moreover, inhibiting RA-induced changes can mitigate impairment of simple or complex visual functions, even in mice with late-stage photoreceptor degeneration. These findings suggest RA synthesis or signaling inhibitors as tools for therapeutic improvement of low vision in humans.

Indirect evidence strongly suggests that RA-induced retinal hyperactivity contributes to human vision impairment [214]. Direct evidence, however, will be difficult to obtain because methods for detecting hyperactivity are invasive and therefore inappropriate for humans. In animal models of RP, hyperactivity can be detected directly with electrophysiological recordings from isolated retina, but RP is a rare disease, greatly restricting the availability of postmortem human retinal samples for possible electrophysiological recording. Noninvasive methods appropriate for the intact human visual system include field potential recordings from retina (ERG) or brain (electroencephalogram) and radiological methods such as functional magnetic resonance imaging or positron emission tomography scans. However, at least currently, these methods are designed to report stimulus-evoked responses, not background activity.

Likewise, directly detecting heightened RA in the human eye is fraught with difficulties. RAR binds to all-trans RA with a dissociation constant in the subnanomolar range [Kd = 0.4 nM [225]], suggesting that the ambient concentration of RA is very low. In addition, RA is labile owing to rapid enzymatic degradation by enzymes of cytochrome P450 family 26 (Cyp26) [241]. The combination of low concentration and short half-life makes direct measurement of RA practically impossible, particularly in subregions of the retina (e.g., in regions of geographic atrophy). An alternative is indirect detection, for example, with a RAR reporter gene incorporating the RA response element (RARE) sequence to drive fluorescent protein expression. However, delivery of a nontherapeutic reporter gene is considered too invasive and risky for implementation in humans, at least at present. Unfortunately, nonhuman primates with RP have been found only very recently (two individual macaques) [242], limiting direct validation of heightened RA signaling to other mammalian models.

These issues make our results with disulfiram particularly exciting and compelling. Because disulfiram is FDA-approved with safety that has been established over decades [228], it should face low regulatory hurdles for trials in humans with RP or other similar disorders. Our results on vision-impaired mice show that disulfiram improves behavioral contrast sensitivity, sharpens cortical neuron representations of spatial orientation, and increases the fidelity of responses to naturalistic scenes, all consistent with improved visual perception. Whether disulfiram will improve vision in humans remains to be seen, but the barriers to answering this question seem relatively low. If disulfiram shows efficacy, then it could be administered orally, but local ocular delivery involving a new drug formulation might ultimately be more appropriate for avoiding the undesired systemic consequences associated with alcohol consumption. Disulfiram nonselectively inhibits all ALDH isozymes, but new drug candidates selectively targeting RALDH isoforms in the retina [224] might also help remove these concerns.

Our results show that inhibiting RAR also improves vision. We used BMS 493, a pan-RAR inverse agonist that acts on RAR co-repressor protein [225, 231]. BMS 493 is potent and effective, but there is a rich pharmacopeia of other small-molecule agents that also interact with the RA binding site on RAR, the co-repressor or the coactivator, acting as agonists, antagonists, or inverse agonists. There are also agents that inhibit RXR, a protein that forms an obligate dimer with RAR before binding to DNA [243]. Determining which agent will have the most appropriate pharmacological properties for therapeutic vision rescue requires further studies of efficacy, toxicity, pharmacokinetics, and pharmacodynamics.

RAR expression or activity can also be inhibited by gene therapy. We have shown that a dominant-negative mutant of the RARα isoform (RARDN), delivered to RGCs with a targeted AAV vector, suppresses hyperactivity and augments light responses in rd10 mice [207]. AAV-mediated gene delivery has the advantage of allowing cell type targeting, which may benefit from the discovery of gene regulatory elements that may be expressed preferentially in retinal neurons that are most severely affected by RA-induced remodeling. However, in nonhuman primates, AAV-mediated gene delivery is limited by uneven penetration of the virus across the inner limiting membrane, restricting viral transduction to a ring of RGCs surrounding the fovea [244]. This scenario will presumably apply to humans as well. To avoid viral delivery limitations, other genetic tools may be appropriate for suppressing RAR expression, including RNA-interfering molecules such as antisense oligonucleotides (ASOs) and small interfering RNAs (siRNAs). These molecules are much smaller than viruses, and after lipid modification, they can cross the inner limiting membrane and inhibit gene expression across the lateral extent of the retina [245, 246]. ASOs and siRNAs are in clinical trials for other eye disorders, and advances in their design may generally benefit this strategy for suppressing RA signaling.

In principle, light responses could be unmasked and vision could be improved by directly inhibiting the ion channels that underlie hyperactivity. Gap junction proteins [247], P2X receptors [201], and hyperpolarization-activated cyclic nucleotide-gated (HCN) channels [210] have all been implicated in remodeling, making them potential drug targets for vision improvement. However, these channels are all normally expressed in the healthy retina, and it might be impossible to block them without affecting normal function. It is possible that RA is the common signal for up-regulating these channels, in which case, a single RA inhibitor might reduce their expression in a coordinated manner. RAR is largely inactive in adult RGCs [207], so an RAR inhibitor might reverse hyperactivity in degenerated regions of the retina without affecting normal function in regions with healthy photoreceptors.

Outer segments of rods and cones completely disappear in no–light perception patients with end-stage RP. However, at least some patients retain cone cell bodies that continue to express cone-specific genes, and these cells remain synaptically connected to bipolar cells [248]. The hyperactivity of downstream RGCs may obscure small light responses produced by these remnant cones, raising the possibility that elevated RA might obscure perception. Thus, there is the possibility that RALDH or RAR inhibitors might awaken light perception in patients otherwise considered completely blind.

Because RAR is relatively inactive in healthy RGCs, RAR inhibitors should act preferentially on regions of the retina where degeneration has taken place, bypassing healthy retinal regions. RA-induced gene expression is not limited to inherited retinal degeneration; it also occurs in response to photoreceptor degeneration caused by photodamage [211] and local physical detachment from the RPE [213]. This suggests that corruption of retinal processing may apply to many disorders that can cause loss of rods and cones, including retinal detachment, photodamage, and perhaps AMD.

Rescue of visual function by RAR may extend useful vision for months or years, but there is no evidence that it will slow photoreceptor degeneration itself. The strategy of rescuing vision with RA inhibitors is distinct from the strategy of restoring vision with retinal prosthetics, optogenetic and optopharmacological tools, or cell-based therapies. Vision restoration therapies are aimed, at least for now, at the small fraction of patients with end-stage photoreceptor degeneration, but treatments targeting the RA pathway may be relevant to the much larger patient population with low vision. Moreover, reducing RGC hyperactivity with RA inhibitors might be beneficial even after all the photoreceptors have degenerated and light perception is absent. Responses evoked by optoelectric [249, 250], optogenetic [198, 251], or optopharmacological [252, 253] stimulation of the degenerated retina are superimposed on the heightened background activity of RGCs, curtailing the encoding of visual images. The combination of a light-sensitive actuator with an RAR inhibitor could have a synergistic effect, boosting neural signals to more effectively restore visual function to patients with no light perception.

Chapter 5

General Conclusion

5.1 Summary of experimental results

Organization of coherent motion responsiveness in mouse visual cortex

In the primate visual cortex, only specific areas, such as areas MT and MST [29], are responsive to coherent motion, forming a highly localized and specialized processing pathway. First, we showed awake mice a coherent motion stimulus while simultaneously recording from the entire visual cortex. Unlike primate visual cortex, in which only specific HVAs are responsive to coherent motion, we found that all measured visual areas showed at least some responsiveness to coherent motion, including V1.

Next, we examined each visual area's responsiveness to coherent motion to screen for specialization as in primate visual cortex. Indeed, we found that the responsiveness to coherent motion was not equal across visual areas, rather that putative dorsal stream HVAs (AL, PM, RL, and AM) show enhanced coherent motion responsiveness as compared to ventral stream areas (LM and LI). Although the differences were not as striking as in primate cortex, the separation of areas into putative dorsal and ventral streams suggests a conserved functional organization of visual cortex across species.

By using widefield microscopy to measure across large spatial scales, we discovered that there are significant differences in coherent motion responsiveness within each visual area as well. Rather than being randomly distributed, neural responses to coherent motion were highly anticorrelated with visual elevation, forming a retinotopy-dependent mapping of coherent motion responsiveness. This effect was prominent in V1, but also across HVAs, particularly those that spanned a large visual elevation.

Influences of visual information on the HD network

One major use of visual information in rodents is to guide spatial perception, and as a result many HVAs directly synapse onto brain regions involved in navigation. We sought to understand how this visual information can be integrated with cognitive variables to support successful navigation, focusing on the HD network. Contrary to previous studies, we found that vestibular modulation was not necessary for driving the HD network. Instead, the confluence of other sensory systems, such as visual, somatosensory, and proprioceptive were sufficient for faithfully activating HD neurons. We found that visual stimuli were particularly important in the absence of vestibular information.

Next, we used a two-photon microscope to record, for the first time, the projections from ADN and HVAs to the RSC. Unlike previous approaches, the combination of calcium imaging and genetically-defined cell types enabled us to specifically measure only those projections from upstream areas to RSC, leading to a highly specific measurement of responses from each area. To separate the responses from heading versus visual areas, we utilized a bilaterally symmetric environment and manipulated the lighting conditions. We found that the responses from ADN and HVAs were very different from each other.

Responses from ADN faithfully represented the animal's heading with a unitary peak that persisted in darkness. On the other hand, HVA responses were strongly influenced by the bilateral symmetry of the environment, resulting in dual peaks that disappeared in darkness. These results demonstrate that the RSC receives multiple nonoverlapping sources of highly tuned responses.

We found that neurons in the RSC were organized into three functional clusters: 1) heading, 2) landmark, and 3) alignment. Heading neurons faithfully represent the animal's heading, and resemble responses in HD areas, such as ADN. Landmark neurons, on the other hand, are strongly influenced by visual stimuli, and strongly resemble the responses recorded from the visual terminals. Finally, alignment neurons exhibit responses that seem to be a combination of the heading and landmark neurons. Alignment neurons have a response similar to the landmark neurons in the light-on condition, with dual symmetric peaks, but resemble heading neurons in the light-off condition. Interestingly, rather than the single light-off peak being randomly distributed, we found that the light-off peak was always aligned with one of the peaks from the light-on condition, suggesting that the alignment cells integrate co-tuned responses. Therefore, these cells may be particularly important for aligning heading tp visual cues in the external environment. These results show that there are unique emergent functional responses in the RSC that are particularly important for registered heading and visual information.

Targeting the RA signaling pathway reduces RGC hyperactivity and rescues cortical visual responses

Retinal disorders are one of the most prevalent causes of vision loss; therefore, understanding their disease mechanism and potential treatment avenues is crucial to improving the quality of life of hundreds of millions of people worldwide. Using FDA-approved retinoic acid inhibitors, we were able to significantly improve visual processing across multiple scales. First, we showed that blocking retinoic acid signaling reduced hyperactivity in RGCs, enhancing their sensitivity to flashes of light. Next, we trained mice on a contrast detection task, and demonstrated that the treatment improved their task performance. Lastly, we performed calcium imaging in awake mice and found that treatment with retinoic acid inhibitors improved neural encoding and processing of visual information across multiple stimuli. These results present a thorough study of the mechanism and effects of retinoic acid inhibitors on photoreceptor degenerative disorders, increasing our understanding and enabling future treatment options for this family of diseases.

5.2 General Discussion of results

Differences in physiological measurements

Many of the claims presented here require the assumption that the optical measurement of calcium indicators is functionally analogous to electrophysiological recordings of neural activity, as previous studies of the visual cortex in primates is entirely based on these types of recordings. As a result, it is important to consider potential differences when comparing across two species as well as measurement modalities. However, significant previous work has shown that the neural activity inferred from calcium imaging reasonably reflects ground truth electrophysiological data [99]. Additionally, several experiments that have directly compared calcium imaging and electrophysiology and found that the neurons' functional responses are conserved [254].

One last important point to note is that calcium imaging does not have the temporal resolution to represent time coding [12]. Therefore, any information that may be present in the precise timing of spikes relative to either each other or to an external stimulus cannot be captured with current optical physiological techniques.

Despite these limitations, calcium imaging remains a favorable physiological technique for recording from large populations of neurons simultaneously. A new technique that utilizes much of the same technology is voltage imaging, which uses voltage sensitive dyes or proteins to provide a direct measurement of the neurons' membrane potential [255, 256, 257]. These voltage indicators tend to be significantly faster than calcium indicators, and may provide a unitary method that leverages the advantages of both systems with minimal drawbacks.

Transformation of visual stimuli in the mouse cortex

Understanding how visual stimuli are processed and transformed in the cortex has been a fundamental topic of study in systems neuroscience. Compared to other sensory systems, visual stimuli are easily manipulated and presented to animals, allowing for a high degree of stimulus control. Furthermore, extensive previous research has laid the groundwork necessary for understanding the basic neural computations in the visual cortex. By understanding how the visual cortex processes sensory information, we hope to apply these principles of cortical computation to other sensory and cognitive systems to increase our general understanding of the brain. Our results show that mouse visual cortex, as in primates, has specific regions in the brain that are optimized for processing coherent motion, demonstrating that this functional organization is consistent across mammalian species. What is the purpose of compartmentalizing the processing of stimulus features to certain brain regions? One potential benefit may be that it enables specific anatomical connectivity between neurons that is highly specialized for processing this type of information. Furthermore, it enables parallel processing of visual stimuli, allowing for highly efficient and fast derivation of important stimulus parameters for ethological behaviors. However, we also found that the mouse visual cortex is significantly less compartmentalized than primate visual cortex. Neurons in V1 are already responsive to coherent motion; whereas, in primates this property does not emerge until reaching specialized areas in the dorsal stream (namely MT and MST). Previous studies have also found a similar processing "compression" in the early visual system of mice as compared to primates [57, 87, 88]. One potential reason for this is the reduced number of HVAs found in the mouse visual cortex, requiring each area to have more roles in sensory processing.

Interestingly, there is no necessity for similar neurons to be grouped together into brain regions. Indeed in other neural systems [258], the anatomical proximity of neurons does not necessarily predict their functional connectivity. However, the brain has canonical grouping of similar neurons into brain regions, suggesting that there must be some kind of either computational, developmental, or metabolic advantage. Future research is important to understand the exact reasons, advantages, disadvantages, and mechanisms of the ordering of brain regions, particularly sensory areas, into processing hierarchies of multiple specialized brain regions.

Most surprisingly, we also found that there is significant heterogeneity in responses within each visual area as well. These retinotopic gradients in feature selectivity may represent optimizations of the visual cortex for biased processing of visual scenes. For example, because rodents are close to the ground, the majority of ethologically relevant coherent motion is found in their lower visual field, although a lower visual field bias for motion processing has been found in other species as well [110, 111]. Alternatively, the biased coherent motion information in the lower visual field may be the progenitor for driving connections that make these neurons more coherent motion responsive. One potential method of teasing apart these two potential possibilities is to use an optical element, such as a prism, to bias the upper visual field to coherent motion. If this bias is developmentally driven, then we should expect no difference in the gradient of coherent motion responsiveness. However, if the gradient reverses, i.e. upper visual field selective neurons are more coherent motion responsive that would suggest that the bias is experience dependent.

Besides the implications for visual processing, the retinotopic dependence may also enable a simple connectivity schema for transferring stimulus information up a processing hierarchy. By following retinotopic gradients, neurons in the visual cortex also exhibit a graded response to coherent motion, so that neurons with high sensitivity to motion are anatomically and spatially separated from neurons with low sensitivity. As a result, a connectivity pattern with specific downstream areas preferentially sampling different anatomically defined areas of upstream areas would result in a simple mechanism for generating specialized areas with unique response properties. Outside of the visual cortex, many sensory areas also exhibit some kind of topographic mapping, such as the tonotopic map in primary auditory cortex [259, 260]; therefore, this mechanism may have widespread implications for understanding how specialized higher processing areas can be generated from primary sensory areas.

Integration of visual information into the HD network

Previous tracing studies have shown that one of the major projections from the HVAs is to an area called the RSC, which is an important cortical area in the HD network. [118, 119] Although previous anatomical [148, 149, 150, 151] and functional [152, 153, 154, 155, 156, 157] studies have demonstrated the importance of visual input in the HD network, the mechanism by which this information is integrated has remained elusive. Because visual information only reaches a few cortical HD areas, there has been a strong focus on these areas in the past few years. One limitation of previous studies is that the proportion of HD responsive cells in these areas is low compared to subcortical HD areas, such as the ADN. As a result, it is difficult to understand the population level mechanisms that are involved in integrating sensory information into the HD network. In our study, we used the high throughput of calcium imaging to record simultaneously from hundreds of cells, allowing us to not only examine the responses of single cells, but also the interactions between cells across large spatial scales. Importantly, we showed that the HD network can still faithfully represent an animal's orientation in its environment despite a lack of vestibular modulation, allowing the use of head-fixed preparations. These findings enable new approaches to study HD network utilizing cutting edge microscopy and virtual reality systems to probe the HD network in previously impossible ways. Our results suggest that specific connectivity among tuned cells from different populations may be the inherent mechanism for integrating information across neural systems. Previous research has suggested that cells that share tuning properties are more likely to be anatomically connected [261], although these studies have largely been limited within a single region. As many sensory processes are performed by networks of areas, rather than individual areas, a similar connectivity pattern may emerge between related cortical areas, linking tuned neurons not just within brain regions, but across brain regions.

Effects of targeting RA signaling

Many higher level cognitive systems, including navigation, rely on vision for their primary window to the outside world. Therefore, visual impairments have a disproportionately strong effect on the proper function of these systems. One set of diseases that causes blindness are photoreceptor degenerative diseases, such as RP and AMD. Our study provides the most comprehensive understanding of the mechanism and implications of treatments targeting the RA signaling pathway. Although these treatments cannot recover the photoreceptors that have already degraded, the progressive nature of these diseases means that managing the symptoms and recovering sight is highly feasible. By reducing the hyperactivity of RGCs in the retina caused by RA signaling, we were able to recover cellular responses in the retina, visual coding in the cortex, and behavioral output. Besides treating these diseases directly, these results are also complementary to other strategies for restoring vision loss, such as retinal implants, by reducing stimulusn independent noise in hyperative RGCs [262].

5.3 Future directions

Distribution of other visual stimulus features

Although we focused on the processing of coherent motion, visual stimuli also contain many other stimulus features that may share a similar processing strategy. For example, ventral stream areas in primates are specialized to process textures, and research in mice suggests a similar specialization of HVAs. As a result, a similar set of experiments can be performed as above to see whether texture processing also follows a retinotopic gradient within visual areas. Furthermore, this strategy could be applied to other sensory systems, although the types of sensory transformation present in other systems is less well understood. Together, these experiments would support that an anisotropic organization of stimulus feature processing is a fundamental cortical strategy.

Understanding how retinotopically correlated stimulus features aids transfer of information

What is the purpose of topographic organization? For simple stimulus features, such as receptive field location, a topographic organization may be beneficial for local processing of information. However, for more complex features that no longer parallel the physical world, the necessity of a topographical organization is diminished. One potential purpose of this organization is in order to facilitate transfer of information along a hierarchical processing stream. In order to test this, we could perform retrograde tracing from specific HVAs to map which areas preferentially project to them. In line with our results above, we would expect that HVAs that are particularly responsive to coherent motion should receive projections from anterior V1, which contains more motion-sensitive neurons. These experiments can help to reveal a general principle of how specifically tuned information is passed between brain regions utilizing a simple and biologically feasible connectivity pattern.

Dissecting circuit mechanisms of visual integration into HD network

Although our experiments have started to identify potential key cell types for integrating visual information in the HD network, the exact mechanism and specific connectivity between these cell types is still unclear. In order to understand the contributions of each cell type in the overall representation of heading, we can dissociate their inputs. As a first step, we can repeat similar experiments as above, but use a cage with a separated bottom, allowing the visual cues on the walls to independently rotate from the bottom of the cage. Because we postulate that the heading cells primarily receive information from non-visual sources (given that they retain tuning in darkness), we expect that they will track the movement of the bottom of the cage; whereas landmark cells will follow the rotation of the visual cue. We can then examine how the responses of the alignment cells respond to this manipulation. Another possibility is taking advantage of our head-fixed preparation to use holographic stimulation of specific functionally defined cells in order to understand the fine-scale connectivity between individual neurons or groups of neurons. Together, these experiments can help elucidate the specific connections in the RSC that support its role in registering internal heading to the external world.

Future treatments of photoreceptor degenerative disorders

One important result from our experiments is that we used FDA-approved drugs to target the RA signaling pathway. As a result, there is high potential for clinical trials to see if a similar pathway is affected in human disorders, and, importantly, whether these treatments can improve visual processing in human patients. Combined with other vision restorative treatments, such as artificial retinae, significant improvements in the quality of life for those affected by photoreceptor degenerative disorders is very likely.

5.4 Conclusion

Understanding how sensory stimuli can be integrated into cognitive processes is a fundamental goal of neuroscience. In these studies, we leveraged state-of-the-art tools to examine and understand sensory processing at scales that were previously inaccessible. Moving forward, the continued development of new tools will further enable greater measurement and manipulation of larger populations of neurons, resulting in increased understanding of how visual processing works. These results have important implications not just for basic science but also to help provide groundwork for treating sensory processing disorders. In the end, our continued investigation and understanding of the processing of visual information along the cortical hierarchy provides a tractable and fruitful avenue for unravelling more general rules of sensory and cortical processing.

Bibliography

[1] B. Panizza, *Osservazioni sul nervo ottico.* Bernardoni, 1855.

[2] H. B. Barlow and W. R. Levick, *The mechanism of directionally selective units in rabbit's retina.*, *The Journal of Physiology* **178** (jun, 1965) 477–504.

[3] H. K. Hartline, *the Response of Single Optic Nerve Fibers of the Vertebrate Eye To Illumination of the Retina*, *American Journal of Physiology-Legacy Content* **121** (1938), no. 2 400–415.

[4] S. W. KUFFLER, *Discharge patterns and functional organization of mammalian retina*, *Journal of neurophysiology* **16** (jan, 1953) 37–68.

[5] G. Wald, *Molecular basis of visual excitation*, oct, 1968.

[6] D. H. Hubel and T. N. Wiesel, *Receptive fields, binocular interaction and functional architecture in the cat's visual cortex*, *The Journal of Physiology* **160** (jan, 1962) 106–154.

[7] M. Ferrara, G. Lugano, M. T. Sandinha, V. R. Kearns, B. Geraghty, and D. H. Steel, *Biomechanical properties of retina and choroid: a comprehensive review of techniques and translational relevance*, *Eye (Basingstoke)* **35** (mar, 2021) 1818–1832.

[8] S. Hecht, S. Shlaer, and M. H. Pirenne, *Energy, quanta, and vision*, *Journal of General Physiology* **25** (jul, 1942) 819–840.

[9] G. S. Mannu, *Retinal phototransduction*, *Neurosciences* **19** (2014), no. 4 275–280.

[10] B. R. Conway, S. Chatterjee, G. D. Field, G. D. Horwitz, E. N. Johnson, K. Koida, and K. Mancuso, *Advances in color science: From retina to behavior*, *Journal of Neuroscience* **30** (nov, 2010) 14955–14963.

[11] G. M. Zeck, Q. Xiao, and R. H. Masland, *The spatial filtering properties of local edge detectors and brisk-sustained retinal ganglion cells*, *European Journal of Neuroscience* **22** (oct, 2005) 2016–2026.

[12] W. Bialek and W. G. Owen, *Temporal filtering in retinal bipolar cells. Elements of an optimal computation?*, *Biophysical Journal* **58** (1990), no. 5 1227–1233.

[13] J. H. Kaas and C. E. Collins, *The organization of sensory cortex*, *Current Opinion in Neurobiology* **11** (aug, 2001) 498–504.

[14] E. K. Miller, *The prefontral cortex and cognitive control*, *Nature Reviews Neuroscience* **1** (2000), no. 1 59–65.

[15] C. L. Ebbesen and M. Brecht, *Motor cortex - To act or not to act?*, *Nature Reviews Neuroscience* **18** (oct, 2017) 694–705.

[16] T. Mueller, *What is the thalamus in zebrafish?*, *Frontiers in Neuroscience* **0** (2012), no. MAY 64.

[17] P. Lennie, *Parallel visual pathways: A review*, *Vision Research* **20** (jan, 1980) 561–594.

[18] A. F. Oliveira and K. Yonehara, *The Mouse Superior Colliculus as a Model System for Investigating Cell Type-Based Mechanisms of Visual Motor Transformation*, *Frontiers in Neural Circuits* **12** (jul, 2018) 59.

[19] N. Sahibzada, P. Dean, and P. Redgrave, *Movements resembling orientation or avoidance elicited by electrical stimulation of the superior colliculus in rats*, *Journal of Neuroscience* **6** (1986), no. 3 723–733.

[20] P. Dean, P. Redgrave, and G. W. Westby, *Event or emergency? Two response systems in the mammalian superior colliculus*, *Trends in Neurosciences* **12** (1989), no. 4 137–147.

[21] P. Dean, I. J. Mitchell, and P. Redgrave, *Responses resembling defensive behaviour produced by microinjection of glutamate into superior colliculus of rats*, *Neuroscience* **24** (1988), no. 2 501–510.

[22] M. Tohmi, R. Meguro, H. Tsukano, R. Hishida, and K. Shibuki, *The Extrageniculate Visual Pathway Generates Distinct Response Properties in the Higher Visual Areas of Mice*, *Current Biology* **24** (mar, 2014) 587–597.

[23] G. Purushothaman, R. Marion, K. Li, and V. A. Casagrande, *Gating and control of primary visual cortex by pulvinar*, *Nature Neuroscience* **15** (jun, 2012) 905–912.

[24] M. W. Self and P. R. Roelfsema, *Scene perception in early vision: Figure-ground organization in the lateral geniculate nucleus*, *Proceedings of the National Academy of Sciences of the United States of America* **112** (jun, 2015) 6784–6785.

[25] F. Briggs and W. M. Usrey, *A fast, reciprocal pathway between the lateral geniculate nucleus and visual cortex in the macaque monkey*, *Journal of Neuroscience* **27** (may, 2007) 5431–5436.

[26] L. Paulun, A. Wendt, and N. Kasabov, *A retinotopic spiking neural network system for accurate recognition of moving objects using neucube and dynamic vision sensors*, *Frontiers in Computational Neuroscience* **12** (jun, 2018) 42.

[27] G. Holmes, *Disturbances of Vision By Cerebral Lesions*, *British Journal of Ophthalmology* **2** (jul, 1918) 353–384.

[28] T. Inouye, *Die Sehstörungen bei Schussverletzungen der kortikalen Sehsphäre: nach Beobachtungen an Verwundeten der letzten japanischen Kriege*. W. Engelmann, 1909.

[29] J. A. Movshon, E. H. Adelson, M. S. Gizzi, and W. T. Newsome, *The analysis of moving visual patterns*, in *Pattern recognition mechanisms* (&. C. G. C. Chagas, R. Gattass, ed.), pp. 117–151. Vatican Press, Rome, 1983.

[30] J. A. Perrone and A. Thiele, *Speed skills: Measuring the visual speed analyzing properties of primate MT neurons*, *Nature Neuroscience* **4** (2001), no. 5 526–532.

[31] L. G. Thorell, R. L. de Valois, and D. G. Albrecht, *Spatial mapping of monkey vi cells with pure color and luminance stimuli*, *Vision Research* **24** (1984), no. 7 751–769.

[32] T. D. Albright, *Form-cue invariant motion processing in primate visual cortex*, *Science* **255** (1992), no. 5048 1141–1143.

[33] J. R. Bergen and B. Julesz, *Rapid Discrimination of Visual Patterns*, *IEEE Transactions on Systems, Man and Cybernetics* **SMC-13** (1983), no. 5 857–863.

[34] G. C. Baylis, E. T. Rolls, and C. M. Leonard, *Selectivity between faces in the responses of a population of neurons in the cortex in the superior temporal sulcus of the monkey*, *Brain Research* **342** (sep, 1985) 91–102.

[35] M. A. Goodale and A. D. Milner, *Separate visual pathways for perception and action*, *Trends in Neurosciences* **15** (1992), no. 1 20–25.

[36] D. J. Kravitz, K. S. Saleem, C. I. Baker, L. G. Ungerleider, and M. Mishkin, *The ventral visual pathway: An expanded neural framework for the processing of object quality*, *Trends in Cognitive Sciences* **17** (jan, 2013) 26–49.

[37] M. N. Hebart and G. Hesselmann, *What visual information is processed in the human dorsal stream?*, *Journal of Neuroscience* **32** (jun, 2012) 8107–8109.

[38] V. van Polanen and M. Davare, *Interactions between dorsal and ventral streams for controlling skilled grasp*, *Neuropsychologia* **79** (dec, 2015) 186–191.

[39] A. D. Huberman and C. M. Niell, *What can mice tell us about how vision works?*, 2011.

[40] C. M. Niell and M. P. Stryker, *Highly selective receptive fields in mouse visual cortex.*, *The Journal of neuroscience : the official journal of the Society for Neuroscience* **28** (2008), no. 30 7520–36.

[41] Q. Wang, E. Gao, and A. Burkhalter, *Gateways of ventral and dorsal streams in mouse visual cortex*, *Journal of Neuroscience* **31** (2011), no. 5 1905–1918.

[42] I. T. Smith, L. B. Townsend, R. Huh, H. Zhu, and S. L. Smith, *Stream-dependent development of higher visual cortical areas*, *Nature Neuroscience* **20** (2017), no. 2 200–208.

[43] H. Sanders, C. Rennó-Costa, M. Idiart, and J. Lisman, *Grid Cells and Place Cells: An Integrated View of their Navigational and Memory Function*, *Trends in Neurosciences* **38** (dec, 2015) 763–775.

[44] J. O'Keefe, *Place units in the hippocampus of the freely moving rat*, *Experimental Neurology* **51** (1976), no. 1 78–109.

[45] M. Fyhn, S. Molden, M. P. Witter, E. I. Moser, and M. B. Moser, *Spatial representation in the entorhinal cortex*, *Science* **305** (aug, 2004) 1258–1264.

[46] T. Evans, A. Bicanski, D. Bush, and N. Burgess, *How environment and self-motion combine in neural representations of space*, *Journal of Physiology* **594** (nov, 2016) 6535–6546.

[47] J. S. Taube, R. U. Muller, and J. B. Ranck, *Head-direction cells recorded from the postsubiculum in freely moving rats. II. Effects of environmental manipulations*, *Journal of Neuroscience* **10** (1990), no. 2 436–447.

[48] J. S. Taube, *Head direction cells recorded in the anterior thalamic nuclei of freely moving rats*, *Journal of Neuroscience* **15** (1995), no. 1 I 70–86.

[49] A. D. Ekstrom, *Why vision is important to how we navigate*, *Hippocampus* **25** (jun, 2015) 731–735.

[50] W. L. Wong, X. Su, X. Li, C. M. G. Cheung, R. Klein, C. Y. Cheng, and T. Y. Wong, *Global prevalence of age-related macular degeneration and disease burden projection for 2020 and 2040: A systematic review and meta-analysis*, *The Lancet Global Health* **2** (feb, 2014).

[51] T. B. O'Neal and E. E. Luther, *Retinitis Pigmentosa*, *StatPearls* (aug, 2021).

[52] K. K. Sit and M. J. Goard, *Distributed and retinotopically asymmetric processing of coherent motion in mouse visual cortex*, *Nature Communications* **11** (jul, 2020) 1–14.

[53] K. K. Sit and M. J. Goard, *Coregistration of heading to visual cues in retrosplenial cortex*, *bioRxiv* (apr, 2022) 2022.03.25.485865.

[54] M. Telias, K. K. Sit, D. Frozenfar, B. Smith, A. Misra, M. J. Goard, and R. H. Kramer, *Retinoic acid inhibitors mitigate vision loss in a mouse model of retinal degeneration*, *Science Advances* **8** (mar, 2022) 4643.

[55] W. T. Newsome, K. H. Britten, C. D. Salzman, and J. A. Movshon, *Neuronal mechanisms of motion perception*, *Cold Spring Harbor symposia on quantitative biology* **55** (1990) 697–705.

[56] R. Rasmussen and K. Yonehara, *Circuit Mechanisms Governing Local vs. Global Motion Processing in Mouse Visual Cortex*, *Frontiers in Neural Circuits* **11** (dec, 2017) 109.

[57] T. Marques, M. T. Summers, G. Fioreze, M. Fridman, R. F. Dias, M. B. Feller, and L. Petreanu, *A Role for Mouse Primary Visual Cortex in Motion Perception*, *Current biology : CB* **28** (jun, 2018) 1703–1713.e6.

[58] L. Dyballa, M. S. Hoseini, M. C. Dadarlat, S. W. Zucker, and M. P. Stryker, *Flow stimuli reveal ecologically appropriate responses in mouse visual cortex*, *Proceedings of the National Academy of Sciences of the United States of America* **115** (oct, 2018) 11304–11309.

[59] I. A. Youngstrom and B. W. Strowbridge, *Visual landmarks facilitate rodent spatial navigation in virtual reality environments.*, *Learning & memory (Cold Spring Harbor, N.Y.)* **19** (feb, 2012) 84–90.

[60] L. L. Glickfeld and S. R. Olsen, *Higher-Order Areas of the Mouse Visual Cortex*, *Annual review of vision science* **3** (sep, 2017) 251–273.

[61] T. A. Seabrook, T. J. Burbridge, M. C. Crair, and A. D. Huberman, *Architecture, Function, and Assembly of the Mouse Visual System*, *Annual review of neuroscience* **40** (jul, 2017) 499–538.

[62] M. Mishkin and L. G. Ungerleider, *Contribution of striate inputs to the visuospatial functions of parieto-preoccipital cortex in monkeys*, *Behavioural Brain Research* **6** (sep, 1982) 57–77.

[63] M. A. Goodale and A. D. Milner, *Separate visual pathways for perception and action*, 1992.

[64] R. Dubner and S. M. Zeki, *Response properties and receptive fields of cells in an anatomically defined region of the superior temporal sulcus in the monkey*, *Brain Research* **35** (dec, 1971) 528–532.

[65] J. M. Allman and J. H. Kaas, *A representation of the visual field in the caudal third of the middle temporal gyrus of the owl monkey (Aotus trivirgatus)*, *Brain Research* **31** (aug, 1971) 85–105.

[66] J. H. Maunsell and D. C. Van Essen, *Functional properties of neurons in middle temporal visual area of the macaque monkey. I. Selectivity for stimulus direction, speed, and orientation.*, *Journal of neurophysiology* **49** (may, 1983) 1127–1147.

[67] J. A. Movshon and W. T. Newsome, *Visual response properties of striate cortical neurons projecting to area MT in macaque monkeys.*, *The Journal of neuroscience : the official journal of the Society for Neuroscience* **16** (dec, 1996) 7733–7741.

[68] W. T. Newsome and E. B. E. Pare, *A selective impairment of motion perception following lesions of the middle temporal visual area (MT)*, *The Journal of Neuroscience* (1988).

[69] C. D. Salzman, K. H. Britten, and W. T. Newsome, *Cortical microstimulation influences perceptual judgements of motion direction*, *Nature* **346** (jul, 1990) 174–177.

[70] R. J. Snowden, S. Treue, and R. A. Andersen, *The response of neurons in areas V1 and MT of the alert rhesus monkey to moving random dot patterns*, *Experimental Brain Research* **88** (feb, 1992) 389–400.

[71] E. P. Simoncelli and D. J. Heeger, *A model of neuronal responses in visual area MT*, *Vision Research* **38** (1998), no. 5 743–761, [arXiv:0911.0492].

[72] N. C. Rust, V. Mante, E. P. Simoncelli, and J. A. Movshon, *How MT cells analyze the motion of visual patterns*, *Nature Neuroscience* **9** (2006), no. 11 1421–1431.

[73] Q. Wang and A. Burkhalter, *Area map of mouse visual cortex*, *Journal of Comparative Neurology* **502** (2007), no. 3 339–357, [NIHMS150003].

[74] J. H. Marshel, M. E. Garrett, I. Nauhaus, and E. M. Callaway, *Functional specialization of seven mouse visual cortical areas*, *Neuron* **72** (2011), no. 6 1040–1054.

[75] M. L. Andermann, A. M. Kerlin, D. K. Roumis, L. L. Glickfeld, and R. C. Reid, *Functional specialization of mouse higher visual cortical areas*, *Neuron* **72** (2011), no. 6 1025–1039, [NIHMS150003].

[76] S. Weng, W. Sun, and S. He, *Identification of ON-OFF direction-selective ganglion cells in the mouse retina*, *The Journal of Physiology* **562** (feb, 2005) 915–923.

[77] T. Baden, P. Berens, K. Franke, M. Román Rosón, M. Bethge, and T. Euler, *The functional diversity of retinal ganglion cells in the mouse*, *Nature* **529** (jan, 2016) 345–350.

[78] O. S. Dhande, B. K. Stafford, K. Franke, R. El-Danaf, K. A. Percival, A. H. Phan, P. Li, B. J. Hansen, P. L. Nguyen, P. Berens, W. R. Taylor, E. Callaway, T. Euler, and A. D. Huberman, *Molecular Fingerprinting of On–Off Direction-Selective Retinal Ganglion Cells Across Species and Relevance to Primate Visual Circuits*, *Journal of Neuroscience* **39** (jan, 2019) 78–95.

[79] Y. Zhang, I.-J. Kim, J. R. Sanes, and M. Meister, *The most numerous ganglion cell type of the mouse retina is a selective feature detector.*, *Proceedings of the National Academy of Sciences of the United States of America* **109** (sep, 2012) E2391—-8.

[80] R. N. El-Danaf and A. D. Huberman, *Sub-topographic maps for regionally enhanced analysis of visual space in the mouse retina*, *Journal of Comparative Neurology* **527** (jan, 2019) 259–269.

[81] A. Cruz-Martín, R. N. El-Danaf, F. Osakada, B. Sriram, O. S. Dhande, P. L. Nguyen, E. M. Callaway, A. Ghosh, and A. D. Huberman, *A dedicated circuit links direction-selective retinal ganglion cells to the primary visual cortex*, *Nature* **507** (mar, 2014) 358–361.

[82] D. Hillier, M. Fiscella, A. Drinnenberg, S. Trenholm, S. B. Rompani, Z. Raics, G. Katona, J. Juettner, A. Hierlemann, B. Rozsa, and B. Roska, *Causal evidence for retina-dependent and -independent visual motion computations in mouse cortex*, *Nature Neuroscience* **20** (jul, 2017) 960–968.

[83] J. H. Marshel, A. P. Kaye, I. Nauhaus, and E. M. Callaway, *Anterior-Posterior Direction Opponency in the Superficial Mouse Lateral Geniculate Nucleus*, *Neuron* **76** (nov, 2012) 713–720.

[84] D. M. Piscopo, R. N. El-Danaf, A. D. Huberman, and C. M. Niell, *Diverse visual features encoded in mouse lateral geniculate nucleus.*, *The Journal of neuroscience : the official journal of the Society for Neuroscience* **33** (mar, 2013) 4642–4656.

[85] X. Zhao, H. Chen, X. Liu, and J. Cang, *Orientation-selective responses in the mouse lateral geniculate nucleus.*, *The Journal of neuroscience : the official journal of the Society for Neuroscience* **33** (jul, 2013) 12751–12763.

[86] X. Xu, J. Ichida, Y. Shostak, A. B. Bonds, and V. A. Casagrande, *Are primate lateral geniculate nucleus (LGN) cells really sensitive to orientation or direction?*, *Visual Neuroscience* **19** (jan, 2002) 97–108.

[87] G. M. Muir, J. E. Brown, J. P. Carey, T. P. Hirvonen, C. C. Della Santina, L. B. Minor, and J. S. Taube, *Disruption of the head direction cell signal after occlusion of the semicircular canals in the freely moving chinchilla*, *Journal of Neuroscience* **29** (nov, 2009) 14521–14533.

[88] G. Palagina, J. F. Meyer, and S. M. Smirnakis, *Complex Visual Motion Representation in Mouse Area V1*, *The Journal of Neuroscience* **37** (2017), no. 1 164–183.

[89] A. L. Juavinett and E. M. Callaway, *Pattern and Component Motion Responses in Mouse Visual Cortical Areas*, *Current Biology* **25** (jun, 2015) 1759–1764.

[90] M. E. Garrett, I. Nauhaus, J. H. Marshel, E. M. Callaway, M. E. Garrett, J. H. Marshel, I. Nauhaus, and M. E. Garrett, *Topography and areal organization of mouse visual cortex*, *Journal of Neuroscience* **34** (2014), no. 37 12587–12600.

[91] J. B. Wekselblatt, E. D. Flister, D. M. Piscopo, and C. M. Niell, *Large-scale imaging of cortical dynamics during sensory perception and behavior*, *Journal of Neurophysiology* **115** (jun, 2016) 2852–2866.

[92] J. Zhuang, L. Ng, D. Williams, M. Valley, Y. Li, M. Garrett, and J. Waters, *An extended retinotopic map of mouse cortex*, *eLife* **6** (2017) 1–29.

[93] Q. Wang, O. Sporns, and A. Burkhalter, *Network analysis of corticocortical connections reveals ventral and dorsal processing streams in mouse visual cortex*, *Journal of Neuroscience* **32** (mar, 2012) 4386–4399.

[94] D. H. Brainard, *The Psychophysics Toolbox*, *Spatial Vision* **10** (1997), no. 4 433–436.

[95] E. Froudarakis, P. Berens, A. S. Ecker, R. J. Cotton, F. H. Sinz, D. Yatsenko, P. Saggau, M. Bethge, and A. S. Tolias, *Population code in mouse V1 facilitates readout of natural scenes through increased sparseness*, *Nature Neuroscience* **17** (2014), no. 6 851–857.

[96] D. W. Williams and R. Sekuler, *Coherent global motion percepts from stochastic local motions*, *Vision Research* **24** (1984), no. 1 55–62.

[97] V. A. Kalatsky and M. P. Stryker, *New paradigm for optical imaging: temporally encoded maps of intrinsic signal.*, *Neuron* **38** (may, 2003) 529–545.

[98] T. Sakatani and T. Isa, *PC-based high-speed video-oculography for measuring rapid eye movements in mice*, *Neuroscience Research* (2004).

[99] T.-W. Chen, T.-W. Chen, T. J. Wardill, T. J. Wardill, Y. Sun, Y. Sun, S. R. Pulver, S. R. Pulver, S. L. Renninger, S. L. Renninger, A. Baohan, A. Baohan, E. R. Schreiter, E. R. Schreiter, R. A. Kerr, R. A. Kerr, M. B. Orger, M. B. Orger, V. Jayaraman, V. Jayaraman, L. L. Looger, L. L. Looger, K. Svoboda, K. Svoboda, D. S. Kim, and D. S. Kim, *Ultrasensitive fluorescent proteins for imaging neuronal activity.*, *Nature* **499** (2013), no. 7458 295–300, [1011.1669].

[100] L. Madisen, A. R. Garner, D. Shimaoka, A. S. Chuong, N. C. Klapoetke, L. Li, A. van der Bourg, Y. Niino, L. Egolf, C. Monetti, H. Gu, M. Mills, A. Cheng, B. Tasic, T. N. Nguyen, S. M. Sunkin, A. Benucci, A. Nagy, A. Miyawaki, F. Helmchen, R. M. Empson, T. Knöpfel, E. S. Boyden, R. C. Reid, M. Carandini, and H. Zeng, *Transgenic Mice for Intersectional Targeting of Neural Sensors and Effectors with High Specificity and Performance*, *Neuron* **85** (mar, 2015) 942–958.

[101] B. R. Payne, *Evidence for Visual Cortical Area Homologs in Cat and Macaque Monkey*, *Cerebral Cortex* **3** (jan, 1993) 1–25.

[102] B. Li, B.-W. Li, Y. Chen, L.-H. Wang, and Y.-C. Diao, *Response properties of PMLS and PLLS neurons to simulated optic flow patterns*, *European Journal of Neuroscience* **12** (may, 2000) 1534–1544.

[103] S. Zeki, J. D. Watson, C. J. Lueck, K. J. Friston, C. Kennard, and R. S. Frackowiak, *A direct demonstration of functional specialization in human visual cortex.*, *The Journal of neuroscience : the official journal of the Society for Neuroscience* **11** (mar, 1991) 641–649.

[104] A. La Chioma, T. Bonhoeffer, and M. Hübener, *Area-Specific Mapping of Binocular Disparity across Mouse Visual Cortex.*, *Current biology : CB* **29** (aug, 2019) 1–7.

[105] D. Lyamzin and A. Benucci, *The mouse posterior parietal cortex: Anatomy and functions*, *Neuroscience Research* **140** (mar, 2019) 14–22.

[106] M. Yilmaz and M. Meister, *Rapid innate defensive responses of mice to looming visual stimuli*, *Current Biology* **23** (oct, 2013) 2011–2015.

[107] C. Shang, Z. Liu, Z. Chen, Y. Shi, Q. Wang, S. Liu, D. Li, and P. Cao, *A parvalbumin-positive excitatory visual pathway to trigger fear responses in mice.*, *Science (New York, N.Y.)* **348** (jun, 2015) 1472–1477.

[108] D. A. Evans, A. V. Stempel, R. Vale, S. Ruehle, Y. Lefler, and T. Branco, *A synaptic threshold mechanism for computing escape decisions*, *Nature* **558** (2018), no. 7711 590–594.

[109] L. L. Glickfeld, M. L. Andermann, V. Bonin, and R. C. Reid, *Cortico-cortical projections in mouse visual cortex are functionally target specific*, *Nature Neuroscience* **16** (2013), no. 2 219–226.

[110] M. W. Levine and J. J. McAnany, *The relative capabilities of the upper and lower visual hemifields*, *Vision Research* **45** (2005), no. 21 2820–2830.

[111] G. A. Zito, D. Cazzoli, R. M. Müri, U. P. Mosimann, and T. Nef, *Behavioral Differences in the Upper and Lower Visual Hemifields in Shape and Motion Perception*, *Frontiers in Behavioral Neuroscience* **10** (jun, 2016) 128.

[112] S. Aihara, T. Yoshida, T. Hashimoto, and K. Ohki, *Color Representation Is Retinotopically Biased but Locally Intermingled in Mouse V1.*, *Frontiers in neural circuits* **11** (2017) 22.

[113] M. Minderer, K. D. Brown, and C. D. Harvey, *The Spatial Structure of Neural Encoding in Mouse Posterior Cortex during Navigation.*, *Neuron* **102** (apr, 2019) 232—-248.e11.

[114] S. S. Kim, H. Rouault, S. Druckmann, and V. Jayaraman, *Ring attractor dynamics in the Drosophila central brain*, *Science* **356** (may, 2017) 849–853.

[115] J. D. Seelig and V. Jayaraman, *Neural dynamics for landmark orientation and angular path integration*, *Nature* **521** (may, 2015) 186–191.

[116] M. J. Beetz, C. Kraus, M. Franzke, D. Dreyer, M. F. Strube-Bloss, W. Rössler, E. J. Warrant, C. Merlin, and B. el Jundi, *Flight-induced compass representation in the monarch butterfly heading network*, *Current Biology* **32** (jan, 2022) 338–349.e5.

[117] S. Leutgeb, K. E. Ragozzino, and S. J. Mizumori, *Convergence of head direction and place information in the CA1 region of hippocampus*, *Neuroscience* **100** (sep, 2000) 11–19.

[118] J. Cho and P. E. Sharp, *Head direction, place, and movement correlates for cells in the rat retrosplenial cortex*, *Behavioral Neuroscience* **115** (2001), no. 1 3–25.

[119] L. L. Chen, L. H. Lin, E. J. Green, C. A. Barnes, and B. L. McNaughton, *Head-direction cells in the rat posterior cortex - I. anatomical distribution and behavioral modulation*, *Experimental Brain Research* **101** (sep, 1994) 8–23.

[120] R. W. Stackman and J. S. Taube, *Firing properties of rat lateral mammillary single units: Head direction, head pitch, and angular head velocity*, *Journal of Neuroscience* **18** (nov, 1998) 9020–9037.

[121] J. S. Taube, R. U. Muller, and J. B. Ranck, *Head-direction cells recorded from the postsubiculum in freely moving rats. I. Description and quantitative analysis*, *Journal of Neuroscience* **10** (1990), no. 2 420–435.

[122] J. J. Knierim, H. S. Kudrimoti, and B. L. McNaughton, *Place cells, head direction cells, and the learning of landmark stability*, *Journal of Neuroscience* **15** (1995), no. 3 I 1648–1659.

[123] H. T. Blair and P. E. Sharp, *Anticipatory head direction signals in anterior thalamus: Evidence for a thalamocortical circuit that integrates angular head motion to compute head direction*, *Journal of Neuroscience* **15** (sep, 1995) 6260–6270.

[124] J. S. Taube and R. U. Muller, *Comparisons of head direction cell activity in the postsubiculum and anterior thalamus of freely moving rats*, *Hippocampus* **8** (1998), no. 2 87–108.

[125] J. S. Taube and J. P. Bassett, *Persistent Neural Activity in Head Direction Cells*, *Cerebral Cortex* **13** (nov, 2003) 1162–1172.

[126] R. W. Stackman and J. S. Taube, *Firing properties of head direction cells in the rat anterior thalamic nucleus: Dependence on vestibular input*, *Journal of Neuroscience* **17** (jun, 1997) 4349–4358.

[127] R. W. Stackman, A. S. Clark, and J. S. Taube, *Hippocampal spatial representations require vestibular input*, *Hippocampus* **12** (2002), no. 3 291–303.

[128] H. T. Blair, J. Cho, and P. E. Sharp, *Role of the lateral mammillary nucleus in the rat head direction circuit: A combined single unit recording and lesion study*, *Neuron* **21** (1998), no. 6 1387–1397.

[129] R. J. Frohardt, J. P. Bassett, and J. S. Taube, *Path integration and lesions within the head direction cell circuit: Comparison between the roles of the anterodorsal thalamus and dorsal tegmental nucleus*, *Behavioral Neuroscience* **120** (feb, 2006) 135–149.

[130] D. Aronov and D. W. Tank, *Engagement of Neural Circuits Underlying 2D Spatial Navigation in a Rodent Virtual Reality System*, *Neuron* **84** (oct, 2014) 442–456.

[131] A. Arleo, C. Déjean, P. Allegraud, M. Khamassi, M. B. Zugaro, and S. I. Wiener, *Optic flow stimuli update anterodorsal thalamus head direction neuronal activity in rats*, *Journal of Neuroscience* **33** (2013), no. 42 16790–16795.

[132] X. Chen, G. C. DeAngelis, and D. E. Angelaki, *Flexible egocentric and allocentric representations of heading signals in parietal cortex*, *Proceedings of the National Academy of Sciences of the United States of America* **115** (apr, 2018) E3305–E3312.

[133] L. Acharya, Z. M. Aghajan, C. Vuong, J. J. Moore, and M. R. Mehta, *Causal Influence of Visual Cues on Hippocampal Directional Selectivity*, *Cell* **164** (jan, 2016) 197–207.

[134] M. B. Zugaro, A. Berthoz, and S. I. Wiener, *Background, but not foreground, spatial cues are taken as references for head direction responses by rat anterodorsal thalamus neurons.*, *The Journal of neuroscience : the official journal of the Society for Neuroscience* **21** (2001), no. 14.

[135] J. P. Bassett, M. B. Zugaro, G. M. Muir, E. J. Golob, R. U. Muller, and J. S. Taube, *Passive movements of the head do not abolish anticipatory firing properties of head direction cells*, *Journal of Neurophysiology* **93** (mar, 2005) 1304–1316.

[136] M. E. Shinder and J. S. Taube, *Active and passive movement are encoded equally by head direction cells in the anterodorsal thalamus*, *Journal of Neurophysiology* **106** (aug, 2011) 788–800.

[137] J. P. Goodridge, P. A. Dudchenko, K. A. Worboys, E. J. Golob, and J. S. Taube, *Cue control and head direction cells*, *Behavioral Neuroscience* **112** (1998), no. 4 749–761.

[138] M. B. Zugaro, A. Arleo, A. Berthoz, and S. I. Wiener, *Rapid spatial reorientation and head direction cells*, *Journal of Neuroscience* **23** (apr, 2003) 3478–3482.

[139] D. G. Wallace, D. J. Hines, S. M. Pellis, and I. Q. Whishaw, *Vestibular information is required for dead reckoning in the rat*, *Journal of Neuroscience* **22** (nov, 2002) 10009–10017.

[140] Y. Zheng, M. Goddard, C. L. Darlington, and P. F. Smith, *Long-Term deficits on a foraging task after bilateral vestibular deafferentation in rats*, *Hippocampus* **19** (may, 2009) 480–486.

[141] S. S. Kim, A. M. Hermundstad, S. Romani, L. F. Abbott, and V. Jayaraman, *Generation of stable heading representations in diverse visual scenes*, *Nature* **576** (nov, 2019) 126–131.

[142] C. S. Royden, M. S. Banks, and J. A. Crowell, *The perception of heading during eye movements*, *Nature* **360** (1992), no. 6404 583–585.

[143] V. E. Pettorossi and M. Schieppati, *Neck Proprioception Shapes Body Orientation and Perception of Motion*, *Frontiers in Human Neuroscience* **8** (nov, 2014) 895.

[144] A. Gasbarri, M. G. Packard, E. Campana, and C. Pacitti, *Anterograde and retrograde tracing of projections from the ventral tegmental area to the hippocampal formation in the rat*, *Brain Research Bulletin* **33** (1994), no. 4 445–452.

[145] K. Asumbisa, A. Peyrache, and S. Trenholm, *Flexible cue anchoring strategies enable stable head direction coding in both sighted and blind animals*, *bioRxiv* (jan, 2022) 2022.01.12.476111.

[146] S. D. Vann and J. P. Aggleton, *Selective dysgranular retrosplenial cortex lesions in rats disrupt allocentric performance of the radial-arm maze task*, *Behavioral Neuroscience* **119** (dec, 2005) 1682–1686.

[147] B. J. Clark, J. P. Bassett, S. S. Wang, and J. S. Taube, *Impaired head direction cell representation in the anterodorsal thalamus after lesions of the retrosplenial cortex*, *Journal of Neuroscience* **30** (apr, 2010) 5289–5302.

[148] T. van Groen and J. M. Wyss, *Connections of the retrosplenial granular a cortex in the rat*, *Journal of Comparative Neurology* **300** (oct, 1990) 593–606.

[149] T. van Groen and J. M. Wyss, *Connections of the retrosplenial granular b cortex in the rat*, *Journal of Comparative Neurology* **463** (aug, 2003) 249–263.

[150] T. van Groen and J. M. Wyss, *Connections of the retrosplenial dysgranular cortex in the rat*, *Journal of Comparative Neurology* **315** (1992), no. 2 200–216.

[151] H. Shibata, *Efferent projections from the anterior thalamic nuclei to the cingulate cortex in the rat*, *Journal of Comparative Neurology* **330** (1993), no. 4 533–542.

[152] L. F. Fischer, R. M. Soto-Albors, F. Buck, and M. T. Harnett, *Representation of visual landmarks in retrosplenial cortex*, *eLife* **9** (mar, 2020).

[153] A. S. Alexander and D. A. Nitz, *Retrosplenial cortex maps the conjunction of internal and external spaces*, *Nature Neuroscience* **18** (aug, 2015) 1143–1151.

[154] H. J. Page and K. J. Jeffery, *Landmark-based updating of the head direction system by retrosplenial cortex: A computational model*, *Frontiers in Cellular Neuroscience* **12** (jul, 2018) 191.

[155] P. Y. Jacob, G. Casali, L. Spieser, H. Page, D. Overington, and K. Jeffery, *An independent, landmark-dominated head-direction signal in dysgranular retrosplenial cortex*, *Nature Neuroscience* **20** (dec, 2017) 173–175.

[156] S. D. Auger, S. L. Mullally, and E. A. Maguire, *Retrosplenial cortex codes for permanent landmarks*, *PLoS ONE* **7** (aug, 2012) e43620.

[157] L. M. Franco and M. J. Goard, *A distributed circuit for associating environmental context with motor choice in retrosplenial cortex*, *Science Advances* **7** (aug, 2021).

[158] B. G. Cooper and S. J. Mizumori, *Retrosplenial cortex inactivation selectivity impairs navigation in darkness*, *NeuroReport* **10** (feb, 1999) 625–630.

[159] I. Q. Whishaw, H. Maaswinkel, C. L. Gonzalez, and B. Kolb, *Deficits in allothetic and idiothetic spatial behavior in rats with posterior cingulate cortex lesions*, *Behavioural Brain Research* **118** (jan, 2001) 67–76.

[160] S. Keshavarzi, E. F. Bracey, R. A. Faville, D. Campagner, A. L. Tyson, S. C. Lenzi, T. Branco, and T. W. Margrie, *Multisensory coding of angular head velocity in the retrosplenial cortex*, *Neuron* **110** (feb, 2022) 532–543.e9.

[161] N. Zhang, R. M. Grieves, and K. J. Jeffery, *Title: Environment symmetry drives a multidirectional code in rat retrosplenial cortex 1*, .

[162] J. Simonnet, M. Nassar, F. Stella, I. Cohen, B. Mathon, C. N. Boccara, R. Miles, and D. Fricker, *Activity dependent feedback inhibition may maintain head direction signals in mouse presubiculum*, *Nature Communications* **8** (jul, 2017) 1–14.

[163] J. Voigts and M. T. Harnett, *Somatic and Dendritic Encoding of Spatial Variables in Retrosplenial Cortex Differs during 2D Navigation*, *Neuron* **105** (jan, 2020) 237–245.e4.

[164] M. Pachitariu, C. Stringer, S. Schröder, M. Dipoppa, L. F. Rossi, M. Carandini, and K. D. Harris, *Suite2p: beyond 10,000 neurons with standard two-photon microscopy*, *bioRxiv* (2016) 061507.

[165] C. Stringer and M. Pachitariu, *Computational processing of neural recordings from calcium imaging data*, *Current Opinion in Neurobiology* **55** (apr, 2019) 22–31.

[166] J. Friedrich, P. Zhou, and L. Paninski, *Fast online deconvolution of calcium imaging data*, *PLoS Computational Biology* **13** (mar, 2017) e1005423, [arXiv:1609.0063].

[167] Z. Xu, W. Wu, S. S. Winter, M. L. Mehlman, W. N. Butler, C. M. Simmons, R. E. Harvey, L. E. Berkowitz, Y. Chen, J. S. Taube, A. A. Wilber, and B. J. Clark, *A Comparison of Neural Decoding Methods and Population Coding Across Thalamo-Cortical Head Direction Cells*, *Frontiers in Neural Circuits* **13** (dec, 2019) 75.

[168] C. D. Harvey, P. Coen, and D. W. Tank, *Choice-specific sequences in parietal cortex during a virtual-navigation decision task*, *Nature* **484** (mar, 2012) 62–68.

[169] A. B. Saleem, E. M. Diamanti, J. Fournier, K. D. Harris, and M. Carandini, *Coherent encoding of subjective spatial position in visual cortex and hippocampus*, *Nature* **562** (sep, 2018) 124–127.

[170] N. J. Sofroniew, J. D. Cohen, A. K. Lee, and K. Svoboda, *Natural whisker-guided behavior by head-fixed mice in tactile virtual reality*, *Journal of Neuroscience* **34** (2014), no. 29 9537–9550.

[171] M. Kislin, E. Mugantseva, D. Molotkov, N. Kulesskaya, S. Khirug, I. Kirilkin, E. Pryazhnikov, J. Kolikova, D. Toptunov, M. Yuryev, R. Giniatullin, V. Voikar, C. Rivera, H. Rauvala, and L. Khiroug, *Flat-floored air-lifted platform: A new method for combining behavior with microscopy or electrophysiology on awake freely moving rodents*, *Journal of Visualized Experiments* (jun, 2014) e51869.

[172] A. Powell, W. M. Connelly, A. Vasalauskaite, A. J. Nelson, S. D. Vann, J. P. Aggleton, F. Sengpiel, and A. Ranson, *Stable Encoding of Visual Cues in the Mouse Retrosplenial Cortex*, *Cerebral Cortex* **30** (jun, 2020) 4424–4437.

[173] R. M. Yoder and J. S. Taube, *The vestibular contribution to the head direction signal and navigation*, *Frontiers in Integrative Neuroscience* **8** (apr, 2014) 32.

[174] D. Yoganarasimha, X. Yu, and J. J. Knierim, *Head direction cell representations maintain internal coherence during conflicting proximal and distal cue rotations: Comparison with hippocampal place cells*, *Journal of Neuroscience* **26** (jan, 2006) 622–631.

[175] E. A. Maguire, N. Burgess, and J. O'Keefe, *Human spatial navigation: Cognitive maps, sexual dimorphism, and neural substrates*, *Current Opinion in Neurobiology* **9** (apr, 1999) 171–177.

[176] A. D. Ekstrom, M. J. Kahana, J. B. Caplan, T. A. Fields, E. A. Isham, E. L. Newman, and I. Fried, *Cellular networks underlying human spatial navigation*, *Nature* **425** (sep, 2003) 184–187.

[177] T. Wolbers and C. Büchel, *Dissociable retrosplenial and hippocampal contributions to successful formation of survey representations*, *Journal of Neuroscience* **25** (2005), no. 13 3333–3340.

[178] S. Yu, A. P. Boone, C. He, R. C. Davis, M. Hegarty, E. R. Chrastil, and E. G. Jacobs, *Age-Related Changes in Spatial Navigation Are Evident by Midlife and Differ by Sex*, *Psychological Science* **32** (may, 2021) 692–704.

[179] H. T. Blair and P. E. Sharp, *Visual and vestibular influences on head-direction cells in the anterior thalamus of the rat*, *Behavioral Neuroscience* **110** (1996), no. 4 643–660.

[180] P. A. LaChance, J. Graham, B. L. Shapiro, A. J. Morris, and J. S. Taube, *Landmark-modulated directional coding in postrhinal cortex*, *Science Advances* **8** (jan, 2022) 8404.

[181] Y. Yan, N. Burgess, and A. Bicanski, *A model of head direction and landmark coding in complex environments*, *PLoS Computational Biology* **17** (sep, 2021) e1009434.

[182] A. Bicanski and N. Burgess, *Environmental anchoring of head direction in a computational model of retrosplenial cortex*, *Journal of Neuroscience* **36** (nov, 2016) 11601–11618.

[183] Y. R. Lozano, H. Page, P.-Y. Jacob, E. Lomi, J. Street, and K. Jeffery, *Retrosplenial and postsubicular head direction cells compared during visual landmark discrimination*, *Brain and Neuroscience Advances* **1** (jan, 2017) 239821281772185.

[184] J. S. Taube, *The head direction signal: Origins and sensory-motor integration*, *Annual Review of Neuroscience* **30** (2007) 181–207.

[185] D. E. Angelaki and J. Laurens, *The head direction cell network: attractor dynamics, integration within the navigation system, and three-dimensional properties*, *Current Opinion in Neurobiology* **60** (feb, 2020) 136–144.

[186] J. P. Goodridge and J. S. Taube, *Interaction between the postsubiculum and anterior thalamus in the generation of head direction cell activity*, *Journal of Neuroscience* **17** (1997), no. 23 9315–9330.

[187] O. Kornienko, P. Latuske, M. Bassler, L. Kohler, and K. Allen, *Non-rhythmic head-direction cells in the parahippocampal region are not constrained by attractor network dynamics*, *eLife* **7** (sep, 2018).

[188] J. B. van Wijngaarden, S. S. Babl, and H. T. Ito, *Entorhinal-retrosplenial circuits for allocentric-egocentric transformation of boundary coding*, *eLife* **9** (oct, 2020) 1–25.

[189] E. J. Bubb, C. Metzler-Baddeley, and J. P. Aggleton, *The cingulum bundle: Anatomy, function, and dysfunction*, sep, 2018.

[190] D. Aronov, R. Nevers, and D. W. Tank, *Mapping of a non-spatial dimension by the hippocampal-entorhinal circuit*, *Nature* **543** (mar, 2017) 719–722.

[191] B. Shahbaba, L. Li, F. Agostinelli, M. Saraf, K. W. Cooper, D. Haghverdian, G. A. Elias, P. Baldi, and N. J. Fortin, *Hippocampal ensembles represent sequential relationships among an extended sequence of nonspatial events*, *Nature Communications* **13** (feb, 2022) 1–17.

[192] H. Eichenbaum, *Time cells in the hippocampus: A new dimension for mapping memories*, oct, 2014.

[193] N. E. Medeiros and C. A. Curcio, *Preservation of ganglion cell layer neurons in age-related macular degeneration*, *Investigative Ophthalmology and Visual Science* **42** (2001), no. 3 795–803.

[194] F. Mazzoni, E. Novelli, and E. Strettoi, *Retinal ganglion cells survive and maintain normal dendritic morphology in a mouse model of inherited photoreceptor degeneration*, *Journal of Neuroscience* **28** (dec, 2008) 14282–14292.

[195] D. García-Ayuso, J. Di Pierdomenico, M. Vidal-Sanz, and M. P. Villegas-Pérez, *Retinal ganglion cell death as a late remodeling effect of photoreceptor degeneration*, *International Journal of Molecular Sciences* **20** (sep, 2019).

[196] M. S. Humayun, J. D. Dorn, L. Da Cruz, G. Dagnelie, J. A. Sahel, P. E. Stanga, A. V. Cideciyan, J. L. Duncan, D. Eliott, E. Filley, A. C. Ho, A. Santos, A. B. Safran, A. Arditi, L. V. Del Priore, and R. J. Greenberg, *Interim results from the international trial of second sight's visual prosthesis*, *Ophthalmology* **119** (apr, 2012) 779–788.

[197] D. Palanker, Y. Le Mer, S. Mohand-Said, M. Muqit, and J. A. Sahel, *Photovoltaic Restoration of Central Vision in Atrophic Age-Related Macular Degeneration*, *Ophthalmology* **127** (aug, 2020) 1097–1104.

[198] A. Bi, J. Cui, Y. P. Ma, E. Olshevskaya, M. Pu, A. M. Dizhoor, and Z. H. Pan, *Ectopic Expression of a Microbial-Type Rhodopsin Restores Visual Responses in Mice with Photoreceptor Degeneration*, *Neuron* **50** (apr, 2006) 23–33.

[199] J. A. Sahel, E. Boulanger-Scemama, C. Pagot, A. Arleo, F. Galluppi, J. N. Martel, S. D. Esposti, A. Delaux, J. B. de Saint Aubert, C. de Montleau, E. Gutman, I. Audo, J. Duebel, S. Picaud, D. Dalkara, L. Blouin, M. Taiel, and B. Roska, *Partial recovery of visual function in a blind patient after optogenetic therapy*, *Nature Medicine* **27** (jul, 2021) 1223–1229.

[200] A. Polosukhina, J. Litt, I. Tochitsky, J. Nemargut, Y. Sychev, I. De Kouchkovsky, T. Huang, K. Borges, D. Trauner, R. N. Van Gelder, and R. H. Kramer, *Photochemical Restoration of Visual Responses in Blind Mice*, *Neuron* **75** (jul, 2012) 271–282.

[201] I. Tochitsky, Z. Helft, V. Meseguer, R. B. Fletcher, K. A. Vessey, M. Telias, B. Denlinger, J. Malis, E. L. Fletcher, and R. H. Kramer, *How Azobenzene Photoswitches Restore Visual Responses to the Blind Retina*, *Neuron* **92** (oct, 2016) 100–113.

[202] M. J. Phillips, D. C. Otteson, and D. M. Sherry, *Progression of neuronal and synaptic remodeling in the rd 10 mouse model of retinitis pigmentosa*, *Journal of Comparative Neurology* **518** (jun, 2010) 2071–2089.

[203] E. E. O'Brien, U. Greferath, and E. L. Fletcher, *The effect of photoreceptor degeneration on ganglion cell morphology*, *Journal of Comparative Neurology* **522** (apr, 2014) 1155–1170.

[204] B. W. Jones, R. L. Pfeiffer, W. D. Ferrell, C. B. Watt, M. Marmor, and R. E. Marc, *Retinal remodeling in human retinitis pigmentosa*, *Experimental Eye Research* **150** (sep, 2016) 149–165.

[205] K. M. Andersen, L. Sauer, R. H. Gensure, M. Hammer, and P. S. Bernstein, *Characterization of retinitis pigmentosa using fluorescence lifetime imaging ophthalmoscopy (FLIO)*, *Translational Vision Science and Technology* **7** (may, 2018).

[206] C. Sekirnjak, L. H. Jepson, P. Hottowy, A. Sher, W. Dabrowski, A. M. Litke, and E. J. Chichilnisky, *Changes in physiological properties of rat ganglion cells during retinal degeneration*, *Journal of Neurophysiology* **105** (may, 2011) 2560–2571.

[207] M. Telias, B. Denlinger, Z. Helft, C. Thornton, B. Beckwith-Cohen, and R. H. Kramer, *Retinoic Acid Induces Hyperactivity, and Blocking Its Receptor Unmasks Light Responses and Augments Vision in Retinal Degeneration*, *Neuron* **102** (may, 2019) 574–586.e5.

[208] D. J. Margolis, G. Newkirk, T. Euler, and P. B. Detwiler, *Functional stability of retinal ganglion cells after degeneration-induced changes in synaptic input*, *Journal of Neuroscience* **28** (jun, 2008) 6526–6536.

[209] H. Choi, L. Zhang, M. S. Cembrowski, C. F. Sabottke, A. L. Markowitz, D. A. Butts, W. L. Kath, J. H. Singer, and H. Riecke, *Intrinsic bursting of AII amacrine cells underlies oscillations in the rd1 mouse retina*, *Journal of Neurophysiology* **112** (sep, 2014) 1491–1504.

[210] I. Tochitsky, A. Polosukhina, V. E. Degtyar, N. Gallerani, C. M. Smith, A. Friedman, R. N. Van Gelder, D. Trauner, D. Kaufer, and R. H. Kramer, *Restoring visual function to blind mice with a photoswitch that exploits electrophysiological remodeling of retinal ganglion cells*, *Neuron* **81** (feb, 2014) 800–813.

[211] Y. Lin, B. W. Jones, A. Liu, J. F. Tucker, K. Rapp, L. Luo, W. Baehr, P. S. Bernstein, C. B. Watt, J. Yang, M. V. Shaw, and R. E. Marc, *Retinoid receptors trigger neuritogenesis in retinal degenerations*, *The FASEB Journal* **26** (jan, 2012) 81–92.

[212] M. Telias, S. Nawy, and R. H. Kramer, *Degeneration-Dependent Retinal Remodeling: Looking for the Molecular Trigger*, *Frontiers in Neuroscience* **14** (dec, 2020).

[213] B. Denlinger, Z. Helft, M. Telias, H. Lorach, D. Palanker, and R. H. Kramer, *Local photoreceptor degeneration causes local pathophysiological remodeling of retinal neurons*, *JCI Insight* **5** (jan, 2020).

[214] S. F. Stasheff, *Clinical impact of spontaneous hyperactivity in degenerating retinas: Significance for diagnosis, symptoms, and treatment*, *Frontiers in Cellular Neuroscience* **12** (sep, 2018).

[215] J. R. Heckenlively, S. L. Yoser, L. H. Friedman, and J. J. Oversier, *Clinical findings and common symptoms in retinitis pigmentosa*, *American Journal of Ophthalmology* **105** (may, 1988) 504–511.

[216] A. K. Bittner, M. Diener-West, and G. Dagnelie, *A survey of photopsias in self-reported retinitis pigmentosa: Location of photopsias is related to disease severity*, *Retina* **29** (nov, 2009) 1513–1521.

[217] J. Delbeke, D. Pins, G. Michaux, M. C. Wanet-Defalque, S. Parrini, and C. Veraart, *Electrical stimulation of anterior visual pathways in retinitis pigmentosa*, *Investigative Ophthalmology and Visual Science* **42** (2001), no. 1 291–297.

[218] L. M. Hoffman, K. Garcha, K. Karamboulas, M. F. Cowan, L. M. Drysdale, W. A. Horton, and T. M. Underhill, *BMP action in skeletogenesis involves attenuation of retinoid signaling*, *Journal of Cell Biology* **174** (jul, 2006) 101–113.

[219] F. Naarendorp, T. M. Esdaille, S. M. Banden, J. Andrews-Labenski, O. P. Gross, and E. N. Pugh, *Dark light, rod saturation, and the absolute and incremental sensitivity of mouse cone vision*, *Journal of Neuroscience* **30** (sep, 2010) 12495–12507.

[220] F. Haeseleer, G. F. Jang, Y. Imanishi, C. A. Driessen, M. Matsumura, P. S. Nelson, and K. Palczewski, *Dual-substrate specificity short chain retinol dehydrogenases from the vertebrate retina*, *Journal of Biological Chemistry* **277** (nov, 2002) 45537–45546.

[221] B. X. Wu, G. Moiseyev, Y. Chen, B. Rohrer, R. K. Crouch, and J. X. Ma, *Identification of RDH10, an all-trans retinol dehydrogenase, in retinal Müller cells*, *Investigative Ophthalmology and Visual Science* **45** (nov, 2004) 3857–3862.

[222] A. Morshedian, J. J. Kaylor, S. Y. Ng, A. Tsan, R. Frederiksen, T. Xu, L. Yuan, A. P. Sampath, R. A. Radu, G. L. Fain, and G. H. Travis, *Light-Driven Regeneration of Cone Visual Pigments through a Mechanism Involving RGR Opsin in Müller Glial Cells*, *Neuron* **102** (jun, 2019) 1172–1183.e5.

[223] A. J. Fischer, J. Wallman, J. R. Mertz, and W. K. Stell, *Localization of retinoid binding proteins, retinoid receptors, and retinaldehyde dehydrogenase in the chick eye*, *Journal of Neurocytology* **28** (1999), no. 7 597–609.

[224] A. R. Harper, A. T. Le, T. Mather, A. Burgett, W. Berry, and J. A. Summers, *Design, synthesis, and ex vivo evaluation of a selective inhibitor for retinaldehyde dehydrogenase enzymes*, *Bioorganic and Medicinal Chemistry* **26** (dec, 2018) 5766–5779.

[225] P. Germain, P. Chambon, G. Eichele, R. M. Evans, M. A. Lazar, M. Leid, A. R. De Lera, R. Lotan, D. J. Mangelsdorf, and H. Gronemeyer, *International union of pharmacology. LX. Retinoic acid receptors*, *Pharmacological Reviews* **58** (dec, 2006) 712–725.

[226] R. Blomhoff and H. K. Blomhoff, *Overview of retinoid metabolism and function*, *Journal of Neurobiology* **66** (jun, 2006) 606–630.

[227] M. Rhinn and P. Dollé, *Retinoic acid signalling during development*, *Development* **139** (mar, 2012) 843–858.

[228] S. S. Robinson, *The Role of Disulfiram in Alcohol Metabolism and the Treatment of Alcoholism*, *ACS Symposium Series* **1189** (2015) 191–206.

[229] J. A. Summers Rada, L. R. Hollaway, W. Lam, N. Li, and J. L. Napoli, *Identification of RALDH2 as a visually regulated retinoic acid synthesizing enzyme in the chick choroid*, *Investigative Ophthalmology and Visual Science* **53** (mar, 2012) 1649–1662.

[230] H. R. Kranzler and M. Soyka, *Diagnosis and pharmacotherapy of alcohol use disorder a review*, *JAMA - Journal of the American Medical Association* **320** (aug, 2018) 815–824.

[231] P. Germain, C. Gaudon, V. Pogenberg, S. Sanglier, A. Van Dorsselaer, C. A. Royer, M. A. Lazar, W. Bourguet, and H. Gronemeyer, *Differential Action on Coregulator Interaction Defines Inverse Retinoid Agonists and Neutral Antagonists*, *Chemistry and Biology* **16** (may, 2009) 479–489.

[232] S. F. Stasheff, M. Shankar, and M. P. Andrews, *Developmental time course distinguishes changes in spontaneous and light-evoked retinal ganglion cell activity in rd1 and rd10 mice*, *Journal of Neurophysiology* **105** (jun, 2011) 3002–3009.

[233] J. J. Janssen, E. D. Kuhlmann, A. H. Van Vugt, H. J. Winkens, B. P. Janssen, A. F. Deutman, and C. A. Driessen, *Retinoic acid receptors and retinoid X receptors in the mature retina: Subtype determination and cellular distribution*, *Current Eye Research* **19** (1999), no. 4 338–347.

[234] J. Wang, H. Xiao, S. Barwick, Y. Liu, and S. B. Smith, *Optimal timing for activation of sigma 1 receptor in the Pde6brd10/J (rd10) mouse model of retinitis pigmentosa*, *Experimental Eye Research* **202** (jan, 2021).

[235] T. D. Marks and M. J. Goard, *Stimulus-dependent representational drift in primary visual cortex*, *Nature Communications* **12** (dec, 2021).

[236] S. E. de Vries, J. A. Lecoq, M. A. Buice, P. A. Groblewski, G. K. Ocker, M. Oliver, D. Feng, N. Cain, P. Ledochowitsch, D. Millman, K. Roll, M. Garrett, T. Keenan, L. Kuan, S. Mihalas, S. Olsen, C. Thompson, W. Wakeman, J. Waters, D. Williams, C. Barber, N. Berbesque, B. Blanchard, N. Bowles, S. D. Caldejon, L. Casal, A. Cho, S. Cross, C. Dang, T. Dolbeare, M. Edwards, J. Galbraith, N. Gaudreault, T. L. Gilbert, F. Griffin, P. Hargrave, R. Howard, L. Huang, S. Jewell, N. Keller, U. Knoblich, J. D. Larkin, R. Larsen, C. Lau, E. Lee, F. Lee, A. Leon, L. Li, F. Long, J. Luviano, K. Mace, T. Nguyen, J. Perkins, M. Robertson, S. Seid, E. Shea-Brown, J. Shi, N. Sjoquist, C. Slaughterbeck, D. Sullivan, R. Valenza, C. White, A. Williford, D. M. Witten, J. Zhuang, H. Zeng, C. Farrell, L. Ng, A. Bernard, J. W. Phillips, R. C. Reid, and C. Koch, *A large-scale standardized physiological survey reveals functional organization of the mouse visual cortex*, *Nature Neuroscience* **23** (jan, 2020) 138–151.

[237] R. A. Care, I. A. Anastassov, D. B. Kastner, Y. M. Kuo, L. Della Santina, and F. A. Dunn, *Mature Retina Compensates Functionally for Partial Loss of Rod Photoreceptors*, *Cell Reports* **31** (jun, 2020).

[238] H. Leinonen, N. C. Pham, T. Boyd, J. Santoso, K. Palczewski, and F. Vinberg, *Homeostatic plasticity in the retina is associated with maintenance of night vision during retinal degenerative disease*, *eLife* **9** (sep, 2020) 1–27.

[239] R. A. Care, D. B. Kastner, I. De la Huerta, S. Pan, A. Khoche, L. Della Santina, C. Gamlin, C. Santo Tomas, J. Ngo, A. Chen, Y. M. Kuo, Y. Ou, and F. A. Dunn, *Partial Cone Loss Triggers Synapse-Specific Remodeling and Spatial Receptive Field Rearrangements in a Mature Retinal Circuit*, *Cell Reports* **27** (may, 2019) 2171–2183.e5.

[240] S. Nirenberg and C. Pandarinath, *Retinal prosthetic strategy with the capacity to restore normal vision*, *Proceedings of the National Academy of Sciences of the United States of America* **109** (sep, 2012) 15012–15017.

[241] N. Isoherranen and G. Zhong, *Biochemical and physiological importance of the CYP26 retinoic acid hydroxylases*, *Pharmacology and Therapeutics* **204** (dec, 2019).

[242] Y. Ikeda, K. M. Nishiguchi, F. Miya, N. Shimozawa, J. Funatsu, S. Nakatake, K. Fujiwara, T. Tachibana, Y. Murakami, T. Hisatomi, S. Yoshida, Y. Yasutomi, T. Tsunoda, T. Nakazawa, T. Ishibashi, and K. H. Sonoda, *Discovery of a cynomolgus monkey family with retinitis pigmentosa*, *Investigative Ophthalmology and Visual Science* **59** (feb, 2018) 826–830.

[243] S. Schierle and D. Merk, *Therapeutic modulation of retinoid X receptors–SAR and therapeutic potential of RXR ligands and recent patents*, *Expert Opinion on Therapeutic Patents* **29** (aug, 2019) 605–621.

[244] L. Yin, K. Greenberg, J. J. Hunter, D. Dalkara, K. D. Kolstad, B. D. Masella, R. Wolfe, M. Visel, D. Stone, R. T. Libby, D. DiLoreto, D. Schaffer, J. Flannery, D. R. Williams, and W. H. Merigan, *Intravitreal injection of AAV2 transduces macaque inner retina*, *Investigative Ophthalmology and Visual Science* **52** (apr, 2011) 2775–2783.

[245] K. Xue and R. E. MacLaren, *Antisense oligonucleotide therapeutics in clinical trials for the treatment of inherited retinal diseases*, *Expert Opinion on Investigational Drugs* **29** (oct, 2020) 1163–1170.

[246] T. Taniguchi, K. ichi Endo, H. Tanioka, M. Sasaoka, K. Tashiro, S. Kinoshita, and M. Kageyama, *Novel use of a chemically modified siRNA for robust and sustainable in vivo gene silencing in the retina*, *Scientific Reports* **10** (dec, 2020).

[247] H. Y. Tu, Y. J. Chen, A. R. McQuiston, C. C. Chiao, and C. K. Chen, *A novel retinal oscillation mechanism in an autosomal dominant photoreceptor degeneration mouse model*, *Frontiers in Cellular Neuroscience* **9** (jan, 2016).

[248] V. Busskamp, J. Duebel, D. Balya, M. Fradot, T. J. Viney, S. Siegert, A. C. Groner, E. Cabuy, V. Forster, M. Seeliger, M. Biel, P. Humphries, M. Paques, S. Mohand-Said, D. Trono, K. Deisseroth, J. A. Sahel, S. Picaud, and B. Roska, *Genetic reactivation of cone photoreceptors restores visual responses in retinitis pigmentosa*, *Science* **329** (jul, 2010) 413–417.

[249] H. C. Stronks and G. Dagnelie, *The functional performance of the Argus II retinal prosthesis*, *Expert Review of Medical Devices* **11** (jan, 2014) 23–30.

[250] G. Dagnelie, P. Christopher, A. Arditi, L. da Cruz, J. L. Duncan, A. C. Ho, L. C. Olmos de Koo, J. A. Sahel, P. E. Stanga, G. Thumann, Y. Wang, M. Arsiero, J. D. Dorn, and R. J. Greenberg, *Performance of real-world functional vision tasks by blind subjects improves after implantation with the Argus® II retinal prosthesis system*, *Clinical and Experimental Ophthalmology* **45** (mar, 2017) 152–159.

[251] J. M. Barrett, P. Degenaar, and E. Sernagor, *Blockade of pathological retinal ganglion cell hyperactivity improves optogenetically evoked light responses in rd1 mice*, *Frontiers in Cellular Neuroscience* **9** (aug, 2015).

[252] I. Tochitsky, M. A. Kienzler, E. Isacoff, and R. H. Kramer, *Restoring Vision to the Blind with Chemical Photoswitches*, *Chemical Reviews* **118** (nov, 2018) 10748–10773.

[253] K. Hüll, T. Benster, M. B. Manookin, D. Trauner, R. N. Van Gelder, and L. Laprell, *Photopharmacologic Vision Restoration Reduces Pathological Rhythmic Field Potentials in Blind Mouse Retina*, *Scientific Reports* **9** (dec, 2019).

[254] I. Nauhaus, K. J. Nielsen, and E. M. Callaway, *Nonlinearity of two-photon ca 2+ imaging yields distorted measurements of tuning for V1 neuronal populations*, *Journal of Neurophysiology* **107** (feb, 2012) 923–936.

[255] Y. Adam, J. J. Kim, S. Lou, Y. Zhao, M. E. Xie, D. Brinks, H. Wu, M. A. Mostajo-Radji, S. Kheifets, V. Parot, S. Chettih, K. J. Williams, B. Gmeiner, S. L. Farhi, L. Madisen, E. K. Buchanan, I. Kinsella, D. Zhou, L. Paninski, C. D. Harvey, H. Zeng, P. Arlotta, R. E. Campbell, and A. E. Cohen, *Voltage imaging and optogenetics reveal behaviour-dependent changes in hippocampal dynamics*, *Nature 2019 569:7756* **569** (may, 2019) 413–417.

[256] A. S. Abdelfattah, T. Kawashima, A. Singh, O. Novak, H. Liu, Y. Shuai, Y. C. Huang, L. Campagnola, S. C. Seeman, J. Yu, J. Zheng, J. B. Grimm, R. Patel, J. Friedrich, B. D. Mensh, L. Paninski, J. J. Macklin, G. J. Murphy, K. Podgorski, B. J. Lin, T. W. Chen, G. C. Turner, Z. Liu, M. Koyama, K. Svoboda, M. B. Ahrens, L. D. Lavis, and E. R. Schreiter, *Bright and photostable chemigenetic indicators for extended in vivo voltage imaging*, *Science* **365** (aug, 2019) 699–704.

[257] T. Knöpfel and C. Song, *Optical voltage imaging in neurons: moving from technology development to practical tool*, *Nature Reviews Neuroscience 2019 20:12* **20** (nov, 2019) 719–727.

[258] "Grafman: Handbook of Neuropsychology: Section 14:... - Google Scholar."

[259] M. M. Merzenich and J. F. Brugge, *Representation of the cochlear partition on the superior temporal plane of the macaque monkey*, *Brain Research* **50** (feb, 1973) 275–296.

[260] A. Morel and J. H. Kaas, *Subdivisions and connections of auditory cortex in owl monkeys*, *Journal of Comparative Neurology* **318** (1992), no. 1 27–63.

[261] H. Ko, S. B. Hofer, B. Pichler, K. A. Buchanan, P. J. Sjöström, and T. D. Mrsic-Flogel, *Functional specificity of local synaptic connections in neocortical networks*, *Nature* **473** (may, 2011) 87–91.

[262] M. Beyeler, A. Rokem, G. M. Boynton, and I. Fine, *Learning to see again: Biological constraints on cortical plasticity and the implications for sight restoration technologies*, *Journal of Neural Engineering* **14** (aug, 2017) 051003.